



COMPUTER-ASSISTED IMAGE REGISTRATION FOR HDR  
BRACHYTHERAPY OF THE LIVER IN MRI

**DISSERTATION**

zur Erlangung des akademischen Grades

**Doktoringenieur (Dr.-Ing.)**

angenommen durch die Fakultät für Informatik  
der Otto-von-Guericke-Universität Magdeburg

von M.Sc. Tim König

geboren am 02. März 1989 in Magdeburg

Gutachter

Prof. Dr.-Ing. Klaus-Dietz Tönnies

Prof. Dr. rer. nat. Jan Modersitzki

Prof. Dr.-Ing. Joachim Denzler

*Magdeburg, den 29.05.2019*



## ABSTRACT

---

The liver is often the primary target of metastatic colorectal cancer because of its filter function from the intestinal blood. The interstitial high-dose rate brachytherapy is a minimally invasive therapy where the tumors can be treated by internal radiation. This requires a percutaneous placement of one or more flexible plastic catheters, called applicators, within the tumors. To maximize the treatment outcome, the optimal applicator configuration is pre-planned on magnetic resonance images and then implemented via a magnetic resonance-guided intervention. A computer-assisted transfer of the pre-planning information onto the interventional images would support the radiologist during the tumor puncture. However, such a transfer is challenging because of the short calculation times and high accuracies which are required for a clinical application.

In this thesis, existing state-of-the-art methods are investigated and novel strategies developed to provide a solution which is suitable for the interventions. A two-step approach is presented which comprises a volume-to-volume as well as volume-to-slice registration of the interventional images. Considering the volume-to-volume registration, a novel joint deformable liver registration and bias field correction approach is presented which is, to the best of my knowledge, the first working solution for a magnetic resonance-guided, interventional setting, where patient re-positioning, bias field artifacts, and extensive noise levels are considered. It is demonstrated on a wide range of real patient data sets that the proposed approach is robust, accurate, and fast. With regard to the volume-to-slice registration, an appropriate strategy is presented that is able to cope with the different breathing states during the intervention. In this context, a visual feedback system is proposed, which allows the radiologist to assess the quality of the transformed pre-planning information during the tumor puncture in real-time.



## ABSTRACT

---

Die Leber ist aufgrund ihrer Filterfunktion oft das primäre Ziel von metastasierendem Darmkrebs. Die interstitielle Brachytherapie ist eine minimalinvasive Therapie, bei der die Lebertumore durch Bestrahlung von innen behandelt werden können. Dies erfordert eine perkutane Platzierung eines oder mehrerer flexibler Kunststoffkatheter, genannt Applikatoren, innerhalb des Tumorzentrums. Um das Behandlungsergebnis zu maximieren, wird die optimale Applikatorkonfiguration auf Magnetresonanzbildern vorab geplant und durch eine magnetresonanzzgeführte Intervention umgesetzt. Eine computergestützte Übertragung der Vorplanungsinformationen auf die interventionellen Bilder würde den Radiologen bei der Tumorpunktion wesentlich unterstützen. Für die Übertragung der Informationen aus den Vorplanungsdaten in die Intervention sind schnelle und präzise 3D-3D sowie 3D-2D Registrierungsalgorithmen erforderlich.

Um diese Herausforderungen bewältigen zu können, werden in dieser Dissertation Methoden aus dem aktuellen Stand der Forschung untersucht und mit neu entwickelten Strategien kombiniert. Bezüglich der 3D-3D Registrierung wird eine Lösungsstrategie vorgestellt, die eine elastische Leberregistrierung umfasst, bei der eine Umlagerung des Patienten vor der Intervention, Bias-Feld-Artefakte und die niedrige Bildqualität der interventionellen Bilder berücksichtigt werden. Anhand einer Vielzahl von realen Patientendatensätzen wird demonstriert, dass der vorgeschlagene Ansatz ausreichend präzise und schnell für eine klinische Anwendbarkeit ist. Im Hinblick auf die 3D-2D Registrierung wird in dieser Dissertation eine geeignete Strategie präsentiert, die in der Lage ist, die verschiedenen Atemzustände während des Eingriffs zu berücksichtigen. In diesem Zusammenhang wurde ein prototypisches System entwickelt, welches es dem Radiologen während der Tumorpunktion ermöglicht, die transformierten Vorplanungsinformationen in Echtzeit anzeigen zu lassen. Dabei wird dem Radiologen bei jedem interventionellen Bild die Genauigkeit der Registrierung als farbkodiertes Feedback visualisiert.



## CONTENTS

---

1	INTRODUCTION	1
1.1	Motivation . . . . .	1
1.2	Clinical Workflow Analysis . . . . .	6
1.2.1	Limitations: Liver Intervention . . . . .	8
1.2.2	Limitations: Radiation Treatment Planning . . . . .	13
2	STATE-OF-THE-ART	15
2.1	Related Work: Liver Registration of Pre-Planning Data	17
2.2	Related Work: Liver Registration of Interventional Data	20
2.3	Selected Registration Methods . . . . .	24
2.4	Validation . . . . .	27
2.5	Remaining Issues in Liver Registration of MRI Data . . . . .	28
3	THESIS OBJECTIVES	31
4	MATERIAL	35
4.1	Volume-to-Volume Registration . . . . .	35
4.2	Volume-to-Slice Registration . . . . .	37
4.3	Evaluation Measures . . . . .	39
5	VOLUME-TO-VOLUME REGISTRATION	41
5.1	Preliminary Study A . . . . .	41
5.1.1	Material and Methods . . . . .	41
5.1.2	Results and Discussion . . . . .	44
5.2	Preliminary Study B . . . . .	46
5.2.1	Material and Methods . . . . .	47
5.2.2	Results and Discussion . . . . .	54
5.3	Complete Study: MRF-BC . . . . .	61
5.3.1	Preprocessing . . . . .	61
5.3.2	Material and Methods . . . . .	61
5.3.3	Rigid and Affine Registration . . . . .	62
5.3.4	Deformable Registration . . . . .	65
6	VOLUME-TO-SLICE REGISTRATION	73
6.1	Preliminary Study . . . . .	73
6.1.1	Rigid Registration . . . . .	73
6.1.2	Deformable Registration . . . . .	73
6.1.3	Discussion . . . . .	74
6.2	Complete Study . . . . .	75
6.2.1	Material and Methods . . . . .	76
6.2.2	Results and Discussion . . . . .	80
7	CONCLUSION	85
A	APPENDIX	87

## LIST OF FIGURES

---

Figure 1.1	CRC liver metastasis . . . . .	3
Figure 1.2	MRI-based treatment . . . . .	5
Figure 1.3	MRI data used for HDR brachytherapy of the liver . . . . .	6
Figure 1.4	Interventional software used to assist the tumor puncture . . . . .	7
Figure 1.5	Steps of HDR brachytherapy post-planning . .	8
Figure 1.6	Illustration of a typical V2V registration task .	10
Figure 1.7	Challenging examples of 3D interventional images . . . . .	11
Figure 1.8	Illustration of 2D interventional images . . . .	12
Figure 1.9	Applicator placement and radiation planning .	13
Figure 1.10	Exemplary axial slices of the 3D post-planning images including applicators . . . . .	14
Figure 3.1	Illustration of the proposed liver registration framework . . . . .	33
Figure 4.1	Illustration of the images and gold standard segmentation masks of the preliminary data .	36
Figure 4.2	Comparison of T1-TFE and THRIVE interventional planning images . . . . .	38
Figure 5.1	Multi-resolution image pyramid from coarse to fine for a pre-planning eTHRIVE and interventional THRIVE planning image . . . . .	44
Figure 5.2	Challenging data set including strong bias field and noise . . . . .	46
Figure 5.3	Challenging case with extensive, spatially varying noise and strong tissue inhomogeneities in the interventional image. . . . .	48
Figure 5.4	Illustration of the pyramidal multi-resolution scheme used within the proposed MRF-BC deformable registration . . . . .	50
Figure 5.5	Registration results where the bias field was considered and not considered during deformable image registration . . . . .	51
Figure 5.6	Example for a working bias field correction . .	52
Figure 5.7	Exemplary liver registration results of rigid, B-spline, SyN, and the proposed MRF-BC registration . . . . .	58
Figure 5.8	Exemplary tumor registration results of rigid, B-spline, SyN, and the proposed MRF-BC registration . . . . .	58



Figure 5.9	Exemplary liver registration results of rigid, B-spline, SyN, and the proposed MRF-BC registration as surface renderings . . . . .	59
Figure 5.10	Imperfect registration result of the pre-planning image . . . . .	59
Figure 5.11	Comparison of rigid and affine liver DSC values for different similarity measures . . . . .	63
Figure 5.12	Comparison of rigid and affine TRE between tumor centroids for different similarity measures . . . . .	63
Figure 5.13	Comparison of the runtimes of rigid and affine registrations for different similarity measures . . . . .	64
Figure 5.14	Exemplary case where the affine registration failed . . . . .	64
Figure 5.15	Exemplary case where the rigid registration failed. . . . .	66
Figure 5.16	Comparison of liver DSC values of the proposed MRF-BC registration for combinations of $\lambda$ and $\Delta_s^{\max}$ . . . . .	67
Figure 5.17	Comparison of tumor centroid distances of the proposed MRF-BC registration for combinations of $\lambda$ and $\Delta_s^{\max}$ . . . . .	67
Figure 5.18	Comparison of the runtimes of the proposed MRF-BC registration for different values of $\Delta_s^{\max}$ . . . . .	68
Figure 5.19	Comparison of TREs of the proposed MRF-BC registration between both registration tasks . . . . .	68
Figure 5.20	Illustration of an example where the tumor alignment after rigid registration could be considerably improved by a MRF-BC deformable registration . . . . .	70
Figure 5.21	Illustration of an exemplary good result of the presented deformable MRF-BC registration approach . . . . .	71
Figure 5.22	Illustration of an exemplary bad result of the presented deformable MRF-BC registration approach . . . . .	72
Figure 6.1	Exemplary V2S registration results between the preprocessed 2D interventional and the 3D interventional image. . . . .	75
Figure 6.2	Illustration of the bias field correction that was applied to the 2D interventional images. . . . .	77
Figure 6.3	Illustration of the essential steps of the proposed V2S registration approach . . . . .	78
Figure 6.5	Comparison of liver and tumor DSC and ED values of the proposed V2S registration. . . . .	81

Figure 6.6	Comparison of TREs between landmarks and tumor centroids and liver and of liver and tumor HDs of the proposed V2S registration . . .	81
Figure 6.7	Illustration of an exemplary good result of the proposed V2S registration approach . . . . .	82
Figure 6.8	Illustration of an exemplary bad result of the proposed V2S registration approach . . . . .	82
Figure 6.9	Illustration of the limitations of the V2S registration approach . . . . .	83

## LIST OF TABLES

---

Table 2.1	Overview of related works in the domain of pre-planning MRI liver registration . . . . .	18
Table 2.2	Overview of related works in the domain of interventional MRI liver registration . . . . .	21
Table 5.1	Results of V2V registration on a single resolution level with standard methods from ITK for the preliminary data . . . . .	45
Table 5.2	Quality comparison of the proposed MRF-BC deformable registration method to the reference methods B-spline and SyN for the preliminary data . . . . .	55
Table 5.3	Quality comparison of the proposed MRF-BC deformable registration method for the preliminary data between both registration tasks: no/all applicator present . . . . .	56
Table 5.4	Comparison of the runtime of the proposed MRF-BC deformable registration method to the reference methods B-spline and SyN as well as to rigid registration for the preliminary data . . . . .	60
Table 5.5	TRE between anatomical landmarks for the best rigid registration using NGF . . . . .	65
Table 5.6	Quality specification of the proposed MRF-BC deformable registration as well as the best rigid registration method with the best parametrization for the complete data set between both registration tasks: no/all applicator present . . . . .	69
Table 5.7	TRE between anatomical landmarks for the best parametrization of the MRF-BC deformable registration . . . . .	71
Table 6.1	Quality and runtime comparison of V2S registration methods that are available in ITK for the preliminary data . . . . .	74
Table 6.2	Quality specifications of the proposed V2S approach . . . . .	80
Table A.1	Complete quality specifications of the proposed MRF-BC deformable registration per patient . . . . .	88
Table A.2	Complete quality specifications of the proposed MRF-BC deformable registration per patient . . . . .	89

## ACRONYMS

---

CRC	colorectal cancer
HDR BT	high-dose rate brachytherapy
RFA	radiofrequency ablation
SIRT	selective internal radiotherapy
MRI	magnetic resonance imaging
CT	computed tomography
US	ultrasound
Gd-EOB-DTPA	gadolinium ethoxybenzyl diethylenetriamine pentaacetic acid
eTHRIVE	enhanced T1-weighted high resolution isotropic volume excitation
THRIVE	T1-weighted high resolution isotropic volume excitation
T1-TFE	T1-weighted turbo field echo
T1-FFE	T1-weighted fast field echo
TR	repetition time
TE	echo time
V2V	volume-to-volume
V2S	volume-to-slice
FOV	field of view
ROI	region of interest
MAD	mean absolute difference
SSD	sum of squared differences
NCC	normalized cross-correlation
MI	mutual information
NMI	normalized mutual information
MMI	Mattes mutual information

NGF	normalized gradient field
PD	point distance
ITK	Insight Segmentation and Registration Toolkit
FAIR	Flexible Algorithms for Image Registration
ANTs	Advanced Normalization Tools
TRE	target registration error
DSC	Dice similarity coefficient
HD	Hausdorff distance
ED	Euclidean distance
FFD	free-form deformation
FFSD	free-form surface deformation
FFGD	free-form grid deformation
LDDMM	large deformation diffeomorphic metric mapping
RBF	radial basis function
SDM	statistical deformation model
ICP	iterative closed point
TPS	thin plate spline
FEM	finite element method
MRF	Markov random field
MRF-BC	joint deformable liver registration and bias field correction
CNN	convolutional neural network
GPU	graphics processing unit
LBFGS	limited-memory Broyden–Fletcher–Goldfarb–Shanno
MIP	maximum intensity projection
PCA	principal components analysis
MPR	multiplanar reconstruction
ICP	iterative closest point
Data-V2V <sub>0</sub>	preliminary subset of data for volume-to-volume registration

Data-V2V <sub>1</sub>	complete data for volume-to-volume registration
Data-V2S <sub>0</sub>	preliminary subset of data for volume-to-slice registration
Data-V2S <sub>1</sub>	complete data for volume-to-slice registration
SNR	signal-to-noise ratio

## INTRODUCTION

---

### 1.1 MOTIVATION

The liver is the largest abdominal organ in the human body. It has four lobes and fills the upper right quadrant of the abdomen. The function of the liver is, among other things, to filter harmful substances from the blood so they can be released by the body, to produce bile in order to better digest fat, and to store glycogen used by the human body to produce energy. However, the liver can be affected by primary liver cancer, which arises in the liver, or by liver metastases.

Recently, Ferlay et al. (2018) presented estimated numbers of new cancer cases and deaths in Europe based on national incidence and mortality rates. Their estimates showed 82.500 new cases and 77.400 deaths caused by primary liver cancer in 2018. The vast majority (75 – 90 %) of primary liver cancers are hepatocellular carcinomas (HCCs), accounting for most of the other cancer subtypes (Center and Jemal, 2011).

Colorectal cancer (CRC) is the second most common tumor disease in Europe with 500.000 new cases and 243.000 deaths in 2018 (Ferlay et al., 2018) and about 15 - 25 % of the patients suffering from CRC already have liver metastases at the time of diagnosis and about 20 - 40 % of the patients develop these throughout the course of the disease (Garden et al., 2006; Manfredi et al., 2006). Because of its filter function from the intestinal blood, the liver is often the primary site of metastatic CRC spreading. Such liver metastases are much more common than primary liver cancer and occur when cancer cells spread from either the rectum or colon. Compared to 2012, the incidence of CRC has already increased by about 12 % and the death rate by about 13 % and there is a clear trend towards an increased CRC incidence for the coming years (Ferlay et al., 2013).

Complete surgical (R0) resection remains the accepted gold standard in the treatment of liver metastases of the CRC (Adams et al., 2013; Van Cutsem et al., 2016). It yields a survival of more than five years for over 50 % of the patients treated (de Jong et al., 2009; Hallet et al., 2016). Primary resection with curative intention depends on surgical-technical and prognostic-oncological factors and is possible in only about 20 % of affected patients (Adam et al., 2004). Volume reduction of liver metastases by neoadjuvant chemotherapy may allow secondary resection with curative intent and significantly prolongs overall survival (Adam et al., 2004). The challenge to achieve adequate volume reduction is based on the genetic and biomolecular hetero-

geneity of the CRC. The risk of incomplete resection (R1 situation) varies considerably depending on the number and size of metastases, uni- or bilobar spread, primary or secondary resection, as well as on the surgical approach. The survival time is significantly reduced in an R1 situation.

Multimodal therapy concepts in an interdisciplinary setting have meanwhile become a standard for hepatic metastatic CRC (Van Cutsem et al., 2016). Minimally invasive radiological procedures complement surgical or systemic procedures or, in the case of selected patients with a low tumor burden, also extend the therapeutic spectrum of non-R0 resectable liver metastases as stand-alone therapy. Interventional radiological procedures are appealing because of their potential for precise tumor cell destruction with the greatest possible protection of the functional liver tissue. The low invasive character and the avoidance of systemic side effects increase patient tolerance and the safety profile. Local anesthesia or analgosedation are usually sufficient to perform an intervention, so patients whose comorbidities would prevent general anesthesia can also be treated.

Common minimally invasive therapies are radiofrequency ablation (RFA), high-dose rate brachytherapy (HDR BT), microwave ablation, chemoembolization, high-intensity focused ultrasound, and angiography based procedures, such as selective internal radiotherapy (SIRT), or external beam radiation therapy. However, the most widespread procedures are SIRT, RFA, and HDR BT.

Endovascular therapy concepts, such as SIRT, are based on the fact that normal liver tissue is predominantly supplied via branches of the portal vein, while liver metastases of the CRC are mainly supplied by the arteries (Van den Eynden et al., 2013). This differential blood supply offers the possibility of treating liver metastases selectively via arterial vascular access and of largely omitting healthy liver tissue. Conceptually, SIRT with Yttrium-90 microspheres is a hybrid procedure of particle embolization and high-dose local radiotherapy in which an activity of 1 – 3 gigabecquerel (GBq) is applied depending on the tumor load, the calculated liver volume, and the body surface (Salem and Thurston, 2006).

Currently, RFA is still the most common interstitial thermal ablation method. The functionality of RFA is based on inducted ion movements within tumor tissue by the application of a high-frequency alternating current of usually 375 - 480 kHz. Heating of the target tissue to cytotoxic temperatures of 60°- 100° C is followed by protein denaturation with consecutive coagulative necrosis. The extent of tissue heating and heat propagation depends on the specific tissue resistance, current density and exposure time. Furthermore, the blood flow is decisive for the heat convection. For complete (R0-) ablation, sufficient and uniform heating of the target lesion must be ensured. Despite the possibility of achieving larger ablation zones through the use of cluster



probes, a size limitation of the R0 ablatable metastases of less than 3 cm diameter is therefore generally accepted (Ayav et al., 2010). However, for colorectal liver metastases with a diameter smaller than 3 cm, RFA can in principle achieve a comparable local control as surgical resection (Lee et al., 2016).

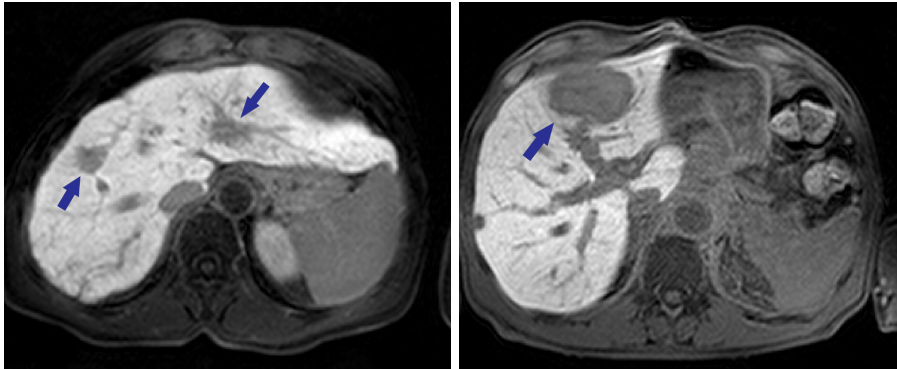


Figure 1.1: Illustration of contrast-enhanced diagnostic images which show colorectal liver metastasis of different sizes.

As part of the HDR BT and in analogy to RFA, one or more flexible, biocompatible plastic catheters are placed through the skin (percutaneously) in the tumor tissue, guided by cross-sectional imaging. For the actual irradiation, a  $3.5 \times 0.7$  mm Iridium-192 radiation source is inserted into the cavity of the applicators inside the tumor by remote control in the afterloading procedure. The Iridium-192 radiation source emits  $\beta$ - and  $\gamma$ - radiation with an average activity of  $3.7 \times 10^9$  Bq and a half-life of 74 days. It typically achieves a dose rate of greater than 12 Gy/h and thus enables an effective irradiation of the tumor tissue within a few minutes. The duration of the complete irradiation depends on the number and size of the lesions treated, but is usually about 1 hour. After the radiation has been completed, the applicators are removed again and the puncture channels are closed with a tissue adhesive. The steep dose gradient of the Iridium-192 radiation source and precise dosimetry based on 3D planning data sets are prerequisites for the precise application of cytotoxic doses in tumor tissue while simultaneously protecting the adjacent liver tissue. The destruction of larger lesions ( $>3$  cm diameter), as illustrated in Figure 1.1, and the use in the surroundings of thermosensitive structures, such as the hepatic porta and bile ducts, are mostly unproblematic (Colletini et al., 2012; Ricke et al., 2004).

In contrast to RFA, the effectiveness of HDR BT is not influenced by perfusion-related cooling effects. The extraordinary regenerative ability of the liver tissue enables the repetitive application of HDR BT in disseminated tumors or interval metastases (Rühl et al., 2010). The efficiency and safety of HDR BT has been demonstrated for primary and secondary liver tumors (Fischbach et al., 2011; Mohnike et al., 2010;

Ricke et al., 2010). Major complications, such as bleeding, bile duct occlusions, or intrahepatic abscesses, are rare after HDR BT and occur in less than 2% of cases (Mohnike et al., 2016). However, the realization of HDR BT requires an intensive cooperation between interventional radiologists and radiation therapists, which could be a reason for the concentration of this method on few specialized centers. Further typical medical applications of HDR BT are treatment of prostate (Gomez-Iturriaga et al., 2016; Prada et al., 2016), breast (Polgár et al., 2004) or lung tumors (Peters et al., 2008).

The aforementioned safety and effectiveness of the percutaneous interstitial interventions results from the precise positioning of the instruments in the target area. Therefore, high performance and high quality image guidance plays a decisive role. At present, the most frequently used imaging modalities for intervention control are sonography and computed tomography (CT). Although magnetic resonance imaging (MRI) is predestined for the control of percutaneous interventions due to its intrinsically high soft tissue contrast, the possibility of image acquisition in multiplanar layer orientation, and the lack of ionizing radiation, it has not yet clinically established itself as the most widely used modality for controlling such interventions. This is due to the fact that for a long time MRI-based interventional planning was technically much more complex than with other modalities and conventional closed MR scanners only allowed very limited access to the patient. Further developments of the MR scanners, which enable better access to the patient and the acquisition of single layer or volume images in the range of seconds, and the increasing availability of MR-compatible instruments, will contribute to the establishment of interventional MRI in the coming years. In principle, two different types of MR scanners are currently available for carrying out MR-guided interventions: MR scanners with an open design by two horizontal or separate magnetic coils - "sandwich" or "double doughnut" design - and MR scanners with conventional tunnel construction. In this thesis, the focus will be on MRI-based treatments of liver tumors carried out with MR scanners with "sandwich" design (see Figure 1.2(a)) as performed at the Department of Radiology and Nuclear Medicine of the University Hospital Magdeburg.

The ability to quickly acquire multiplanar, interventional sequences with frame rates of 1/s increases the safety and effectiveness of the HDR BT, especially in anatomically challenging regions such as the hepatic hilum or in lesions prone to respiratory movements, e.g. in the very deformable left liver lobe. The intravenous application of Gadolinium (Gd)-containing, liver-specific contrast agents such as Gd-EOB-DTPA (Primovist<sup>®</sup>, Bayer HealthCare) simplifies the exact positioning of the applicators even in small hepatic tumors (Fischbach et al., 2011). Gd-EOB-DTPA is an liver-specific contrast agent for hepatic MRI, yielding strong signal enhancement in normal liver parenchyma

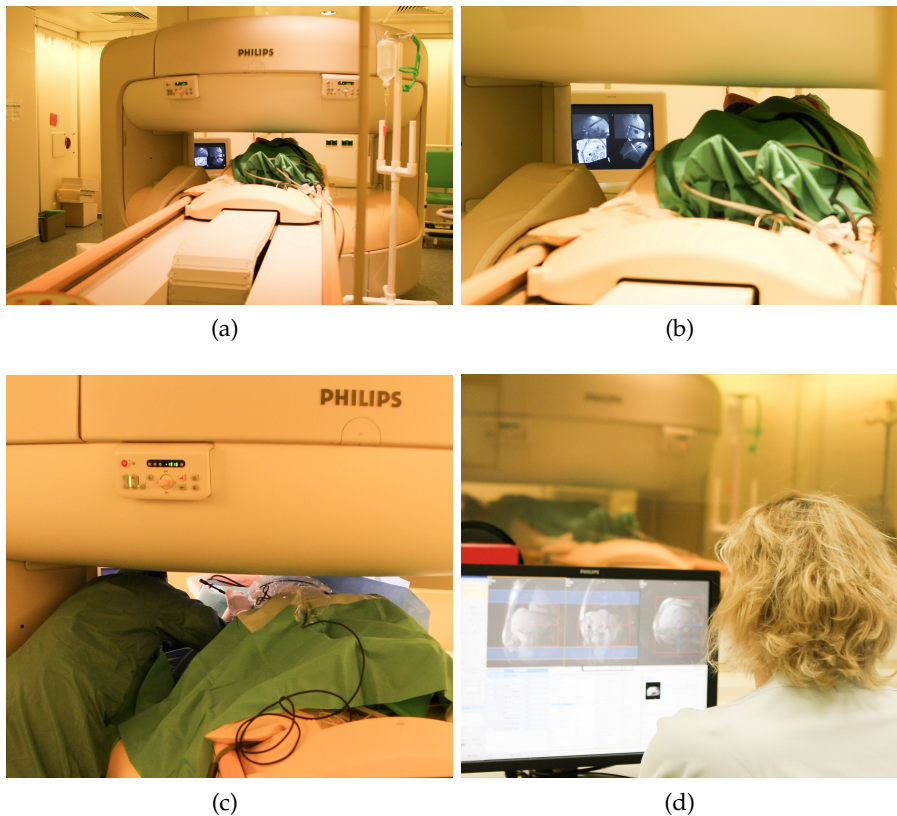


Figure 1.2: Pictures of a [MRI](#)-based treatment as performed at the Department of Radiology and Nuclear Medicine of the University Hospital Magdeburg. (a) Philips 1.0 T Panorama HFO open MR scanner with two horizontal magnet pole shoes. (b) The current orthogonal interventional image slices are shown at the monitor next to the patient. (c) The tumor puncture is performed by the radiologist, who has to lean into the scanner. (d) The desired slice orientation is set with the help of Philips interventional [MRI](#) suite by a [MRI](#) technician in the control room, who communicates by radio with the radiologist.

and absence of signal for focal liver lesions not composed of hepatocytes in delayed T1-weighted MR images. Hence, the detection of liver metastases and other secondary malignant tumors is increased (see [Figure 1.1](#)). The maximum tissue-metastasis contrast is shown in the hepatobiliary phase 10 - 25 min after application of [Gd-EOB-DTPA](#) (Thian et al., 2013). High-resolution, T1-weighted 3D gradient echo (T1w-3D-GRE) sequences in combination with liver-specific contrast agents have become an integral part of oncological image studies for the detection, characterization, and surgical planning of colorectal liver metastases (Choi et al., 2010). Signal enhancement of liver tissue by [Gd-EOB-DTPA](#) lasts for several hours (Frydrychowicz et al., 2012), ensuring consistently high image quality even during time-consuming interventions. With regard to the definition and contouring of the

target lesions during radiation planning, MRI offers clear advantages over CT due to its high soft tissue contrast (Pech et al., 2008; Romero et al., 2012). The reconstruction of the applicators in the MRI radiation planning sequences can be performed with comparable accuracy as in CT data sets (Wybranski et al., 2015).

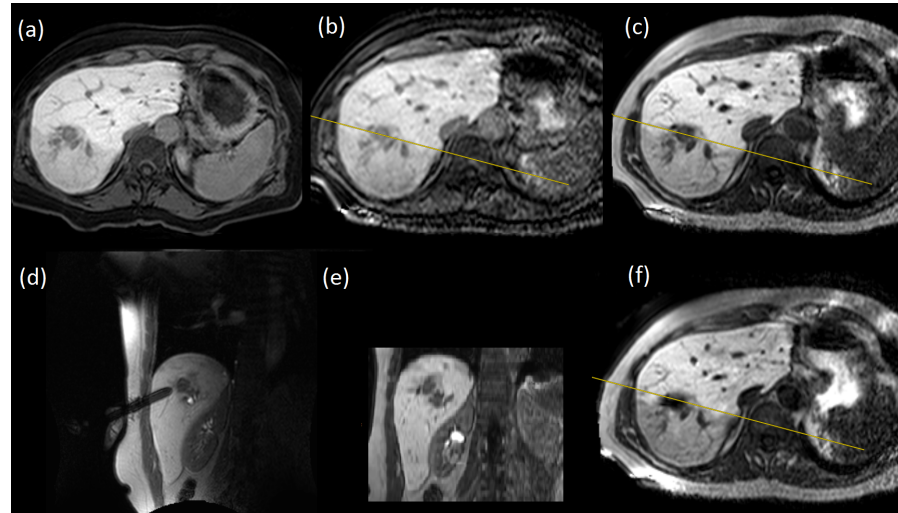


Figure 1.3: Example of different MRI data sets used for HDR brachytherapy of the liver: (a) 3D pre-planning eTHRIVE image acquired in supine position; (b) 3D interventional THRIVE planning image; (c) 3D interventional T1-TFE planning image; (d) 2D interventional T1-FFE slice; (e) 3D multiplanar reconstructed slice of the 3D interventional planning image in (c) at the same location as the 2D interventional T1-FFE slice in (d); (f) 3D post-planning T1-TFE.

In the next sections, the current clinical workflow will be discussed in detail to identify improvement potentials by using computer-assisted methods. In addition, remaining issues and open research questions will be deduced.

## 1.2 CLINICAL WORKFLOW ANALYSIS

In principle, the clinical workflow of HDR BT treatments can be divided into three phases:

**1. Pre-planning:** During the diagnostic pre-planning stage, a T1-weighted, 3D spoiled turbo gradient echo sequence is acquired a few days before treatment, i. e., a contrast (Gd-EOB-DTPA) enhanced T1-weighted high resolution isotropic volume excitation (eTHRIVE) with spectrally adiabatic inversion recovery fat suppression and sensitivity encoding acceleration from a Philips Intera 1.5 T machine. The pre-planning image is usually acquired with the patient in supine position (see Figure 1.3(a)). It is used to assess the extent of metastatic spread to the liver (Elhawary et al., 2010), to extract information such

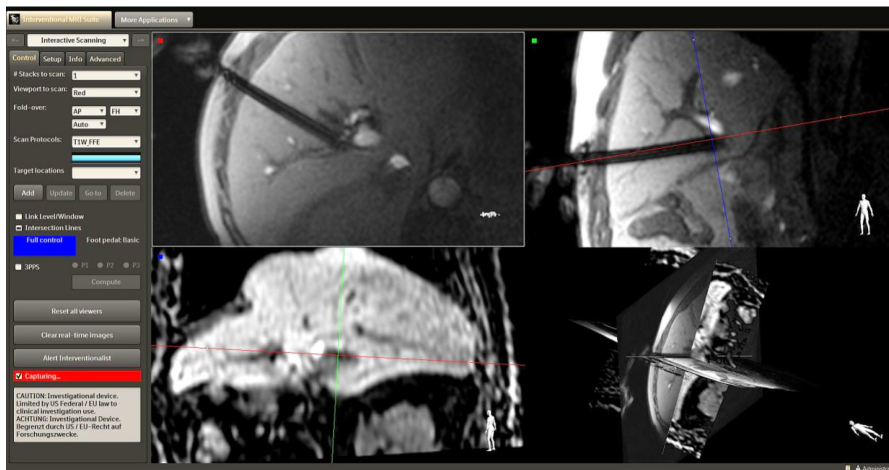


Figure 1.4: Applicator placement is guided by ongoing image acquisition of mutually orthogonal slices. A view of the interventional software called iSuite (Philips Research) is shown, which allows for a quick adjustment of slice orientations according to the trajectory of the puncture needle.

as tumor location and size, and to derive the treatment plan, i. e. the optimal number and trajectory of the applicators.

**2. MRI-guided intervention:** During the interventional stage, the needle insertion or applicator placement is guided by interventional MRI using a Philips 1.0T Panorama HFO open MR scanner. Some steps of this stage are shown in Figure 1.2. At first, several T1-weighted 3D gradient-echo pulse sequences, called interventional planning data sets, are acquired. These are either T1-weighted high resolution isotropic volume excitation (THRIVE) sequences, or T1-weighted turbo field echo (T1-TFE) sequences before and in between applicator placement, as well as after implantation of the last applicator for the final radiation treatment planning (see Figure 1.3(b) and Figure 1.3(c)). During tumor puncture, according to treatment plan, each time (1/s) a 2D interventional image slice, i. e., a T1-weighted fast field echo (T1-FFE) sequence is acquired in mutually orthogonal, arbitrary slice layers (see Figure 1.3(d)). The desired slice orientation is set with the help of Philips interventional iSuite platform (see Figure 1.4) by a MRI technician in the control room (see Figure 1.2(d)). During such interventions, the patient may be placed in decubital position to achieve better access to the tumor or ease the handling of the puncture needles and applicators within the bore of the MRI machine.

**3. Radiation planning and afterloading:** After applicator placement, a 3D post-planning image (either THRIVE or T1-TFE) is used for the radiation planning, which is performed in the Department of Radiotherapy (see Figure 1.3(f)). Brachytherapy radiation planning is implemented within the commercial Oncentra Brachy Treatment Planning System (Version 4.1, Elekta) and includes a contouring of the

planning target volume and organs at risk, a manual reconstruction of the implanted applicators, as well as a graphical or sometimes manual calculation and optimization of the dose distribution. Its main purpose is to cover the minimum required dose values within the target volume and to not exceed maximum dose values in organs at risk. Finally, the optimal treatment plan is validated by analyzing dose-volume histograms and then transferred to the treatment machine, which performs a computer-controlled insertion of an Iridium-192 source by means of a remote-afterloading machine (microSelectron® Digital HDR-V3, Elekta) via several applicators (see Figure 1.5).

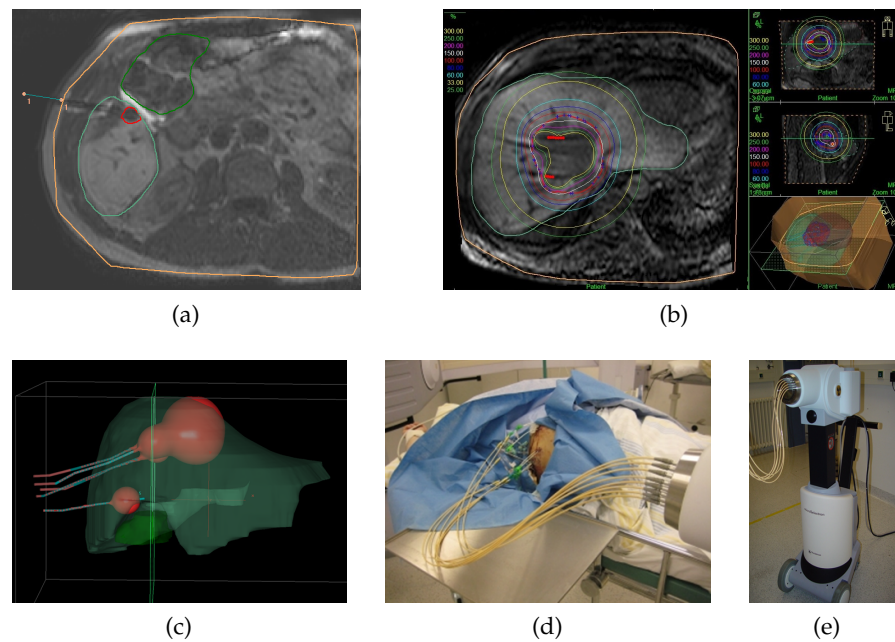


Figure 1.5: Sequential steps of the **HDR BT** post-planning: (a) Manual applicator reconstruction, (b) 2D isocontour view during graphical dose optimization, (c) 3D isosurface view during graphical dose optimization, and (d) insertion of the radiation source through the implanted applicators. Subfigure (e) shows a remote-afterloading machine.

### 1.2.1 Limitations: Liver Intervention

The current workflow has some limitations, which could be strongly improved by means of computer-assistance. A main issue so far is the lack of a computer-assisted pre-planning, which could include among others: a prior placement of virtual applicators, an (semi-) automatic segmentation of target volumes and organs at risk as well as a subsequent hybrid inverse planning optimization (Karabis et al., 2005) on diagnostic images to maximize radiation exposure of the target volumes while minimizing exposure of organs at risk and the healthy liver parenchyma. Pre-planning would greatly reduce the

time exposure to achieve a optimal dose distribution during the dose planning stage (after the intervention). However, it is currently not possible to provide (or transfer) pre-planning information into the interventions.

Due to the poor visibility of the tumor during the puncture, the interventional radiologist has to mentally map the location of the tumor from the 3D diagnostic pre-planning eTHRIVE images to the 3D interventional THRIVE or T1-TFE planning images. This procedure is inconvenient, potentially inaccurate, and time-consuming, because the human ability to mentally map a 3D object into a 3D space is limited (Kim et al., 2011). Moreover, after initial body puncture, 2D interventional T1-FFE images are acquired with a limited time interval of 1/s, to verify the needle position that is advanced to the tumor step by step.

In summary, a computer-assisted transfer of pre-planning information (virtual applicators, target volume contour, organ at risk contours) from 3D pre-planning images onto the 3D interventional planning images (see Figure 1.6), and in a next step onto the 2D interventional slices, would greatly support the interventional radiologist during tumor puncture by reducing the cognitive demands arising from the mental mapping of the pre-planning information. It would also increase the precision of the tumor puncture. First of all, such a transfer would require an accurate volume-to-volume (V2V) registration and secondly, an fast and sufficiently accurate volume-to-slice (V2S) registration. The challenges that arise from spatially aligning (registering) the given 3D diagnostic pre-planning and 3D interventional planning images are as follows:

1. **Deformations:** Often, rigid liver deformations occur because of the different patient positioning between both scans (see Figure 1.6). Due to the patient's respiration and repositioning, non-rigid deformations can also occur in parts of the liver and in the surrounding tissue (e.g. air in the intestines, or different gallbladder filling). The degree of the rigid and non-rigid deformations also varies from patient to patient because the planned applicator configuration, the resulting patient-specific applicator trajectories, patient positioning, and the respiration are individual for each patient.

Suramo et al. (1984) found out that the range of liver movement in the cranio-caudal direction is about 5.5 cm during maximum, 2.5 cm during normal, and 0.9 cm during suspended respiration. During brachytherapy treatments, the liver movement approximately ranges between 1.0 cm during suspended and 2.5 cm during normal respiration. However, it is unknown, how much motion occurs in the bulk of the liver with shallow breathing (Suramo et al., 1984). Hence, a main challenge will be to find a transformation, which can model such non-rigid respiration de-

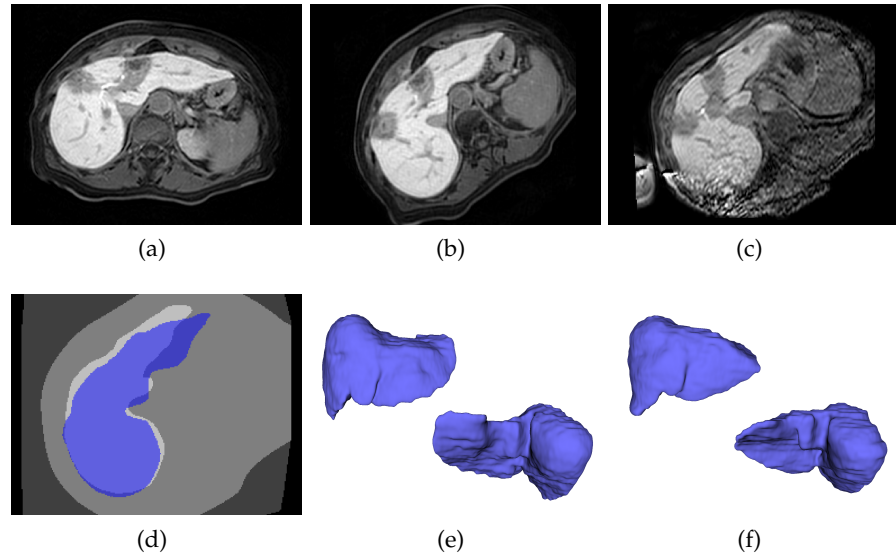


Figure 1.6: Illustration of a typical V2V registration task. The patient is positioned differently during pre-planning and subsequent intervention. A pre planning eTHRIVE image (a) needs to be rigidly aligned (b) with the interventional THRIVE image (c). Non-rigid deformations between both images need to be corrected by a deformable registration, since rigidly transformed liver segmentations only roughly match (d) and liver surfaces reveal large discrepancies of the left liver lobe between pre-planning (e) and interventional image (f).

formations. In the context of liver deformations, the terms *rigid* and *non-rigid* are often used. Regarding the type of registration transformation, there exist several terms in the literature having the same meaning: *non-rigid*, *elastic*, and *deformable*. In this thesis, the term *deformable registration* will be used to compensate for *non-rigid* liver deformations.

2. **Image quality:** In contrast to the pre-planning eTHRIVE data, the image quality of THRIVE and T1-TFE interventional planning images is restricted by the open MRI scanner, i. e. by the low magnetic field strength, and by the limited acquisition time. This results in strong noise, low contrast, a limited field of view, and intensity inhomogeneities, also called partial bias field artifacts in the context of MRI. In the post-planning images, artifacts from already implanted applicators are also present. Exemplary images, which show some of the mentioned aspects, are shown in Figure 1.7.
3. **Validation:** A correct selection of suitable reference structures is essential for a meaningful validation of the accuracy of a registration method. A major issue with real clinical data sets in medical image analysis is the precise identification of corresponding ref-



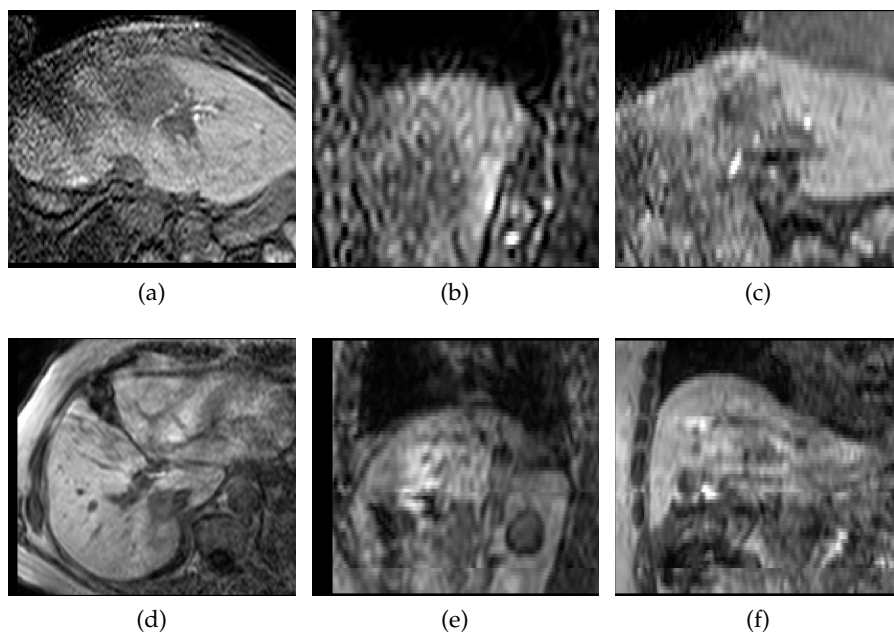


Figure 1.7: Challenging examples of 3D interventional **THRIVE** (a-c) and **T1-TFE** (d-f) planning images. Both types of images show a partly strong noise in some regions, intensity inhomogeneities, and in general a lower resolution than pre-planning images. Anatomical planes from left to right are as follows: axial, sagittal, coronal.

erence structures in both data sets. Often, a medical field expert is needed to perform this task. However, contouring of the liver and tumors as well as setting anatomical landmarks is always a time-consuming and error-prone task for 3D data sets.

If the listed challenges above would be addressed successfully, an adequate transfer of the already transformed 3D pre-planning information onto 2D interventional image slices could be considered in a next step. This would further support the accuracy of the tumor puncture during **MRI**-guidance, e. g., by overlaying virtually placed applicators or displaying planned applicator trajectories, and contours of the target volumes and organs at risk.

The challenges of spatially aligning 3D interventional planning images and 2D interventional slices are as follows (see Figure 1.3 and Figure 1.4):

1. **Spatial and temporal resolution:** In contrast to the 3D interventional **THRIVE** or **T1-TFE** planning images, interventional **T1-FFE** images are only two-dimensional. This is caused by the fact that a continuous, fast image acquisition is required to perform a sufficiently precise tumor puncture. However, the temporal resolution is only 1/s and not sufficient to create an accurate respiratory model of the liver. Both limitations create high degrees of freedom for a **V2S** registration task.

**2. Deformations:** Both images – 3D interventional **THRIVE** or **T1-TFE** planning images and 2D interventional **T1-FFE** image slices – are acquired within the same open **MRI** scanner and the patient is usually not repositioned. This means that both scans also hold same scanner coordinates and that rigid liver deformations are minimal. However, much of the deformation of the liver in the interventional **T1-FFE** images occurs due to continuous respiration and results in tumor displacements and motion artifacts during the needle insertion. To compensate for respiration, information about the strength and intervals would be needed, e.g. by means of a breathing belt or a previous acquisition of various 3D interventional planning images at different respiratory moments. Such information would allow the creation of a 4D respiratory model of the liver. Unfortunately, this information is not recorded within the current clinical workflow and cannot be used for the present registration task.

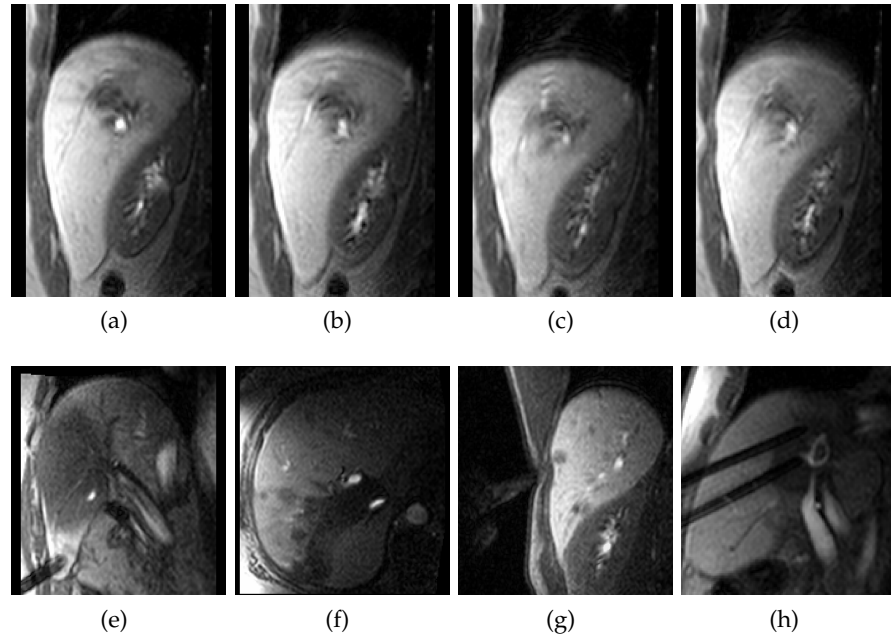


Figure 1.8: Illustration of 2D interventional **T1-FFE** images. Sub-figures (a-d) show liver deformations at different respiration moments. Sub-figures (e-h) show challenging examples including (e) tissue inhomogeneities, (f) strong bias field, (g) small deformations due to finger (and needle) puncture, and (h) artifacts caused by already implanted applicators.

**3. Image quality:** Challenges arise due to the poor image quality, which is limited by the open **MRI** scanner and by the required fast image acquisition. Among other things, this includes a small field of view (**FOV**), low contrast (compared to pre-planning images), partial bias field artifacts, and artifacts caused by al-

ready implanted applicators and inserted needles. Some of the challenges mentioned are exemplarily illustrated in Figure 1.8.

4. **Validation:** As with the V2V registration, reference structures are also required for the V2S registration. To identify such structures in the 2D interventional T1-FFE images is even more challenging, because of the two-dimensionality and low contrast. Moreover it is not possible to find structures in every single slice as the time required for this would be enormous. The main challenge at this point is the selection of a suitable number of criteria in order to measure the accuracy of the V2S registration sufficiently.

If the challenges just mentioned would be addressed successfully, an overlay of pre-planning information onto 2D interventional image slices could be easily performed. This would greatly support the accuracy of the tumor puncture during MRI-guidance and allows for transferring pre-planning information to post-planning images as well. Such information could be directly used for the radiation treatment planning by the radiation therapist.

### 1.2.2 Limitations: Radiation Treatment Planning

The objectives of brachytherapy treatment planning are first of all to protect the surrounding normal tissue and organs at risk from excessive radiation and to deliver a sufficiently high dose in the tumor tissue. During treatment planning, the challenges for the radiation therapist are: to determine the number and location of implanted applicators and source dwell points within the 3D post-planning image as well as to find the optimal dwell times for each source dwell point, so that the final dose distribution is as close as possible to the desired dose distribution (see Figure 1.9).

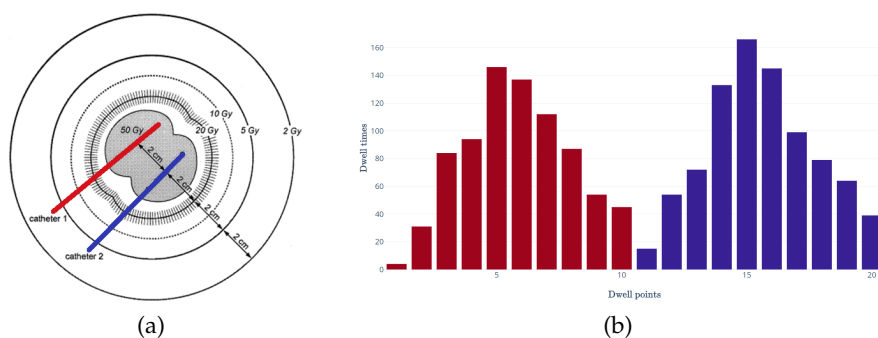


Figure 1.9: Illustration of an (a) optimal applicator placement including isocontours of the dose distribution and (b) of the corresponding dwell time configuration for a given target volume. The radiation therapist often has to manually optimize the dwell times (b) to achieve an optimal and sufficient dose distribution (a).

Moreover, a manual reconstruction of the implanted applicators and a new contouring of the target volumes and organs at risk, which are needed for the optimization task, are very time-intensive. It can be seen in Figure 1.10 and Figure 1.3(d), that implanted applicators cause broad, dark signal voids within the image. The width of the artifact is heavily dependent on the direction of the needle or applicator relative to the static magnetic field. Here, a fast (semi-)automatic applicator reconstruction could further support the radiation therapist.

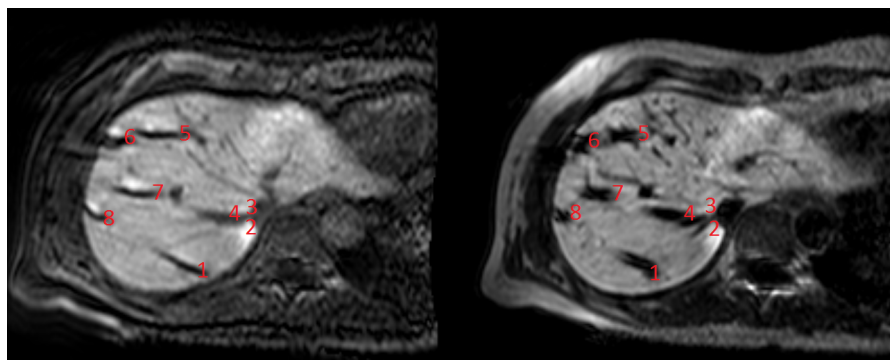


Figure 1.10: Exemplary axial slices of the 3D post-planning **THRIVE** (left) or **T1-TFE** (right) images including implanted applicators. Applicators are displayed as susceptibility artifacts, which result in quasi linear signal voids. They must be manually reconstructed by a radiation therapist, which can be very time-consuming depending on the number and position of the applicators.

A main issue during the current clinical workflow is the fact that the number, location, and orientation of applicators is already fixed during the post-planning, which complicates a quick automatic optimization of the treatment plan. As a result, a time-consuming manual (by direct dwell point time manipulation) or graphical (by isocontour manipulation) dose optimization must be performed, which often includes a lot of trial and error. An early determination of an optimal number of applicators, e. g. already during the pre-planning phase, could strongly improve the optimization time and accuracy of the treatment plan, as a reduction of the number of applicators as well as more suitable locations of the applicators would simplify the treatment plan in terms of time and complexity. As a result, the whole **HDR BT** would be even less invasive for the patient and would reduce the possibility of treatment errors.

Summarizing the last section shows that there is a lot of potential to improve the current **HDR BT** workflow by means of computer-assistance. Since this thesis cannot address all of these issues, I will focus mainly on the registration parts. Before I define the aims and objectives of this thesis, the related work and state-of-the-art will be described in detail.

In general, there exists no uniform or common classification or grouping of image registration procedures. The present thesis is mainly oriented to the surveys of Holden (2008) and Sotiras et al. (2013). According to their work, registration deformations can in principle be divided into physics-based, interpolation-based, and knowledge-based geometric transformations whereby some deformation models can also be assigned to more than one group.

In accordance with the work of Modersitzki (2004), deformations derived from physical models can be further subdivided into elastic body models (Bajcsy and Kovačič, 1989; Broit, 1981), viscous fluid models (Bro-Nielsen and Gramkow, 1996; Christensen et al., 1994), diffusion models (Thirion, 1996, 1998), also called demons-based models, curvature-based models (Fischer and Modersitzki, 2003), and flows of diffeomorphisms (Dupuis et al., 1998; Trounev, 1998), also called large deformation diffeomorphic metric mappings (LDDMMs).

Interpolation-based deformations are based on the fact that transformations smoothly approximate the known displacements rather than taking the exact same values and thus having low degrees of freedom. The most common types of interpolation-based deformations are thin plate splines (TPSs) (Bookstein, 1989) based on radial basis functions (RBFs) (Zagorchev and Goshtasby, 2006), elastic body splines (Davis et al., 1997), and free-form deformations (FFDs) (Rueckert et al., 1999). In the medical image analysis community, the term deformable B-spline registration gained a wide acceptance and is often associated with FFDs, where interpolation is performed by cubic B-splines over a regular image grid.

Knowledge-based geometric deformations can be further classified into statistically-constrained geometric transformations, where a high dimensional statistical deformation model (SDM) is learned and biophysically-inspired deformations, which are using knowledge of the deformability of target tissues to construct biophysical deformations. The former often use a principal components analysis (PCA) to model the deformation (Wouters et al., 2006). The latter differ from the physics-based models mainly in that they are closely related to anatomy and physiology. Often, finite element methods (FEMs) are used in this context to model such properties (Azar et al., 2001).

Regarding the matching criteria, also called similarity metrics or similarity measures, there exist a couple of different classes dependent on the image features used for the specific registration task. Geometry-based methods are looking for the best possible transforma-

tion between corresponding feature points derived from the images. Hence, these techniques always require additional preprocessing of the images in order to enable the creation of surface points, edge points, or landmarks from the target organ. On the other hand, voxel-based or intensity-based methods, also called iconic methods, quantify the alignment of the images by evaluating a similarity criterion over the whole image domain. The best known similarity measures are mean absolute difference (MAD), sum of squared differences (SSD), normalized cross-correlation (NCC) (Brown, 1992), mutual information (MI) (Collignon et al., 1995; Viola and Wells, 1997), normalized mutual information (NMI) (Studholme et al., 1999), Mattes mutual information (MMI) (Mattes et al., 2001), or gradient image-derived measures such as normalized gradient fields (NGFs) (Haber and Modersitzki, 2006).

Optimization methods can be divided into two categories based on the type of variables they attempt to derive: continuous and discrete. The former class of methods solves optimization problems where the variables assume real values. In this context, optimization is often performed by (stochastic) gradient descent, conjugate gradient methods, Quasi-Newton methods like limited-memory Broyden–Fletcher–Goldfarb–Shanno (LBFGS), Gauss-Newton method, Levenberg-Marquardt algorithm, or Powell’s conjugate directions method. The latter class solves the problem that the variables take values from a discrete set, which is often represented by a Markov random field (MRF) (Tang and Chung, 2007). For a more detailed overview of common registration deformations, similarity measures, and optimizers please refer to the survey of Sotiras et al. (2013).

In the domain of MRI-based liver registration, previous works often use a combination of rigid and deformable registration. Rigid registration is applicable if the difference between both images can be expressed by translation and rotation. If local tissue movement is not negligible, e.g., due to deformations caused by respiratory motion, different patient positioning, or liver mass changes over time, deformable registration is needed.

First approaches were based on a simple manual alignment (Wilson et al., 1998), which can however be cumbersome in 3D data sets. Later, Carrillo et al. (2000) and Lee et al. (2005) used to formulate rigid registration into an optimization problem that can be solved by gradient descent.

To express the tissue deformation of the liver, related publications most often used FFDs based on cubic B-splines (Elhawary et al., 2010; Fernandez-de-Manuel et al., 2014; Lange et al., 2005; Rohlfing et al., 2004; Tang and Wang, 2010; Tokuda et al., 2015), linear elastic FEMs (Archip et al., 2007; Brock et al., 2006), geometric surface deformations (Kadoury et al., 2012; Kaus et al., 2007; Liu et al., 2013), TPSs (Böttger

et al., 2003; Foruzan and Motlagh, 2015), and MRFs (Mahapatra and Sun, 2012). To judge the quality of the deformation, image similarity measures such as MI (Elhawary et al., 2010; Lange et al., 2005), its normalized variants (Archip et al., 2007; Brock et al., 2006; Rohlfing et al., 2004; Tokuda et al., 2015) and gradient image-derived measures (Liu et al., 2013; Mahapatra and Sun, 2012) were mainly used.

Since there exist only a few studies that register between pre-planning MRI and interventional MRI liver data, papers that register from pre-planning MRI to interventional CT or ultrasound (US) data or vice versa are also included in the analysis. As a complement, promising selected deformable registration approaches from other medical application fields will be explained, which could be applied (with some adaptation) to liver registration in MRI. In the following sections, a more detailed description and comparison of related works is provided. An overview and a classification of the papers described can be found in Table 2.1 with the focus on pre-planning data of the liver and in Table 2.2 with the focus on interventional liver data.

## 2.1 RELATED WORK: LIVER REGISTRATION OF PRE-PLANNING DATA

As presented by Carrillo et al. (2000), image-based registration is superior in quality compared to manual registration for registering different MRI-sequences (T1, T2, T1-weighted Gd-DTPA enhanced; resolution: about  $1.5 \times 1.5 \times 5 - 10$  mm) during MRI-guided RFA of liver cancer at different time points (pre-planning, interventional, and several follow-up images), but it is also prone to failure if the initial translation and rotation is not close enough to the anticipated transform. In their cases, MI gave better results than entropy, correlation, and variance of gray-scale ratio. A final registration accuracy of about 3 mm between anatomical landmarks was achieved with both, manual and MI-based methods for cases where the registration did not fail. MRI images were acquired using a clinical 0.2-T C-arm machine.

Later, multi-resolution approaches were introduced, which are less prone to get stuck in the wrong local optima. In Lee et al. (2005), a multi-resolution, voxel-similarity-based registration algorithm (from the open-source Insight Segmentation and Registration Toolkit (ITK)) was selected as a baseline registration method. Evaluation was performed on multiple T2-weighted, and pre- and post-contrast T1-weighted images of the abdomen. Their results showed a target registration error (TRE) of 8.2 mm for MRI-MRI registration and 14.0 - 18.9 mm for MRI-CT registration between automatically selected landmarks. They justify their high error rates with the very high slice thickness of 5 - 10 mm of their MRI images.

Rohlfing et al. (2004) presented a technique for modeling liver motion during the respiratory cycle using intensity-based nonrigid

Table 2.1: Overview of related works in the domain of pre-planning MRI liver registration. For each reference, the table compares (from left to right) the kind of image modality (CT, MRI), transformation type  $T_{type}$  (rig.: rigid, deform.: deformable), transformation model  $T_{model}$  (FFGD, TPSs, FEMs, FFSD), registration metric (MI, NMI, SSD, NCC, PD) as well as the computation times  $t_c$ (s), number of data sets, validation criteria (LMs: anatomical landmarks, SPs: surface points, EPs: edge points), and TREs(mm). The symbol '-' indicates that no information has been provided by the reference.

Reference	Modality	$T_{type}$	$T_{model}$	Metric	$t_c$ [s]	# Data	Val. Crit.	TRE [mm]
Carrillo et al. (2000)	MRI-MRI	rig.	–	MI, NCC	–	17	LMs	~ 3.0
Rohlfing et al. (2004)	MRI-MRI	deform.	FFGD	NMI	–	4	SPs , LMs	2.5 to 5.1
Lee et al. (2005)	MRI-CT	rig.	–	MI, PD	–	–	LMs	~ 8.2
Lange et al. (2005)	CT-MRI	deform.	FFGD	NMI	–	5   5	LMs	2.3 to 2.6
Brock et al. (2006)	CT-MRI	deform.	FEM	–	8	5	LMs	$4.2 \pm 1.4$
Voroney et al. (2006)	CT-MRI	deform.	FEM	–	–	17	LMs	$4.2 \pm 1.7$
Kaus et al. (2007)	CT-MRI	deform.	FFsD	–	10	5	SPs , LMs	$0.6 \pm 4.3$
Fernandez-de-Manuel et al. (2014)	CT-MRI	deform.	FFGD	OF-MI	–	7	SPs LMs	$3.2 \pm 0.2$ $7.1 \pm 1.9$



registration of gated MRI images. Global motion was modeled by a rigid transformation. Local motion was modeled by a FFD based on B-splines. Their approach was tested on MRI images (1.5-T; resolution: about  $1.5 \times 1.5 \times 5$  mm) of four healthy patients and achieved a TRE of about 3 mm, which was evaluated using different anatomical landmarks as well as surface points from isocontours.

Another application of deformable image registration of the liver in MRI was presented by Lange et al. (2005). Non-rigid deformations were modeled by multilevel cubic B-splines to register pre-planning CT and MRI data (resolution:  $0.6 \times 0.6 \times 2.5$  mm) for computer-assisted preoperative planning of surgical procedures. Evaluation was performed on MRI images of five patients using a closest point distance measure between vessel centerlines, resulting in final TREs of 2.3 - 2.6 mm.

Brock et al. (2006) proposed a multiorgan deformable image registration technique based on FEMs. It was demonstrated on pre-planning CT and MRI images (resolution about:  $0.14 \times 0.14 \times 0.8$  mm) of five liver cancer patients and they achieved an average TRE of  $4.2 \pm 1.4$  mm between CT and MRI, based on four to five vessel bifurcations identified by an experienced radiation oncologist. The average time required to perform the complete multiorgan deformable image registration process was about 50 min, but single-organ deformable registration can be completed in about 2 min.

Voroney et al. (2006) applied the proposed method of Brock et al. (2006) to diagnostic pre-planning CT and MRI (contrast-enhanced T1-weighted, dual-echo, and T1-weighted) images of 17 patients. Accuracy measurement was performed using five pairs of anatomical landmarks in both images. Finally, they achieved a TRE of  $4.2 \pm 1.7$  mm, which is similar to the results of Brock et al., 2006 and less than the slice thickness of their MRI data (6 - 8 mm).

Kaus et al. (2007) deformably registered contrast-enhanced CT and high-resolution MRI using a surface-based registration. They derived a volumetric deformation field based on the surface deformations of the liver as alternative to FEM-based methods. Evaluation was done on five patients, between four to six corresponding vessel bifurcations. They finally reported poorly interpretable TREs (because of very high standard deviations) of  $0.6 \pm 4.3$  mm and a computation time of about 10 s.

Recently, an organ focused extension of MI was proposed by Fernandez-de-Manuel et al. (2014) to improve quality and robustness of the registration by adding spatial information, benefiting from the availability of expert liver segmentations in clinical protocols. Their proposed organ-focused MI (OF-MI) criterion extended the joint histogram with an additional information channel, similar to the one proposed in Studholme et al. (1996). Moreover, they extended its implementation to a deformable, B-spline based, multimodal registration

framework. Validation of their system was performed on 63 simulated volumes as well as on seven real subjects, each comprising a pre-planning contrast-enhanced portal-phase CT and pre-planning eTHRIVE (resolution: about  $1.0 \times 1.0 \times 2.0$  mm). An improvement of the registration accuracy for OF-MI as compared with MI was found for both, simulated and real data sets. For real data sets, they observed a landmark-based TRE of  $7.55 \pm 2.09$  mm after MI registration and  $7.07 \pm 1.88$  mm after OF-MI registration as well as a surface-based TRE of  $3.68 \pm 1.00$  mm after MI registration and  $3.20 \pm 0.2$  mm after OF-MI registration.

Further related work in the field of liver registration of pre-planning MRI data is available with regard to respiratory motion correction in dynamic contrast enhanced (DCE-)MRI. However, motion correction is a slightly different task as it is usually only performed on the same data set without changing the position or the MRI scanner. For this reason, these papers will not be discussed.

## 2.2 RELATED WORK: LIVER REGISTRATION OF INTERVENTIONAL DATA

Only some of the related works register onto 3D or 2D interventional data of the liver, where the acquisition quality is typically limited compared to non-interventional settings due to time and other constraints. In particular, Archip et al. (2007), Böttger et al. (2003), Elhawary et al. (2010), and Tokuda et al. (2015) apply deformable registration between 3D pre-planning MRI and 3D interventional CT images, while Foruzan and Motlagh (2015), Liu et al. (2013), and Tang and Wang (2010) investigate the opposite direction and register 3D pre-planning CT and 3D interventional MRI images deformably. Other studies have mainly investigated deformable registration of 3D pre-planning MRI onto interventional 3D US data (Cha et al., 2017; Kadoury et al., 2012; Lange et al., 2003; Mauri et al., 2015).

Warfield et al. (2000) first introduced a combined segmentation and deformable registration for two intraoperative MRI liver data sets during percutaneous cryotherapies of liver tumors. But the main focus of their work was segmentation and they did not propose any quality or accuracy values regarding their registration.

Lange et al. (2003) defined the need for a fast deformable registration procedure to display pre-planning information on intraoperative data for liver surgery. They introduced a novel deformable registration method that combines an iterative closest point (ICP) algorithm and multilevel B-splines based on semi-automatically extracted vessel centerline points in contrast-enhanced MRI and CT as well as intraoperative US. However, their approach was only evaluated on three

Table 2.2: Overview of related works in the domain of interventional MRI liver registration. For each reference, the table compares (from left to right) the kind of image modality (CT, MRI, US as well as interventional CT, MRI), transformation type  $T_{\text{type}}$  (rig.: rigid, deform.: deformable), transformation model  $T_{\text{model}}$  (FFGD, TPSs, FEMs, FFSD), registration metric (MI, NMI, SSD, NCC, PDs), computation times  $t_c$  [s], number of data sets, validation criteria (LMs: anatomical landmarks, EPs: edge points, SPs.: surface points), TRE and DSC values. The symbol ‘-’ indicates that no information has been provided by the reference.

Reference	Modality	$T_{\text{type}}$	$T_{\text{model}}$	Metric	$t_c$ (s)	# Data	Val. Crit.	TRE [mm]	DSC(%)
Böttger et al. (2003)	MRI - iCT	deform.	TPS	MI	–	2	LMs	15	–
Archip et al. (2007)	MRI - iCT	deform.	FEM	–	$\sim 300$	13	EPs	1.6	–
Elhawary et al. (2010)	MRI - iCT	deform.	FFGD	MI	$\geq 600$	5	SPs	3.3	0.97
							LMs	4.1	–
Tokuda et al. (2015)	MRI - iCT	deform.	FFGD	MI	88	14	SPs	$13.1 \pm 5.2$	$0.88 \pm 0.03$
Tang and Wang (2010)	CT - iMRI	deform.	FFGD	MI	$\sim 1100$	7	SPs	–	0.87
Liu et al. (2013)	CT - iMRI	deform.	FFSD	PD	–	20	LMs	$4.3 \pm 1.9$	–
Foruzan and Motlagh (2015)	CT - iMRI	deform.	TPS	PD	$\sim 540$	18	LMs	$12.0 \pm 4.9$	$0.78 \pm 0.07$
Lange et al. (2003)	MRI/CT - US	deform.	FFGD	PD	$\leq 900$	3	LMs	1.7	–
Kadoury et al. (2012)	MRI - US	deform.	FFSD	PD	44	4	LMs	$3.7 \pm 0.69$	–
Mauri et al. (2015)	MRI/CT - US	deform.	–	–	$\geq 300$	215	SPs	$\leq 5$	–
Cha et al. (2017)	MRI/CT - US	deform.	–	–	29	22	SPs	3.75	–

patients and reached a **TRE** of about 1.7 mm and a computation time of about 15 min.

Böttger et al. (2003) introduced a combined **MI**-based rigid and **TPS**-based deformable registration approach to register two different pre-planning **MRI** and interventional **CT** liver data sets during stereotactic single-dose radiation therapy treatments. Their quality was measured using distances between manually selected anatomical landmarks like tumor centers and vessel bifurcations. Finally they achieved a **TRE** of about 15 mm.

Archip et al. (2007) proposed a novel **FEM**-based method to fuse 3D pre-planning **MRI** images (1.5 T; resolution:  $1.36 \times 1.36 \times 2.5$  mm) with 3D interventional **CT** images (resolution:  $0.61 \times 0.61 \times 2.5$  mm) of the liver for improved targeting of tumors during liver **RFA**s. They compared its performance with conventional rigid registration and two deformable registration methods: B-spline and Demons on 13 subjects. In an initial step, a rigid registration was performed, based on an **ITK** implementation of **MI**. They demonstrated **TRE**s between the edges of anatomical landmarks of the liver of 12.2 mm for rigid, 2.4 mm for B-spline, 3.0 mm for demons, and 1.64 mm for their **FEM**-based deformable registration method. The average computation times were 1 min for rigid, 10 min for B-spline, 6 min for demons, and 5 min for their proposed technique.

Another deformable image registration procedure was presented by Elhawary et al. (2010) to enhance tumor visualization and localization during **CT**-guided liver tumor cryoablation procedures of five patients between pre-planning, contrast enhanced **MRI** images (1.5 T; resolution:  $7.8 \times 7.8 \times 2.5$  mm) and interventional unenhanced **CT** images (slice thickness: 3 mm). They used a staged approach of manual rigid, affine, and deformable B-spline registration with **MI** as similarity criterion. Their deformable registration took an average of 4 - 11 min, depending on the images and they reached **TRE**s of about 4.1 mm between selected anatomical landmarks and a Dice similarity coefficients (**DSC**s) of 0.97. The final computation time of their approach ranged between 9.4 - 43.9 min (including the whole liver segmentation process).

Tang and Wang (2010) applied a two-step approach to six pre-planning **CT** (resolution:  $0.6 \times 0.6 \times 3 - 7$  mm) and interventional **MRI** (0.5 T, resolution:  $1.17 \times 1.17 \times 5$  mm) liver data sets. First, they used a parametric active contour to segment liver boundaries in **CT** and **MRI** data. Secondly, they applied an affine and **FFD** with B-splines to their masked liver data sets. They achieved an average tumor **DSC** of 0.87 and the average runtime of their combined segmentation and registration was about 18 min.

Kadoury et al. (2012) presented a combined rigid and a deformable surface-based registration approach for pre-planning **MRI** and interventional **US** images during **RFA** treatments of liver tumors. Their

main contribution was the training of a shape-constrained deformable model for an unsupervised liver segmentation in MRI images. They presented registration results for only four patients and finally achieved a TRE of 4.3 mm between manually selected anatomical landmarks on hepatic bifurcations.

Liu et al. (2013) proposed a novel geometry-based deformable registration approach for registering pre-planning CT (resolution:  $0.74 \times 0.74 \times 2.0$  mm) and MRI (resolution:  $1.19 \times 1.19 \times 2.5$  mm), interventional MRI (resolution:  $1.13 \times 1.13 \times 5.0$  mm), and several follow-up MRI images. They used a 3D surface-based model as guidance and up to four landmarks placed at vessel bifurcations in the liver were used as a gold standard for evaluating registration results. Finally, they compared their active-surface approach (TRE of  $4.3 \pm 1.9$  mm) with an affine MI-based registration (TRE of  $3.2 \pm 1.2$  mm) on twenty patients treated by routine brachytherapy. Their average TRE increased to  $11.9 \pm 5.6$  mm for follow-up registration cases. Finally, they concluded that their approach has limitations in cases where internal liver deformation is present.

A graphics processing unit (GPU)-based approach for the registration of pre-planning MRI and interventional CT for CT-guided tumor ablations was proposed by Tokuda et al. (2015). They implemented a plugin for the open source software 3D Slicer and compared their proposed GPU-based B-spline method to the standard B-spline method using NMI and a LBFGS optimizer with simple bounds. For evaluation, they measured DSC and Hausdorff distances (95%) between liver surface points and finally achieved a DSC of  $0.88 \pm 0.03$  and mean Hausdorff distances of  $13.1 \pm 5.2$  mm. However, they concluded that in terms of computation time their approach reached little to no improvement over standard B-splines with regard to the deformable registration part.

An alternative to similarity-based registration was presented by Foruzan and Motlagh (2015), who extracted meaningful points semi-automatically from the images and matched the point sets deformably. First, maximum intensity projections (MIPs) of 18 pre-planning CT (resolution:  $0.6 \times 0.6 \times 3-7$  mm) and interventional MRI (0.5 T, resolution:  $1.17 \times 1.17 \times 5$  mm) data sets were registered in 2D, and the corresponding rigid transformation parameters were used to align 3D images in axial, coronal, and sagittal planes. Use of MIPs should compensate for intensity inhomogeneities inherent in the interventional MRI data. In a next step, they used a PCA to align 3D pre-planning CT and 3D interventional MRI data sets. Then, the corresponding translation and rotation parameters were used to increase the global registration accuracy. Finally, a modified deformable, TPS robust point matching algorithm was developed to accommodate local liver deformations. Manually extracted surface points on the liver and branching points of the portal veins were used as input. They compared their automated

registration algorithm with both rigid and deformable methods. Eventually, Hausdorff distances of  $42.00 \pm 20.7$  mm and  $22.5 \pm 21.28$  mm as well as TREs of  $12.02 \pm 4.99$  mm and  $10.11 \pm 8.75$  mm were achieved for the liver and tumor. The DSC of liver and tumor were increased from  $0.39 \pm 0.18$  and  $0.00$  to  $0.78 \pm 0.07$  and  $0.27 \pm 0.14$ , respectively. However, they stated that the combined runtime of their approach was about 540 s, which is very high in an interventional setting and the main drawback of this method.

One of the most recent studies (Mauri et al., 2015) showed that with regard to US data, there is already commercial software available that can register pre-planning MRI on interventional, real-time US during RFAs. Drawback of the proposed method is the required manual adjustment of internal anatomic markers before the registration and the long pre-registration time of 5 - 20 min which is required for the real-time fusion. To evaluate their method, they performed a registration on 215 cases with the exception that a large part (about 182 tumors) of the data had to be excluded due to insufficient distinction in the tumor echogenicity from the surrounding tissue or lack of detection because tumors were located in areas which are not accessible to US. Unfortunately, the paper does not reveal any further information regarding the registration algorithm used (because it is commercial) or regarding the accuracy of their method. They finally proposed a success rate of about 90.2 % which includes all cases with a TREs smaller than 5 mm. A very similar approach was used by Cha et al. (2017) who achieved a mean TRE of about 3.75 mm (1 - 15.8 mm) with an average runtime of 28.5 s (18 - 47 s) on 22 patients who received RFA.

In contrast to V2V registration and to the best of my knowledge, there is currently no related work for V2S registration on 2D interventional MRI liver data. Few related works proposed only rigid approaches for the V2S registration of 3D pre-planning CT and 2D interventional, fluoroscopic CT liver data (Birkfellner et al., 2007; Lasowski et al., 2008; Micu et al., 2006), or for other target organs, e. g. prostate cancer (Fei et al., 2003). Ferrante and Paragios (2017) presented a detailed survey for slice-to-volume registration in medical image analysis, where several application areas and registration concepts are described.

### 2.3 SELECTED REGISTRATION METHODS

Obviously, there also exist many deformable registration approaches which did not focus on MRI-based liver registration. Since it would clearly go beyond the scope of this thesis, the focus will be on some selected, promising approaches.

Mahapatra and Sun (2012) proposed a method to exploit segmentation information for deformable image registration using a MRF-

based objective function. They used a multiscale graph-cut approach to achieve subpixel registration and to reduce computation time (similar to Glocker et al. (2008)). Although they did not apply their method to different MRI liver sequences, their method seems to be promising in terms of computational efficiency. Their approach was tested on 3D liver perfusion data (110×80×28 slices, resolution: 1.6×1.6×4 mm) and achieved an average DSC of 0.91 for simulated deformations.

Another promising approach was presented by Pace et al. (2013), who developed a deformable image registration algorithm that uses anisotropic smoothing for regularization to find correspondences between images of sliding organs, e. g., like the liver. In particular, their algorithm uses locally adaptive diffusion tensors to determine the direction and magnitude with which to smooth the components of the displacement field that are normal and tangential to an expected sliding boundary. They argued that conventional regularizers of deformable registration approaches enforce smooth transformations, and therefore are inaccurate near the discontinuous motion that occurs when multiple organs, like the liver and neighboring organs, move independently. Furthermore, globally smoothing regularizations will underestimate motion near such sliding boundaries by averaging discontinuous motions, and/or incorrectly smooth motion onto static structures. Unfortunately, the approach needs a segmentation of the sliding boundaries on the target/fixed images, which is not available for the interventional data before the registration.

Papież et al. (2014) proposed an implicit sliding-motion preserving regularization via bilateral filtering for deformable image registration, which works similar to the approach of Pace et al. (2013). In contrast, Papież et al. (2014) stated that their framework does not require any explicit prior knowledge about the organ motion properties, e. g., segmentation. As the deformable registration algorithm, they used a vector-valued demons approach which incorporates a NGF. Validation was performed on synthetic and clinical 4D lung CT data sets.

Recently, Luu et al. (2016) presented a deformable registration for CT-guided ablation of liver tumors. Although they concentrated on CT-guided RF ablations, their application and existing problems are similar to mine since they registered 3D diagnostic pre-planning images with 3D interventional images deformably. In their study, they used Elastix, a free registration software package, to apply the deformable registration. In particular, a simple B-spline approach combined with MI as similarity criterion was used. Finally, they achieved a DSC of  $0.91 \pm 0.03$  and a mean TRE of  $4.6 \pm 1.8$  mm between liver surfaces, and a TRE of  $5.3 \pm 2.5$  mm between anatomical landmarks placed into liver vessels for the remaining 16 CT scans. However, some of the CT images were excluded for the quality measuring or had to be manually post-processed.

Recent publications focused mainly on short registration times, e. g., Peterlík et al. (2018), who proposed a geometry-based registration as combination of linear elasticity and ICP for pre-interventional and interventional CT data using a detailed 3D model of the liver and its internal structure combined with liver surface information extracted from the interventional CT. They presented their results on nine real data sets and achieved a TRE of 4.5 mm. Computation time of their registration was less than 1 min but semi-automatic segmentation of the liver in the interventional CT took about 10 min.

As deep learning plays an increasingly important role in medical image analysis, there are also first studies in the field of image registration of medical image data.

Wu et al. (2013) proposed an unsupervised deep learning method using an adopted stacked convolutional independent subspace analysis method to directly learn hierarchical representations for image patches from MRI brain images. They integrated their learned features into a multi-channel demons and a geometrical registration method, then compared hand-engineered features with their learned data-adaptive features, and finally achieved promising registration results. Another work of Cheng et al. (2015) introduced a novel deep similarity learning method that trains a simple binary classifier to learn the local correspondence between 2D MRI and CT image patches of the head. After training, the networks are fine-tuned using two prediction layers to determine whether two patches are similar or dissimilar. A similar strategy is used by Simonovsky et al. (2016), who also estimated a similarity between patches from differing modalities using deep convolutional neural networks (CNNs). They additionally proposed a way to incorporate this measure directly into first-order optimization frameworks. On the task of intersubject MRI deformable registration, they claim that they outperform MI by a significant margin.

A direct prediction of the transformation parameters using deep learning methods was first introduced by Miao et al. (2016) and Yang et al. (2016). Miao et al. (2016) presented a novel and real-time deep learning regression approach for the task of rigid 3D to 2D X-ray registration to overcome the small capture range as well as slow computation time of current intensity-based methods. Yang et al. (2016) proposed a patch-based deep encoder-decoder network which learns the voxel-wise mapping between image registration parameters and image appearance in the context of LDDMMs. They retain the mathematical properties of LDDMMs, e. g., diffeomorphic transforms, using the momentum parameterization and they finally achieved huge speed-ups compared to a direct optimization method, while maintaining high prediction accuracy on brain MRI images.

A more detailed overview of deep learning based registration is provided by the work of Litjens et al. (2017). They summarize that “in



contrast to classification and segmentation, the research community seems not have yet settled on the best way to integrate deep learning techniques in registration methods. Not many papers have yet appeared on the subject and existing ones each have a distinctly different approach. Thus, giving recommendations on what method is most promising seems inappropriate. However, we expect to see many more contributions of deep learning to medical image registration in the near future.”

A reason why there are only a few works so far could be the diversity of registration problems and applications in the medical field combined with the huge number of degrees of freedom in 3D deformable registration as well as the (in most cases) low number of training data sets or corresponding ground truth data. In the domain of deformable deformations of 3D medical data, it would be a very time-consuming task to create exact deformations as an approximate ground truth for a sufficient number of data sets.

## 2.4 VALIDATION

Validation is an important part for almost all medical deformable registration tasks. Often, an expert radiologist or radiation therapist has to manually identify a lot of anatomical landmarks or structures within or on the boundary of the liver and tumor to compute a suitable and significant evaluation measure. Even then, it cannot be guaranteed that the quality of the deformable registration is precisely measured over the whole liver volume. As can be seen in Table 2.1 and Table 2.2, most of the related works used one or more of the following criteria to measure the quality of their proposed methods:

### 1. Distances between landmarks:

- Vessel bifurcations or intersections (Böttger et al., 2003; Brock et al., 2006; Carrillo et al., 2000; Fernandez-de-Manuel et al., 2014; Kadoury et al., 2012; Kaus et al., 2007; Liu et al., 2013; Luu et al., 2016; Rohlfing et al., 2004; Voroney et al., 2006)
- Vessel centerlines (Lange et al., 2005)
- Centroids of small tumors (Böttger et al., 2003; Fernandez-de-Manuel et al., 2014)
- Automatically selected points (Lee et al., 2005)
- Closest surface points, i. e., by either computing
  - Euclidean distances (Carrillo et al., 2000; Fernandez-de-Manuel et al., 2014; Foruzan and Motlagh, 2015; Luu et al., 2016; Rohlfing et al., 2004) or
  - Hausdorff distances (Archip et al., 2007; Elhawary et al., 2010; Foruzan and Motlagh, 2015; Tokuda et al., 2015)

## 2. Volume overlap:

- DSCs between liver and/or tumor volumes (Elhawary et al., 2010; Foruzan and Motlagh, 2015; Luu et al., 2016; Tokuda et al., 2015)

To ensure that this work will be comparable with the related work, equal and similar quality measures will be used and defined later.

### 2.5 REMAINING ISSUES IN LIVER REGISTRATION OF MRI DATA

In conclusion, there are still open questions in the domain of liver registration in MRI, which are so far not covered by the state-of-the-art. At first, the related work will be evaluated in order to derive remaining issues and open research questions. Then, the requirements and objectives of this thesis will be defined for each task and the selected strategies to meet these will be discussed.

**LIVER REGISTRATION OF PRE-PLANNING MRI** In pure MRI liver registration, previous works are most of all either limited to rigid registration (Carrillo et al., 2000; Lee et al., 2005) or limited to deformable registration of high quality diagnostic pre-planning images as in Brock et al. (2006), Fernandez-de-Manuel et al. (2014), Lange et al. (2005), Rohlfing et al. (2004), and Voroney et al. (2006). Many of them would probably fail using real interventional images because of the low image quality resulting from the open MRI device (as illustrated in Figure 1.7). In addition there do not exist any time constraints in this context, which allows the focus to be more on a better registration quality. According to clinical experts in the field of HDR BT, TREs smaller than 3 mm are very good, 3 - 5 mm are sufficient and larger than >5 mm insufficient for any kind of computer-assisted support. On average, the referenced works achieved TREs of about 4.3 mm between liver surface points and selected anatomical landmark, which would be sufficient for interventions. But the computation times are often unknown and thus an evaluation with regard to its suitability for interventional MRI liver data is difficult.

As can be seen in Table 2.1, a main flaw of many of the referenced works is the low number ( $\leq 5$ ) of real patient data sets used for the evaluation. Only the study published by Voroney et al. (2006) measured the quality of their approach on a sufficient number of 17 data sets. As already mentioned in the last chapter, the creation of reference structures, which can be used as a gold standard for the evaluation, is a time-consuming and difficult task. Nevertheless, the question arises if quality indications, that have only been determined on a few data sets, have a real significance or benefit for the medical image analysis research community.

**LIVER REGISTRATION OF INTERVENTIONAL MRI** There exist a few approaches which register pre-planning liver images with interventional liver images deformably (see Table 2.2) and there is no comparable work that registered MRI and interventional MRI so far. Hence a direct quality comparison with such approaches is rather difficult. Tang and Wang (2010), Liu et al. (2013), and Foruzan and Motlagh (2015) registered pre-planning CT data with interventional MRI data and these works are still the most comparable as they faced similar challenges in terms of the quality of interventional MRI data.

An evaluation of their approaches shows that some of them have clear deficiencies in terms of accuracy and quality or computation time attained. Tang and Wang (2010) did not quantify any results except for some selected tumors (with a size  $>10$  mm) and achieved a tumor DSC of 0.87. But their study lacks in terms of a decent evaluation on a sufficient number of data sets or additional validation criteria. Moreover, their combination of a semi-automatic pre-segmentation step in both images and an affine and FFD-based deformable registration leads to high computation times which would be inappropriate for a clinical application.

Foruzan and Motlagh (2015) tackled the problem of bias artifacts arising with interventional MRI data by using MIP projections and a PCA as a basis for their landmark-based deformable registration. They performed a decent evaluation on 18 patients and achieved a DSC of 0.78 for the liver and 0.27 for the tumor and TREs of  $12.0 \pm 4.9$  mm for the liver and  $10.1 \pm 8.7$  mm for the tumor, which is too imprecise for computer-assisted interventions. The runtime of their proposed TPS-based robust point matching method was about 9 min, which would be quite high in a real interventional setting. In addition, it is unclear if they included the timings of surface point and landmark point extraction which is required for their algorithm to work properly.

The approach of Liu et al. (2013) concluded with “unsatisfactory results” with respect to the liver, because of varying liver deformations of tissue near the surface and internal liver tissue. Their presented results showed TREs of  $4.3 \pm 1.9$  mm between selected landmarks but they did not provide computation times to compare with.

**SELECTED REGISTRATION METHODS** Deep learning based approaches were not considered for a deformable registration as there would not be enough ground truth available to create a sufficient amount of training data.

Many of the geometry-based registration methods are unsuitable because they need a preceding extraction of features, e. g. surfaces, in both images. An automatic liver surface extraction cannot be performed so easily automatically on interventional MRI because of the bad image quality. Hence a semi-automatic or manual segmentation

would be required which would take too much time within a clinical setting. Peterlík et al. (2018) achieved a sufficient accuracy for CT liver data but their surface-matching algorithm also requires a segmentation of the liver in the interventional data set.

The sliding-motion based approach of Papież et al. (2014) seemed to be promising since it does not require target organ segmentation in both images and it can handle smooth deformations between and within organs. However they indicate a substantial amount of computational time due to their convolution based filtering methodology applied to filter deformation fields at each iteration. Their proposed NGF-based demons procedure using an isotropic bilateral filtering took around 75 min for 4D lung data sets, which would be unsuitable for a clinical application.

A suitable approach was the one presented by Glocker et al. (2008) and later Mahapatra and Sun (2012). The idea of using a MRF-based objective function combined with a fast multi-scale graph-cut approach seems also promising for the tasks of this thesis.

Regarding V2S liver registration in MRI, there are currently no related and comparable works available.

## THESIS OBJECTIVES

---

The overall aim of this thesis is to provide suitable **V2V** and **V2S** registration approaches which are able to address some of the flaws in the clinical workflow already discussed in Section 1.2 to support the radiologists during current **HDR BT** interventions of the liver. To achieve this aim, more specific objectives have to be defined for both tasks.

### 1. V2V registration:

In cooperation with the a clinical partner, the following objectives shall be met on average in the context of **V2V** liver registration:

- **DSC** > 92 % for the liver surfaces
- **TRE** < 5 mm for the tumor centroids and anatomical landmarks
- Computation time ( $t_c$ ) < 2 min on current consumer hardware

As none of the related work has already met all of these objectives, new strategies must be developed. However, the focus of this thesis is not to invent a new registration algorithm or type of deformation but to adequately adapt and combine existing approaches so that the defined objectives will be achieved.

Therefore, freely available state-of-the-art deformable registration methods will be considered as part of a preliminary study on a subset of the given data. This means in particular, an analysis of the methods which are accessible via **ITK** (Yoo et al., 2002) and other libraries and toolboxes like the Flexible Algorithms for Image Registration (**FAIR**) toolbox (Modersitzki, 2009). The preliminary studies are primarily intended to figure out aspects which have still potential for improvement.

As a next step, already examined deformable registration approaches will be adapted to obtain greater robustness to noise and intensity inhomogeneities, which is present in most of the interventional **MRI** planning images. In particular, it will be investigated how to supplement necessary redundant information with model information, in case solely used image information is not enough for a stable registration, e. g., as in some of the interventional planning images. During the whole process, it will be mainly focused on fast computation times for the complete registration procedure to meet the objectives. This will be one of the main challenges, since most of the existing deformable methods, e. g., B-spline and **FEM**-based approaches, are computationally intensive or require a kind of manual interaction beforehand, e. g.,

as many geometry-based methods. To achieve this objective, it will be concentrated, among other things, on multi-threaded implementations of optimizers and deformable transformations.

## 2. V2S registration:

Regarding V2S liver registration we defined the following objectives:

- DSC > 92 % for the liver surfaces
- TRE < 5 mm for the tumor centroids and anatomical landmarks
- Computation time ( $t_c$ ) < 1 s on current consumer hardware

Hence there does not exist related work that registered on 2D interventional MRI, a new strategy must be developed to adequately meet the defined objectives. In a first step, it will be investigated which freely available state-of-the-art deformable registration methods (from ITK and FAIR) are able to perform a V2S registration task. Depending on the results of this study, new V2S registration approaches will be developed and proposed.

In the end, a prototypical registration system for interstitial HDR BT is intended. The prototype should contain V2V and V2S registration methods to finally enable a stable and accurate transfer of clinical 3D pre-planning information (eTHRIVE sequences), i. e., liver and tumor segmentations as well as virtually planned applicator trajectories, onto the 2D interventional image slices (T1-FFE slices) during needle insertion. Since no externally acquired respiratory information is available, an adequate strategy must be developed that is able to accurately register both images at certain times in real time. This strategy will be discussed later in Section 6.

The final liver registration framework including the main steps of this thesis are outlined in Figure 3.1.

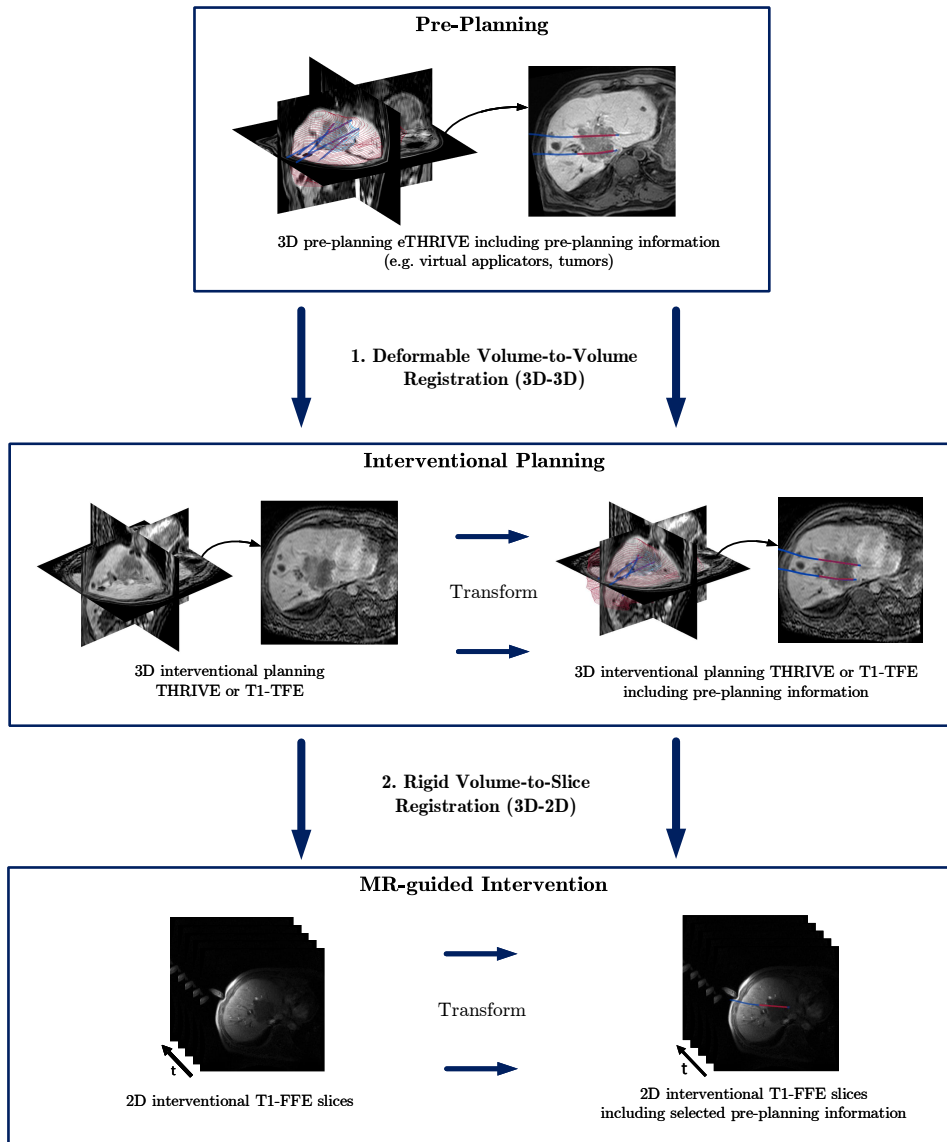


Figure 3.1: Illustration of the proposed liver registration framework: (1) First, a deformable volume-to-volume (V2V) registration transforms pre-planning information to the 3D interventional MRI planning images. (2) Second, a rigid volume-to-slice (V2S) registration transforms 3D interventional MRI planning information to 2D interventional slices which are acquired in real time (1/s). Finally, the transformed pre-planning information can be used as guidance for the interventional radiologist to improve the accuracy and time spent during the tumor puncture.





## MATERIAL

---

In order to evaluate the suitability of the results for a clinical application, a sufficiently high number of data sets and ground truth is required. In cooperation with the Department of Radiology and Nuclear Medicine of the University Hospital in Magdeburg, data from 64 patients, who have undergone a MRI-based HDR BT from 2014 to 2016, was retrospectively acquired. For each patient, a number of pre-planning eTHRIVE, interventional planning THRIVE or T1-TFE images, and interventional T1-FFE slice images are available.

The available data is differentiated into two subsets. On the one hand, various preliminary studies were performed on the basis of a small subset of eleven patients. On the other hand, a complete study with another 53 patients was performed later. These data sets are termed Data<sub>0</sub> and Data<sub>1</sub> respectively. For both data sets, the approval of the responsible ethics committee of the Otto von Guericke University at the Medical Faculty and at the University Hospital Magdeburg has already been obtained. Based on the registration task (V2V or V2S), both data sets were further subdivided in Data-V2V<sub>0</sub> and Data-V2V<sub>1</sub> as well as Data-V2S<sub>0</sub> and Data-V2S<sub>1</sub>, respectively.

In addition, clinical experts have defined evaluation criteria, which are used as approximate ground truth or gold standard, respectively, including segmentations of the liver and tumor boundaries as well as definitions of anatomical landmarks within the liver. In the following sections, the data and gold standard is described for each part of my thesis.

### 4.1 VOLUME-TO-VOLUME REGISTRATION

#### DATA-V2V<sub>0</sub>:

- 3D pre-planning images:
  - MRI scanner: Philips Intera 1.5 T
  - MRI sequence: eTHRIVE; repetition time (TR): 4.0 - 4.1 ms; echo time (TE): 2.0 ms
  - Voxel spacing: 0.98×0.98×3 mm
  - FOV: 315×315×240 mm
  - Number of images: 11
- 3D interventional planning images:
  - MRI scanner: Philips 1.0 T Panorama HFO

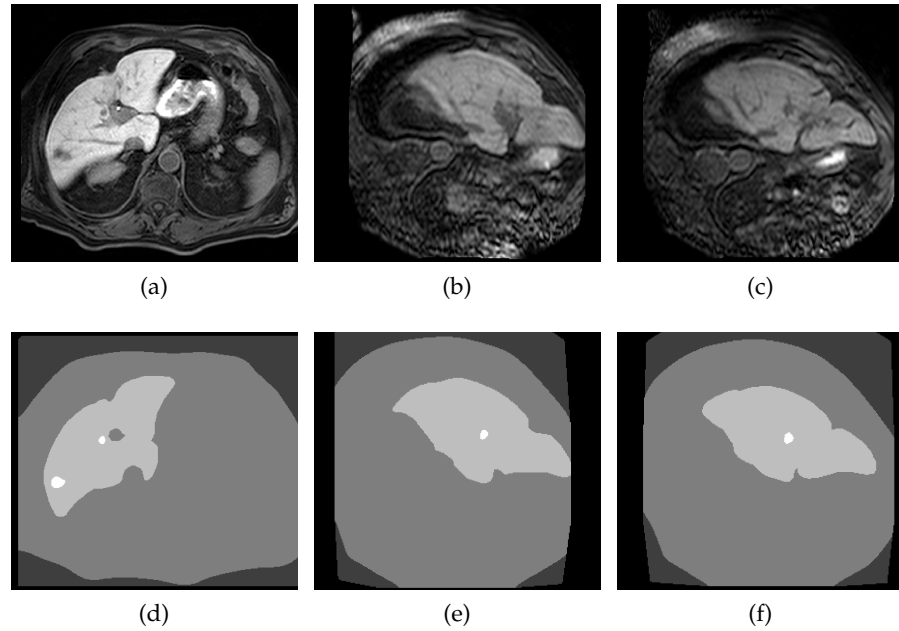


Figure 4.1: Illustration of the images and gold standard segmentation masks of [Data-V2V<sub>0</sub>](#). The first row shows exemplary slices of 3D (a) pre-planning, (b) first interventional, and (c) last interventional images. The second row (d-f) shows the corresponding gold standard including segmentations of the liver and tumors, displayed with different labels.

- MRI sequence: [THRIVE](#); TR: 3.8 - 4.6 ms; TE: 1.8 - 2.3 ms
- Voxel spacing: 1.19×1.19×2.5 mm
- FOV: 285×285×210 mm
- Number of images: 22

- Gold standard data for both images:
  - Segmentation masks of the liver
  - Segmentation masks of several tumors

For each patient, gold standard annotation are available for the pre-planning as well as the first and the last interventional image. Gold standard annotations were created by an interventional radiologist with more than five years of experience. The gold standard of [Data-V2V<sub>0</sub>](#) comprises segmentations of the liver and tumors for each of the data sets (see Figure 4.1). This enables an evaluation of the quality of the [V2V](#) registration on the liver surfaces and within the tumor regions.

#### [DATA-V2V<sub>1</sub>](#):

- 3D pre-planning images:
  - See [Data-V2V<sub>0</sub>](#) above

- Number of images: 53
- 3D interventional planning images:
  - MRI scanner: Philips 1.0 T Panorama HFO
  - MRI sequence: T1-TFE; TR: 11.2 ms; TE: 5.5 ms
  - Voxel spacing:  $1.27 \times 1.27 \times 2.5$  mm
  - FOV:  $285 \times 285 \times 210$  mm
  - Number of images: 78
- Gold standard data for both images:
  - Segmentation masks of the liver
  - Segmentation masks of several tumors
  - Anatomical landmarks at corresponding vessel bifurcations

In contrast to the preliminary data set [Data-V2V<sub>0</sub>](#), [Data-V2V<sub>1</sub>](#) comprises images of 53 patients and includes T1-TFE instead of THRIVE interventional planning images. The MRI sequence of the V2V registration data was changed because T1-TFE images are more similar to the T1-FFE images in terms of image properties and thus more suitable for the subsequent V2S registration. Moreover it can be evaluated whether the proposed V2V registration is working for both sequences. Figure 4.2 shows similarities and differences between the two planning sequences.

For each patient, gold standard annotations for the pre-planning as well as the first and the last interventional image are available, which comprises segmentations of the liver and tumors. In addition to [Data-V2V<sub>0</sub>](#), an clinical expert and two field experts have selected anatomical landmarks on vessel bifurcations within the liver. This enables an evaluation of the quality of the V2V registration also within the liver tissue. Hence the experts set their anatomical landmarks independently on the same vessel bifurcations, the impact of the inter-observer variability on the landmark quality measure can be measured, too.

## 4.2 VOLUME-TO-SLICE REGISTRATION

### DATA-V2S<sub>0</sub>:

- 3D interventional planning images:
  - MRI sequence: THRIVE
  - Unchanged imaging parameters
  - Number of images: 22
- 2D interventional image slices:
  - MRI scanner: Philips 1.0 T Panorama HFO

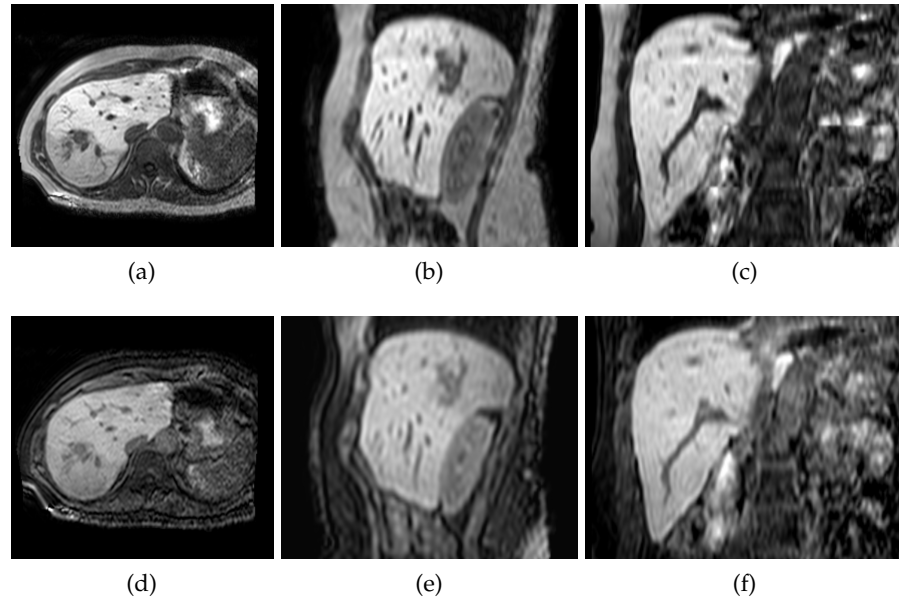


Figure 4.2: Comparison of **T1-TFE** (a-c) and **THRIVE** (d-f) interventional planning images. The former are used within **Data-V2V<sub>0</sub>** and the latter within **Data-V2V<sub>1</sub>**. Anatomical views from left to right are: axial, sagittal, coronal.

- **MRI** sequence: **T1-FFE**; **TR** = 10.4 ms; **TE** = 6.0 ms
- Voxel spacing:  $1.1 \times 1.1 \times 8$  mm
- **FOV**:  $352 \times 352 \times 8$  mm
- Number of images: 552
- Gold standard data for both images:
  - Segmentation masks of the liver

Finally, **Data-V2S<sub>0</sub>** comprises 23 interventional 3D planning images which are registered with a total number of 552 interventional 2D image slices. Each of the 2D image slices was taken at a different time. Segmentation masks of the liver were given as gold standard data for the evaluation.

#### **DATA-V2S<sub>1</sub>**:

- 3D multiplanar reconstructed subvolumes of interventional planning images:
  - **MRI** sequence: **T1-TFE**
  - Unchanged imaging parameters
  - Number of images: 887
- 2D interventional image slices:
  - **MRI** sequence: **T1-FFE**

- Unchanged imaging parameters
- Number of images: 9738
- Gold standard data for both images:
  - Segmentation masks of the liver
  - Segmentation masks of the tumors
  - Anatomical landmarks at corresponding vessel bifurcations

In contrast to [Data-V2S<sub>0</sub>](#), multiplanar reconstructed subvolumes of the 3D [T1-TFE](#) images have been created at each slice orientation in the 2D [T1-FFE](#) images, which means at any time when the radiologist or the medical technical assistant has changed the current slice orientation. This process is described in more detail in [Chapter 6](#). In addition to [Data-V2S<sub>0</sub>](#), segmentation masks of the tumors and selected anatomical landmarks are available as gold standard.

### 4.3 EVALUATION MEASURES

To evaluate the proposed approaches, first, the resulting transformations have to be applied to the gold standard data (segmentation masks, anatomical landmarks) of the template images. This enables a comparison of the results with the gold standard data of the reference images to estimate different kinds of [TRE](#) and [DSC](#).

- The [DSC](#) as a measure of the segmentation volume overlap between both liver segmentation masks is computed by:

$$\text{DSC} = \frac{2|V_T \cap V_R|}{|V_T \cup V_R|}, \quad (4.1)$$

where  $V_T$  and  $V_R$  are segmentation mask volumes of the template and reference image, respectively.

- The average Euclidean distance ([ED](#)) for  $N$  corresponding points (tumor centroids, anatomical landmarks)  $\mathbf{p}_i$  and  $\mathbf{q}_i$  in the template and reference image is computed by:

$$\bar{d} = \frac{\sum_{i=1}^N d(\mathbf{p}_i, \mathbf{q}_i)}{N} \quad (4.2)$$

with

$$d(\mathbf{p}, \mathbf{q}) = \sqrt{\sum_{j=1}^3 (q_j - p_j)^2} \quad (4.3)$$

where  $q_j$  and  $p_j$  are the components of the 3D vectors  $\mathbf{p}$  and  $\mathbf{q}$ .

- In addition, average **ED** as the averaged contour misalignment between surface points of the liver are computed by:

$$\overline{\text{ED}} = \frac{\text{ED}_{\text{TR}} + \text{ED}_{\text{RT}}}{2} \quad (4.4)$$

with

$$\text{ED}_{\text{TR}} = \frac{\sum_i \min_j (d(\mathbf{p}_R^j, \mathbf{p}_T^i))}{|k_T|}$$

$$\text{ED}_{\text{RT}} = \frac{\sum_i \min_j (d(\mathbf{p}_T^j, \mathbf{p}_R^i))}{|k_R|}$$

where  $k_R$  and  $k_T$  are sets of surface points,  $\mathbf{p}_R^i \in k_R$  and  $\mathbf{p}_T^j \in k_T$  are the  $i$ -th and  $j$ -th 3D surface point of each set from the segmentation masks of the template and of the reference image  $M_R$  and  $M_T$ , respectively.

- The average Hausdorff distance (**HD**) (Chalana and Kim, 1997) as the worst-case contour misalignment between surface points of the liver is computed by:

$$\overline{\text{HD}} = \max\{\text{HD}_{\text{TR}}, \text{HD}_{\text{RT}}\} \quad (4.5)$$

with

$$\text{HD}_{\text{TR}} = \max_i \left\{ \min_j \left\{ d(\mathbf{p}_T^j, \mathbf{p}_R^i) \right\} \right\}$$

$$\text{HD}_{\text{RT}} = \max_j \left\{ \min_i \left\{ d(\mathbf{p}_R^i, \mathbf{p}_T^j) \right\} \right\}$$

Since there is no perfect ground truth to compare with, an approximate ground truth was generated manually by an expert radiologist as a gold standard. However, such a manual generation is not always completely error-free. For example, small changes in the contouring already lead to different volume ratios of the liver segmentation masks. When setting landmarks on vessel bifurcations in two slightly different 3D images of the liver, there does not always exist a clear correspondence. Therefore, an inter-observer variability regarding the landmarks for a subset of 10 data sets was calculated, which can be used to better interpret the calculated error rates. An additional rigid and volume preserving deformable registration of the gold standard liver and tumor segmentation masks was performed in order to compare with.

In this chapter, standard [V2V](#) registration methods are first investigated and afterwards, the developed [V2V](#) registration approaches are discussed in detail. Parts of this chapter have already been published in König et al. (2017) and Rak et al. (2017) and may therefore partially contain similar or identical formulations and illustrations. The publishers granted a non-exclusive, world-wide licence to reproduce the material for the purpose of this thesis<sup>1</sup>. I separated the chapters *methods*, *results*, and *discussion* according to each study, because the discussion of the results of the preliminary studies influenced the choice of methodology in the subsequent studies.

## 5.1 PRELIMINARY STUDY A

In this preliminary work, a comprehensive investigation of rigid and deformable intensity-based registration methods, that are freely available in [ITK](#), was performed. The main objective was to find out if standard state-of-the-art registration methods are feasible for the tasks presented and if not, to figure out at which points is still need for further research. [ITK](#) offers a multitude of different types of transformations, measures, and optimizers which are to be investigated in the remainder of this section.

### 5.1.1 *Material and Methods*

All available combinations were applied on the preliminary data set [Data-V2V<sub>0</sub>](#), which includes 3D pre-planning [eTHRIVE](#) and 3D interventional [THRIVE](#) images of eleven patients. To simplify processing, all images were downsampled to yield isotropic voxels of 2.5 mm extent. All experiments were carried out on consumer hardware comprising an AMD FX™-6300 @ 3.5 GHz and 8 GB RAM.

First, both images were initialized according to their geometrical center. Second, rigid registration was applied to cope with the differences in patient positioning between the images. Given a reference image  $I_R$ , image registration tries to find the optimal transformation of the spatially aligned and resampled template image  $I_T$  with regard to the similarity between both images, the quality of which can be as-

---

<sup>1</sup> Reprinted by permission from Springer Nature Customer Service Centre GmbH: Springer Nature, International Journal of Computer Assisted Radiology and Surgery, Joint deformable liver registration and bias field correction for MR-guided HDR brachytherapy, M. Rak, T. König, K. D. Tönnies et al, (2017)

essed by a measure  $S(I_R, I_T)$ . The measure is calculated over all voxel  $s \in P$  where  $P$  is the set of voxels shared by images  $I_T$  and  $I_R$  after transformation, i. e. the intersection of the transformed pre-planning and the interventional image. Hence template and reference images are both **MRI**-based, monomodal similarity measures, which can be applied in combination with appropriate preprocessing. Potential preprocessing methods are evaluated in the context of this thesis too. **ITK** offers the possibility to compute various intensity-based similarity measures, the most promising of which are listed below::

$$S_{SSD} = \frac{1}{|P|} \sum_{s \in P} \|I_R(s) - I_T(s)\|^2 \quad (5.1)$$

$$S_{MAD} = \frac{1}{|P|} \sum_{s \in P} |I_R(s) - I_T(s)| \quad (5.2)$$

$$S_{NCC} = \frac{1}{|P|} \sum_{s \in P} \frac{(I_R(s) - \mu_R)(I_T(s) - \mu_T)}{\sigma_R \sigma_T} \quad (5.3)$$

where  $S_{SSD}$ ,  $S_{MAD}$ ,  $S_{NCC}$  are the similarities defined by **SSD**, **MAD**, and **NCC**, respectively.  $\mu_R$  and  $\mu_T$  are expected intensities and  $\sigma_R$  and  $\sigma_T$  are standard intensity deviations of the reference and transformed template images  $I_R$  and  $I_T(T)$ , respectively.

**MI**-based similarity measures are defines as:

$$S_{MI} = H(I_R) + H(I_T) - H(I_R, I_T) \quad (5.4)$$

$$S_{NMI} = \frac{H(I_R) + H(I_T)}{H(I_R, I_T)} \quad (5.5)$$

with

$$H(I_R) = - \sum_{s_i \in I_R} p(s_i) \log p(s_i)$$

$$H(I_T) = - \sum_{s_j \in I_T} p(s_j) \log p(s_j)$$

$$H(I_R, I_T) = - \sum_{s_i \in I_R} \sum_{s_j \in I_T} p(s_i, s_j) \log p(s_i, s_j)$$

where  $S_{MI}$  and  $S_{NMI}$  are the similarities defined by **MI** and **NMI**, respectively.  $H(I_R, I_T)$  is the joint Shannon entropy and  $p(s_i, s_j)$  is the joint probability of the pixel pair intensities  $s_i$  and  $s_j$  of the reference and transformed template images  $I_R$  and  $I_T$ .

For the sake of completeness, a discrete version of the **NGF**-based similarity as described by Tramnitzke et al. (2014) is already defined at this point because it will be used in a subsequent study:



$$S_{\text{NGF}} = \frac{1}{2} \sum_{s \in \mathcal{P}} \left( 1 - \left( \frac{\langle \nabla I_T(s), \nabla I_R(s) \rangle}{\|\nabla I_T(s)\|_{\eta} \|\nabla I_R(s)\|_{\eta}} \right)^2 \right) \quad (5.6)$$

where  $\nabla I$  is the gradient field of an image  $I_*$ ,  $\langle \cdot, \cdot \rangle$  computes the inner product of two vectors and  $\|\cdot\|_{\eta} = \langle \cdot, \cdot \rangle + \eta^2$ . The parameter  $\eta^2$  allows to compensate for noise and should be chosen such that it reflects the noise characteristics of the given modalities.

With the exception of **NGF**, all similarity measures were tested in this study. Artifacts caused by implanted applicators were negligible for the rigid registration, because they affected only small portions of the interventional data. Bias field artifacts were only imposed on parts of the interventional data and thus did not impede rigid registration either. More problematic was the extensively varying signal-to-noise ratio (**SNR**) in the interventional planning images already discussed in Section 1.2.1 (Figure 1.7), possibly causing errors if the registration process is not initialized close to the anticipated transformation. To cope with this issue, a pyramidal multi-resolution registration scheme, as illustrated in Figure 5.1, was employed. Starting with the initial registration on a rather coarse image resolution, the transformation was subsequently refined on smoothed images of increasing resolution until full resolution was reached. Finally, downsampling factors of  $1/6$ ,  $1/4$ , and  $1/2$  were used. This multi-resolution scheme proved to be stable with respect to varying noise levels, because noise cancels out on coarser resolutions, providing good initializations for registration refinement at higher resolutions.

Next, an affine and deformable registration was applied subsequently on the best results after rigid registration to cope with local liver deformations. However, deformable registration methods were only applied to a single, coarser resolution. This decision is based on preliminary experiments, which have shown that an application on the full resolution is too computationally expensive and thus not appropriate within a clinical setting. However, it was attempted to find out which types of transformation and similarity measure could be promising for further investigation or adaption. As a drawback of the downsampling, the obtained results must be interpreted with caution since evaluation was performed on the transformed, downsampled segmentation masks and thus, small structures, such as tumors or vessels, may almost vanish on coarser resolutions. Initial downsampling factors of ( $1/6$ ,  $1/4$ ,  $1/2$ ) were investigated in this regard to find the best trade-off between registration quality and computation time. Downsampling produced images with voxel spacings varying between  $15 \times 15 \times 15$  mm ( $1/6$ ) and  $5 \times 5 \times 5$  mm ( $1/2$ ) for the pre-planning **eTHRIVE** and interventional **THRIVE** images. Overall, about 300 different registration combinations were examined for rigid, affine, and deformable **V2V** registration.

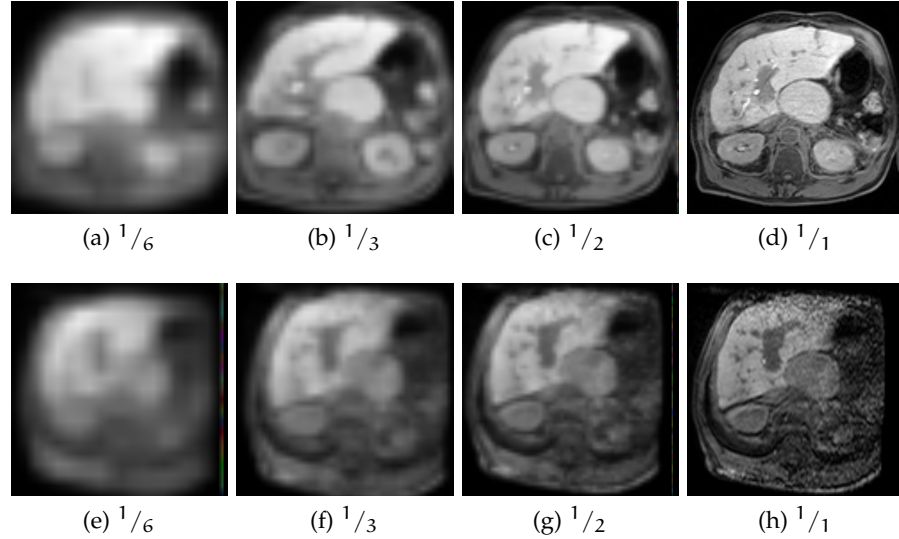


Figure 5.1: Multi-resolution image pyramid from coarse (left) to fine (right) for a pre-planning [eTHRIVE](#) image (a-d) and interventional [THRIVE](#) planning image (e-h). Gaussian smoothing with appropriate standard deviations was performed before the resampling on each level.

### 5.1.2 Results and Discussion

Rigid registration worked best using a 3D Euler transformation in combination with several similarity measures, e. g., [NCC](#), [NMI](#) or [MMI](#), and a gradient descent optimizer achieving a [DSC](#) of 0.9 for liver and 0.28 for tumor surfaces (see [Table 5.1](#)). In contrast, most of the standard deformable registration methods were computationally expensive and thus inappropriate for time-critical clinical applications. For [FFDs](#) with B-splines, [LBFGS](#) optimizers worked best using an initial downsampling factor of  $1/4$  and a mesh grid size of  $3 \times 3 \times 3$  voxel in combination with an Advanced Normalization Tools ([ANTs](#)) similarity measure ([Avants et al., 2011](#)). [ANTs](#) computes [NCCs](#) using a spatial neighborhood around each voxel. However, the average run-times ranged from 56 s to more than 120 s for downsampling factors of  $1/4$  and  $1/3$ , respectively. Overall, the fastest deformable registration approaches involved a voxel displacement field based transformation (termed as [DispField](#)) which additionally performs a Gaussian smoothing of the displacement field after each optimization step. [DispField](#) performed best in combination with [ANTs](#) and gradient descent optimizer. Computation times for [DispField](#) based transformations ranged from of 26 s to 144 s for a downsampling of  $1/3$  and  $1/2$ , respectively (see [Table 5.1](#)).

With regard to rigid registration, the best-performing combination compared well to the upper bounds of the maximum achievable quality and also finished computation within a reasonable time. It can

Table 5.1: Results of V2V registration on a single resolution level with standard methods from ITK for the preliminary Data-V2V<sub>0</sub>. Values in [ ] indicate the upper bounds on the result quality given optimal rigid (Rig. Mask) and volume-preserving deformable (Def. Mask) registration of the gold standard segmentation masks. Abbrev.: DSC - Dice coefficient;  $\overline{ED}$  - Euclidean distance.

V2V	Average t <sub>c</sub> [s]	Liver		Tumor(s)
		DSC [%]	$\overline{ED}$ [mm]	DSC [%]
Initial	-	44 ± 21	20.9 ± 8.6	1 ± 5
Rigid	4.4	90 ± 3	3.3 ± 0.8	28 ± 18
Affine	10.6	91 ± 3	3.0 ± 0.9	36 ± 22
Rig. Mask	-	[90 ± 2]	-	[41 ± 23]
B-spline (1/4)	56.3	92 ± 2	-	
B-spline (1/3)	> 120	93 ± 5	-	
DispField (1/3)	26.4	94 ± 1	1.9 ± 0.4	55 ± 12
DispField (1/2)	144.3	95 ± 1	1.6 ± 0.4	61 ± 13
Def. Mask	-	[97 ± 3]	-	[81 ± 14]

also be observed that an additional affine transformation after the initial rigid registration did not improve the registration quality but increased runtimes due to the additional degrees of freedom during optimization. The rather low tumor DSCs and high liver DSCs need to be interpreted with caution because of the coarse resolution level and relatively small number of patients. Thus, small misalignments together with likewise small gold standard imperfections may result in large differences in the DSC solely because of the small tumor sizes in the Data-V2V<sub>0</sub> ( $1.71 \pm 1.61$  mL on average). Furthermore, an upper bound DSC of  $0.81 \pm 0.14$  of the volume-preserving deformable registration of the tumor segmentation masks indicated, that a manual segmentation of small tumors in different MRI sequences is a challenging task, even for an expert radiologist.

Regarding deformable registration methods, the best performing combination comprised a DispField transformation, ANTs (Avants et al., 2011) and the gradient descent optimizer. ANTs performed better than most of the other available similarity measures in ITK because it computes similarity values in a spatial neighborhood, which compensates for some of the intensity inhomogeneities in the interventional images. The DispField transformation is able to perform a voxel-wise, dense transformation that enables appropriate transformations on coarser resolution levels, but leads to high computation expenses at finer resolution levels. Although first results are promising, there

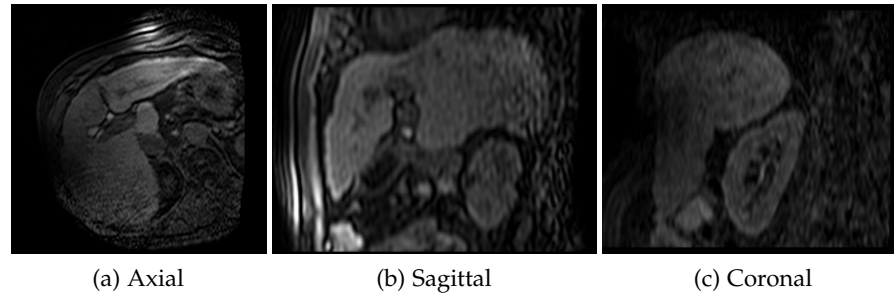


Figure 5.2: Challenging data set including strong bias field and noise. In such cases standard deformable procedures failed.

is still room for improvement in deformable registration. Even the best investigated combination in deformable [V2V](#) registration still has limitations in cases with bias field artifacts (see [Figure 5.2](#)). Hence, deformable [V2V](#) registration methods should be incorporated into a multi-resolution approach, which however must still fulfill the time constraints defined in [Chapter 3](#) by using a reasonable kind of regularization. This could be done by using more of the previously available information such as segmentation masks of the liver of the available pre-planning [eTHRIVE](#) data, which have to be created in the course of a proper pre-planning phase anyway. In addition, one should consider a more comprehensive pre-processing of the data, e. g., by cropping the [FOV](#).

In summary, the following findings were made and should be considered in the subsequent studies:

- Rigid registration already works sufficiently precise and fast to compensate for different patient positioning.
- Deformable registration still needs improvements in terms of accuracy and computation time.
- Deformable registration should be integrated into a multi-resolution scheme that compensates for bias field artifacts and locally varying noise.
- Segmentation masks of the pre-planning data should be used to improve registration accuracy.

## 5.2 PRELIMINARY STUDY B

In this study, selected registration methods from the literature were adapted and improved to cope with the named issues. Next, a novel approach is proposed that performs a deformable [V2V](#) registration of 3D pre-planning and 3D interventional planning [MRI](#) images in a sufficiently accurate and fast manner to be applicable for interventional settings.

### 5.2.1 Material and Methods

In order to show the suitability of the method presented next, [Data-V2V<sub>0</sub>](#) was used, which includes one 3D pre-planning [eTHRIVE](#) image and two 3D interventional [THRIVE](#) images for each of the eleven patients. The interventional images were termed as  $R_1$  for images without applicators and  $R_2$  for images including several applicators. In a subsequent study (Section 5.3), a more detailed evaluation was performed on the complete data set [Data-V2V<sub>1</sub>](#). Again, all images were downsampled to an isotropic voxel spacing of 2.5 mm. All experiments were carried out on consumer hardware comprising an Intel® Core™ i7-3720QM @ 3.4 GHz and 12 GB RAM.

#### 5.2.1.1 Rigid Registration

Rigid registration was first applied to model the differences in patient positioning in the pre-planning and interventional images. The results of the preliminary study have shown that the choice of the similarity measure has little influence on the quality of the results. Thus, the focus was on the deformable registration part in this study. A normalized version of the [MAD](#) as described in Equation 5.2 was used, which should be more stable in cases where the intensity scaling strongly differs between the images. To find the rigid transformation between the transformed pre-planning image  $I_T$  and the interventional image  $I_R$ , the following similarity measure had to be minimized

$$S_{\text{NMAD}} = \frac{1}{|P|} \sum_{s \in P} \left| \frac{I_T(s)}{\mu_T} - \frac{I_R(s)}{\mu_R} \right|. \quad (5.7)$$

where the expected intensities  $\mu_R$  and  $\mu_T$  need to be evaluated over the set of shared voxels  $P$  to not skew the normalization by different spatial domains. As already figured out, artifacts caused by implanted applicators are negligible for the rigid registration because they affect only a small portion of the interventional data sets and thus had little influence on the used similarity measure (Equation 5.7). As previously shown in Figure 1.7, bias field artifacts are only focused on parts of the interventional data and thus pose no problem to rigid registration, but to deformable registration. Standard pre-processing methods for bias field correction such as N3 (Sled et al., 1998) and its extension N4 (Tustison et al., 2010) struggled to improve tissue homogeneity because these require that the bias field contains low frequency content compared to the actual image signal, which may be violated for the data used (see Figure 5.3(a-b)). Less stringent techniques such as PABIC (Styner et al., 2000) took several minutes to process, which is unacceptable in an interventional setting (see Figure 5.3(c)). To cope with varying [SNR](#) within the interventional images, a similar pyramidal multi-resolution registration scheme as stated in Section 5.1 was used.

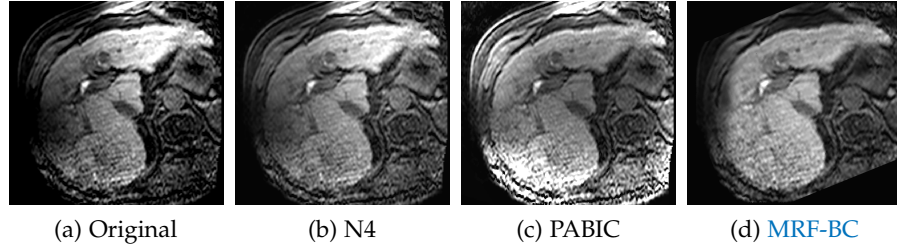


Figure 5.3: Challenging case with extensive, spatially varying noise and strong tissue inhomogeneities in the interventional image. Standard pre-processing methods for bias field correction either struggled to improve tissue homogeneity (N4 (Tustison et al., 2010)) or took several minutes to process (PABIC (Styner et al., 2000)). The presented approach yields good results at marginal computational costs.

After rigid registration, the intensities of both images were rescaled by  $I_T/\mu_T$  and  $I_R/\mu_R$  to ensure a common normalized intensity range. Furthermore, registered images were cropped to an axis-aligned region of interest (ROI), which was extracted automatically based on the transformed pre-planning segmentation masks. ROI extraction was used because large parts of the images are irrelevant for the task of this thesis, i. e. they do not contain pre-planned applicators, tumor tissue, the liver, or nearby organs at risk. The extracted ROIs were then passed into the deformable registration.

#### 5.2.1.2 MRF-based Deformable Registration

To identify the non-rigid changes, the findings of the previous study were first evaluated and then combined with promising methods from the state-of-the-art which were already figured out in Section 2.5. I decided to use a deformable registration method based on MRF theory in this thesis since it seemed promising for the presented registration task in terms of computational efficiency (like demonstrated in Glocker et al. (2008), Glocker (2010), or Mahapatra and Sun (2012)). Discrete optimization methods have some advantages when compared with continuous methods:

1. Most of the continuous methods require the objective function to be differentiable while discrete methods are inherently gradient-free.
2. For discrete methods, prior information can be easily introduced by using the discrete label space to control its range and resolution.
3. With regards to the computational effort, parallel architectures can be used to perform non-sequential tasks required by several

discrete algorithms, which leads to more efficient implementations.

A main advantage for continuous methods compared to discrete methods is the accuracy, which is not limited by the discretization. However, Glocker (2010) already suggested intelligent refinement strategies to achieve an accuracy similar to continuous approaches.

Within the MRF context, deformable registration is seen as a discrete minimization problem, seeking to select the best displacement  $\Delta_s$  for each voxel  $s$  from a pre-specified set of allowed displacements. Let  $\Delta$  be the anticipated displacement field, then the optimization problem can be formulated as

$$E(\Delta) = \lambda \sum_{s \in P} D_s(\Delta_s) + (1 - \lambda) \sum_{(s,t) \in N} V_{s,t}(\Delta_s, \Delta_t), \quad (5.8)$$

where  $P$  is the known set of voxels shared by both images after ROI extraction and set  $N$  contains all pairs of spatially neighboring voxels.  $D_s$  and  $V_{s,t}$  are data and smoothness terms defined over particular voxel displacements, while parameter  $\lambda$  controls the relative importance of both terms. This formulation enables smoothness on the deformation field by means of the introduced graph edges, while the unary term is able to encode the image support for a given deformation.

Given particular implementations of both terms (discussed later), the  $\alpha$ -expansion algorithm of Boykov et al. (2001) was applied to find a near-optimal solution for Equation 5.8, which is guaranteed to stay within a factor of two of the globally optimal solution. In particular, the cache-efficient multi-core implementation of Jamriska et al. (2012) was used, which is available as a part of the GridCut library<sup>2</sup> and seemed to be well suited for a clinical application. The presented deformable registration approach was implemented in C++ and ITK.

Since a direct optimization of Equation 5.8 is costly if potential displacements become large, i. e. several voxels in each direction, the deformable registration was integrated into a pyramidal multi-resolution scheme to solve for large displacements on coarse image resolutions and to add finer displacement field details with increasing image resolution, until full resolution is reached. Such a scheme requires an integration of the displacements known from coarser resolutions into Equation 5.8 at the current resolution. To this end, the displacement field  $\Delta$  was re-defined as the composition of the already known displacement  $\Delta^k$  and the anticipated update field  $\Delta^u$ . Likewise, the displacement  $\Delta_s$  of a voxel  $s$  was calculated as  $\Delta_s^k + \Delta_s^u$ , with  $\Delta_s^u$  being variables of the MRF optimization task.

The scheme is illustrated in Figure 5.4 (left). Starting on the coarsest resolution, Equation 5.8 was optimized and the resulting displacement field was feeded into the next resolution level. For each subsequent

<sup>2</sup> <http://www.gridcut.com/>

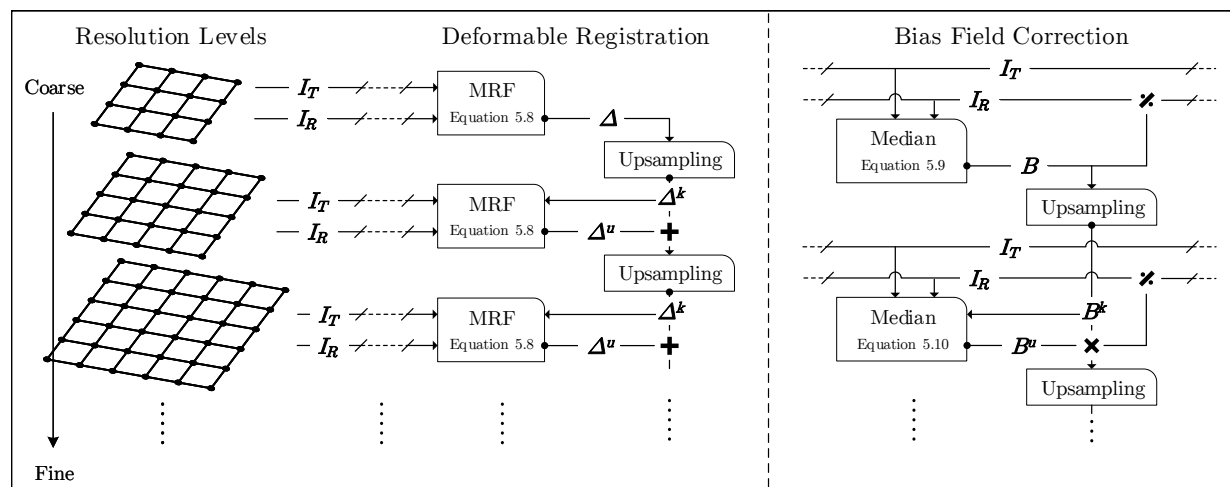


Figure 5.4: Illustration of the pyramidal multi-resolution scheme used within the proposed **MRF-BC** deformable registration. The visualization is separated into the deformable registration part (left) and the bias field correction part (right). The latter takes place right before **MRF** optimization, which is indicated by the dashed horizontal lines. On each resolution level,  $I_T$  and  $I_R$  represent the appropriately smoothed and downsampled pre-planning and interventional image.  $\Delta^k$  and  $\Delta^u$  denote the displacement field known from the previous level and the currently anticipated update field, respectively.  $B^k$  and  $B^u$  denote the bias field known from the previous level and the currently anticipated update field, respectively. On the first level, the displacement and bias field are simply called  $\Delta$  and  $B$ , respectively. Inputs to the particular processing steps (rectangles) are marked by arrows, while outputs are marked by dots. Mathematical operators '+', ' $\times$ ' and ' $\div$ ' combine inputs voxel-wise. 2D grids were only used for illustration purposes.



level, the known displacement field  $\Delta^k$  was upsampled to the current resolution by linear interpolation, solved for the best update field  $\Delta^u$ , and then the composed displacement field  $\Delta^k + \Delta^u$  was incorporated into the next level, if any.

Varying noise levels and applicator-related artifacts did not have a significant impact on coarser resolutions due to smoothing, but they certainly come into effect at higher resolutions, which was addressed by an appropriate data term that is discussed later. Tissue inhomogeneities caused by the varying bias field were more problematic and needed to be addressed explicitly for successful deformable registration. Otherwise, deformable registration would probably fail, as can be seen in Figure 5.5.

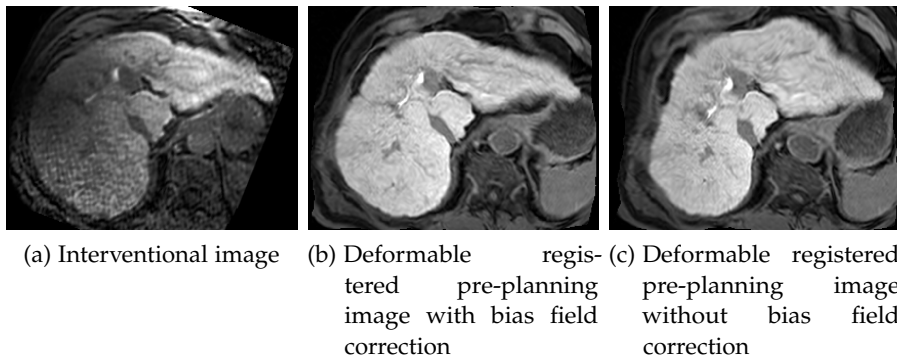


Figure 5.5: Registration results at the example from Figure 5.6, where the bias field was (b) considered and (c) not considered during deformable image registration. False deformations in (c) mostly occur in parts of (a), which contain strong tissue inhomogeneities.

### 5.2.1.3 Bias Field Correction

A bias field in MRI is typically considered as smooth multiplicative function, which scales tissue intensities differently in various parts of the image, as seen in Figure 5.6. Factoring its influence is an ill-posed problem unless restricting assumptions are made or additional information is available. In the given case, additional information can be obtained by the rigid alignment of both images, provided that the rigid registration was successful. Hence, differential bias field correction as proposed in Lewis and Fox (2004) was adopted. They noticed that the voxel-wise intensity quotient of two perfectly aligned, noise-free, images equals the quotient of their bias fields. Therefore, knowing the bias field of either image is sufficient to estimate that of the other image. This is exactly the case here because a constant bias field was assumed for the pre-planning images.

According to Lewis and Fox (2004), even in case of noise and small misalignments from prior registration, the differential bias field  $B$  can still be approximated via

$$B(s) \approx \text{median} \left\{ \frac{I_R(t)}{I_T(t)} \middle| t \in M_s \right\}, \quad (5.9)$$

where  $M_s$  is a neighborhood around voxel  $s$ . The median filter cancels noise and artifacts from misalignment as long as these are small compared to the neighborhood.

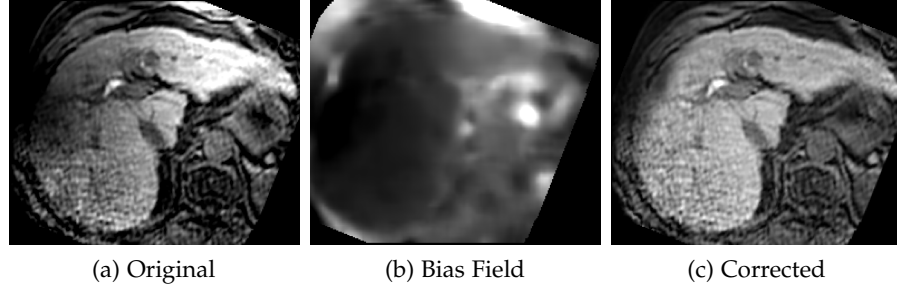


Figure 5.6: Bias field correction outlined at the example from Figure 5.3. Tissue inhomogeneities can be corrected by factoring out a multiplicative bias field.

#### 5.2.1.4 *Pyramidal Integration of Bias Field Correction*

Since interventional data shows bias field artifacts of different extents, a correction on a single resolution would be difficult. To address this issue, the correction was incorporated into the multi-resolution scheme, adding finer bias field details with increasing image resolution. For this purpose, the current bias field estimate  $B$  was redefined as the voxel-wise composition  $B^k(s) \cdot B^u(s)$  of the estimate  $B^k$  known from the previous resolution and the update field  $B^u$  anticipated at the current resolution. Using this notation, yielded

$$B^u(s) \approx \text{median} \left\{ \frac{I_R(t)}{B^k(t) \cdot I_T(t)} \middle| t \in M_s \right\}, \quad (5.10)$$

which essentially pre-corrects the current interventional image  $I_R$  by the known  $B^k$  and estimates the bias field update from the quotient of the remainder.

The bias field correction can be integrated into the pyramidal registration as depicted in Figure 5.4 (right). On the coarsest resolution, the bias field was estimated via Equation 5.9. Then, the interventional image was corrected right before **MRF** optimization and the bias field estimate was passed into the next resolution level. For each subsequent level, the known bias field  $B^k$  was upsampled to the current resolution level by linear interpolation and the bias field update  $B^u$  was estimated via Equation 5.10. Afterwards, the interventional image was corrected before **MRF** optimization and the composed bias field estimate  $B^k \cdot B^u$  was passed into the next resolution level, if any.

### 5.2.1.5 Data and Smoothness

Due to the bias field correction discussed above, it was assumed that tissue intensities are homogeneous in the 3D pre-planning and 3D interventional images from that moment. Moreover, any scaling between the intensities of both images was corrected as byproduct of the bias field correction. A correction for mean intensities is therefore not required and thus, **MAD** can be used as data term<sup>3</sup> directly via

$$D_s(\Delta_s) = \frac{1}{|P||M_s|} \sum_{t \in M_s} |I_T(t + \Delta_s) - I_R(t)|. \quad (5.11)$$

The data term is averaged over a sub-volume  $M_s$  around voxel  $s$  because the previous study has shown that a local similarity measure like **ANTs** achieved already promising results. The edge length of  $M_s$  was set to 20 mm, which was sufficient to cancel out noise and to guarantee that artifacts from crossing applicators skew at most 5% of each local **MAD** estimate.

When different displacements produce similar data costs, e. g. inside homogeneous tissues, a smooth displacement field should be preferred. To this end, a smoothness term<sup>4</sup> was used which penalized different displacements of neighboring voxels via

$$V_{s,t}(\Delta_s, \Delta_t) = \frac{1}{|N|} \|\Delta_s - \Delta_t\|^2. \quad (5.12)$$

Moreover,  $V_{s,t}$  was set to  $+\infty$  if any component of the difference vector  $|\Delta_s - \Delta_t|$  exceeded half the voxel extent in this direction. This ensured that the result is self-intersection free. This property is conserved between different resolution levels by linear interpolation of the displacement fields.

### 5.2.1.6 Parametrization

Regarding the choice of resolution levels, one typically downsamples the image grid recursively by a factor of two, like it was performed in the previous study. Different factors were investigated and found out that a factor of two is too aggressive for challenging cases. On the other hand, factors close to one increased the computational effort significantly. As a compromise, a factor of  $\sqrt{2}$  was used, which is half-way the downsampling that occurs for a factor of two.

The number of downsamplings was set to six, which equated to an overall downsampling factor of eight between the coarsest and the finest resolution. This was sufficient to guarantee that even large tissue displacement were captured by a single voxel on the coarsest

<sup>3</sup> The normalization by  $|P|$  in Equation 5.11 simplified the weighting of terms  $D_s$  and  $V_{s,t}$  in Equation 5.8

<sup>4</sup> The normalization by  $|N|$  in Equation 5.12 simplified the weighting of terms  $D_s$  and  $V_{s,t}$  in Equation 5.8

resolution level. Therefore, the registration targets sub-voxel misalignments, which will be the case on any finer resolution level as well, if the deformable registration performs adequate.

Consequently, the allowed voxel displacements (Equation 5.8) were sampled at a rate of 0.25 voxels along each grid axis and the maximum displacement  $\Delta_s^{\max}$  was limited by a spherical region of one voxel radius. The edge length of the median filter (Equation 5.9 and 5.10) was set to five voxels, which is significantly larger than the remaining misalignment at each level given an adequate deformable registration on the previous levels.

Investigating the trade-off between data and smoothness terms (Equation 5.8) confirmed that displacement fields are smooth, even when the smoothness term is completely disabled ( $\lambda = 1$ ). This is a direct consequence of the  $+\inf$  penalty on potentially self-intersecting displacements. In this study,  $\lambda$  was set to 0.9, which should be a sufficient penalty for the given data to prevent any overfitting in homogeneous tissues. A more detailed evaluation of the parameters is described later (in Section 5.3).

### 5.2.2 Results and Discussion

In addition to the proposed **MRF-BC** registration method, deformable registration based on **FFDs** using cubic B-splines, as well as the **SyN** method (Avants et al., 2008) in combination with **ANTs** (Avants et al., 2011) was evaluated and incorporated into the multi-resolution approach for comparison purposes. These two approaches were chosen because B-splines and deformations computed with **ANTs** achieved the most promising results in the previous study (see Section 5.1) and their source code is available via **ITK**. In contrast to the **DispField**-based deformation, the **SyN**-deformation extends the Lagrangian diffeomorphic registration technique described in Avants et al. (2006) by a new formulation comprising symmetry properties required for a geodesic connecting of two images in the space of diffeomorphic transformations, which guarantees symmetry regardless of the chosen similarity measure. To find the best setup for both reference methods, different similarity measures were investigated, ending up with **MMI** (Mattes et al., 2003). The same pyramid scheme as for the proposed method was used, except that the finest resolution level was excluded for B-spline registration. This was necessary to keep its computation tractable. B-spline knots were evenly distributed along each grid axis, whereby a ratio of six voxels per knot was most adequate for the given data. Internal parameters of both methods were optimized to improve runtime where possible.

Aggregated results of the preliminary experiments for **Data-V2V<sub>0</sub>** are given in Table 5.2. Again, tumor **DSCs** need to be interpreted with caution because of small tumor volumes which are present in this data

Table 5.2: Quality comparison of the proposed **MRF-BC** deformable registration method to the reference methods B-spline and SyN for the preliminary **Data-V2V<sub>0</sub>**. Bold values mark the best approach in each category. Italic values should be interpreted with caution due to small tumors. **MRF-BC\*** is a faster version, which skips the finest resolution level. Values in [ ] are upper bounds on the result quality given optimal rigid (Rig. Mask) and volume-preserving deformable (Def. Mask) registration of the gold standard segmentation masks. Abbrev.: **DSC** - Dice coefficient;  $\overline{ED}/\overline{HD}$  - Euclidean/Hausdorff distance.

Method	<b>DSC</b> [%]		$\overline{ED}$ [mm]		$\overline{HD}$ [mm]	
	Liver	<i>Tumor(s)</i>	Liver	<i>Tumor(s)</i>	Liver	<i>Tumor(s)</i>
Initial	44.2 ± 21.1	1.2 ± 5.1	20.86 ± 8.59	40.22 ± 20.34	58.67 ± 23.16	51.67 ± 22.18
Rigid	90.1 ± 5.3	33.7 ± 26.7	3.28 ± 1.79	4.35 ± 3.31	8.56 ± 5.22	8.92 ± 5.72
Rig. Mask	[92.0 ± 2.0]	[40.8 ± 23.4]				
B-spline	91.4 ± 4.1	39.2 ± 19.5	2.86 ± 1.24	3.72 ± 1.91	8.92 ± 5.77	9.10 ± 5.38
SyN	92.6 ± 2.8	39.1 ± 22.8	2.47 ± 0.94	4.14 ± 3.02	7.29 ± 3.76	9.11 ± 4.68
<b>MRF-BC</b>	<b>94.3 ± 3.3</b>	<b>47.1 ± 28.3</b>	<b>1.92 ± 1.14</b>	<b>3.20 ± 2.58</b>	<b>6.13 ± 4.68</b>	<b>7.23 ± 5.03</b>
<b>MRF-BC*</b>	94.0 ± 2.7	40.9 ± 28.0	2.02 ± 0.87	3.55 ± 2.19	6.42 ± 3.83	7.66 ± 4.03
Def. Mask	[96.7 ± 3.2]	[80.9 ± 13.6]				

Table 5.3: Quality comparison of the proposed **MRF-BC** deformable registration method for **Data-V2V<sub>0</sub>** between both registration tasks: no/all applicator present ( $R_1/R_2$ ). Italic values should be interpreted with caution due to small tumors. MRF-BC\* is a faster version, which skips the finest resolution level. Abbrev.: **DSC** - Dice coefficient;  $\overline{ED}/\overline{HD}$  - Average Euclidean/Hausdorff distance.

Task	Method	<b>DSC</b> [%]		$\overline{ED}$ [mm]		$\overline{HD}$ [mm]	
		Liver	<i>Tumor(s)</i>	Liver	<i>Tumor(s)</i>	Liver	<i>Tumor(s)</i>
$R_1$	Rigid	90.8 ± 3.3	36.2 ± 28.0	3.04 ± 1.14	3.77 ± 2.60	7.79 ± 3.05	7.71 ± 4.67
$R_2$		89.4 ± 6.9	31.2 ± 26.6	3.51 ± 2.30	4.94 ± 3.95	9.34 ± 6.82	10.13 ± 6.63
$R_1 \cup R_2$		90.1 ± 5.3	33.7 ± 26.7	3.28 ± 1.79	4.35 ± 3.31	8.56 ± 5.22	8.92 ± 5.72
$R_1$	MRF-BC	95.0 ± 1.8	51.7 ± 23.3	1.68 ± 0.59	2.36 ± 1.35	5.14 ± 2.37	5.75 ± 3.09
$R_2$		93.6 ± 4.4	42.5 ± 33.2	2.17 ± 1.50	4.04 ± 3.27	7.11 ± 6.18	8.56 ± 4.44
$R_1 \cup R_2$		94.3 ± 3.3	47.1 ± 28.3	1.92 ± 1.14	3.20 ± 2.58	6.13 ± 4.68	7.23 ± 5.03
$R_1$	MRF-BC*	94.6 ± 1.8	43.9 ± 26.6	1.79 ± 0.57	3.02 ± 1.63	5.54 ± 2.38	6.77 ± 3.59
$R_2$		93.3 ± 3.2	38.0 ± 19.9	2.25 ± 1.07	4.07 ± 2.61	7.30 ± 4.85	8.71 ± 6.25
$R_1 \cup R_2$		94.0 ± 2.7	40.9 ± 28.0	2.02 ± 0.87	3.55 ± 2.19	6.42 ± 3.83	7.66 ± 4.03

set. The average ED tumor values should be interpreted with caution too, because the computation of an average ED would euphemize the results for cases where the tumor segmentation masks do not overlap. This results from the fact, that EDs are estimated by computing the averaged distances from one tumor contour to the nearest contour point of the other tumor contour (see Equation 4.4).

As far as the rigid transformation is concerned, the proposed multi-resolution scheme improved all quality measures significantly compared to the initial positioning based on scanner coordinates (see "Initial" in Table 5.2). For instance, the average DSCs more than doubled and the EDs and HDs improved by several centimeters. Comparing rigid results to the given upper bounds on the achievable result quality, it was observed that differences are rather small, e. g. average liver DSCs differed by 1.9 %, while it was 44.2 % initially. Therefore, it can be concluded that rigid results are sufficiently close to the optimal transformation, i. e. significant gains in quality cannot be expected without additional degrees of freedom from deformation.

The proposed MRF-BC deformable registration clearly improved upon rigid results most of the time, but not always. For instance, FFDs registration with B-spline struggled to improve the HD of the tumor(s) and the liver. The latter resulted from the number of cases where artificial deformations occurred at the liver surface, as can be seen in Figure 5.7 and Figure 5.9. SyN did not improve the HD for the tumor tissue; they occasionally even increased the misalignment of the tumor, as seen in Figure 5.8. In contrast, the presented approach always improved upon the rigid results and also scored best in each category (bold values in Table 5.2). Comparing the results to the given upper bounds of the achievable result quality (enclosed by [ ] in Table 5.2), it can be observed that differences are rather small for the liver tissue, i. e. average DSCs differed by only 2.4 %. Therefore, it can be concluded that significant further gains may be expected only with regard to the tumor alignment.

In Table 5.3, results were differentiated with regards to both registration tasks. As could be expected, task  $R_1$  (no applicator present) is less challenging than task  $R_2$  (all applicators present). The difference is most notably for the tumor-related measures and to a smaller degree also for the liver-related measures. The rationale is that the tumors in Data-V2V<sub>0</sub> are rather small in size ( $1.71 \pm 1.61$  mL on average) and are thus more easily affected by applicators placed nearby or inside. The liver, on the other hand, is rather large in size ( $1.60 \pm 0.33$  L on average), making the impact of implanted applicators less significant, except for the HD, which might increase at the puncture site.

Although task  $R_2$  was more challenging than  $R_1$ , the presented MRF-BC registration managed to improve upon the rigid results in each category. Moreover, the magnitude of the improvement was consistent between both registration tasks. For instance, the average

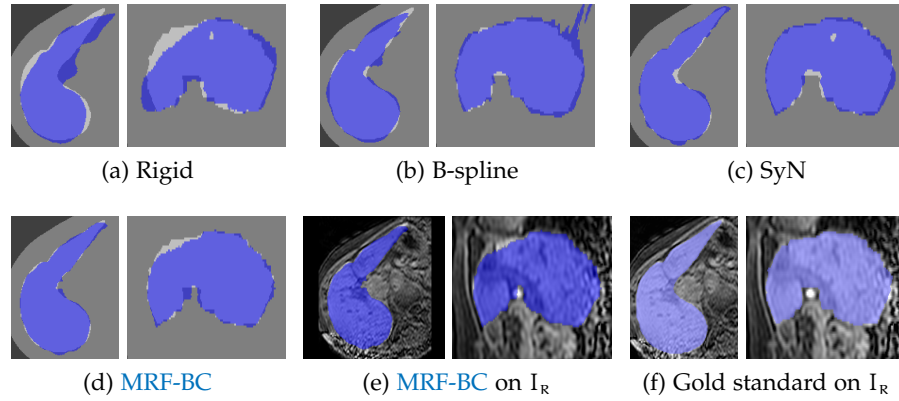


Figure 5.7: Exemplary liver registration results of rigid (a), B-spline (b), SyN (c), and the proposed **MRF-BC** (d) registration. The matching with gold standard (d) and the overlay on the interventional image  $I_R$  (e) are depicted in axial (left) and coronal slices (right). Rigid registration (a) could not account for the liver deformations, while **FFDs** with B-splines (b) produced artificial deformations on the liver surface.

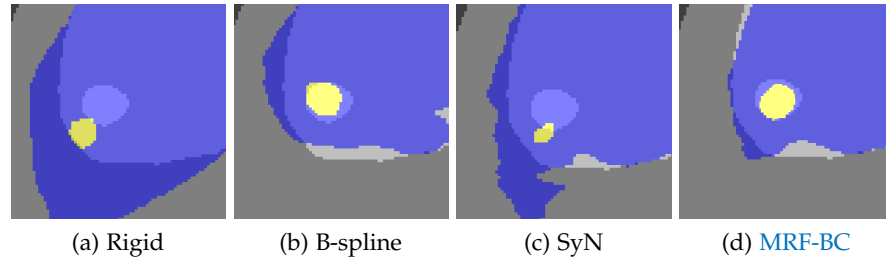


Figure 5.8: Exemplary tumor registration results of rigid (a), B-spline (b), SyN (c), and the proposed **MRF-BC** (d) registration.

liver **DSCs** of  $R_1$  and  $R_2$  both improved by 4.2%, while the average **EDs** and **HDs** decreased by about 1.3 mm and 2.4 mm, respectively. Also tumor-related measures improved consistently for  $R_1$  and  $R_2$ . The average tumor **DSCs** increased by around 13.4%, while the average **EDs** and **HDs** decreased by about 1.2 mm and 1.7 mm, respectively. Due to the consistency, it can be concluded that the proposed **MRF-BC** approach is suited for deformable registration irrespectively of the presence of applicators.

However, the **MRF-BC** registration has limitations in exceptional cases, where the noise is too strong and extensive in the interventional images. An example is shown in Figure 5.10. In such rare cases, additional shape information would be needed for a successful registration.

#### 5.2.2.1 Runtime Comparison

To assess the relevance of the approach for real clinical interventions, the runtimes were also assessed. Comparing the results in Table 5.4,



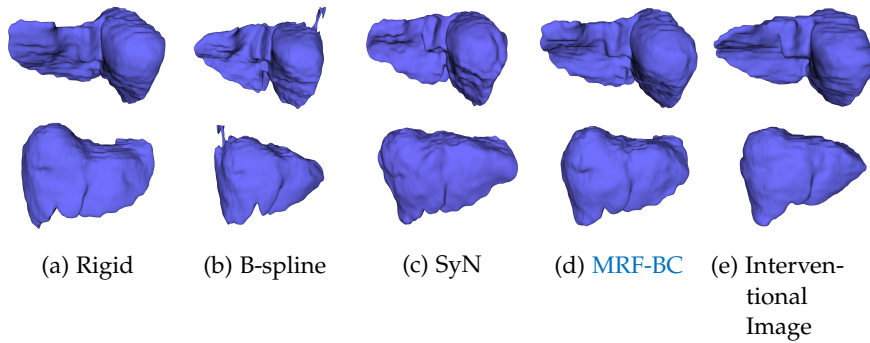


Figure 5.9: Exemplary liver registration results of rigid (a), B-spline (b), SyN (c), and the proposed **MRF-BC** (d) registration as surface renderings from two different viewpoints compared to the interventional image (e). Rigid registration (a) cannot account for the liver deformations, while B-spline registration (b) produced artificial deformations on the liver surface in some cases.

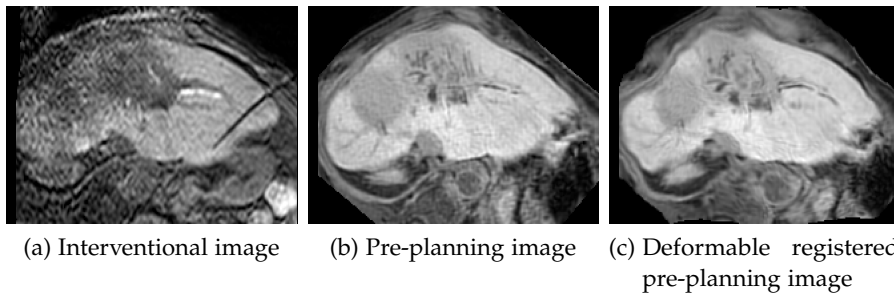


Figure 5.10: Imperfect registration result (c) of the pre-planning image (b) due to strong and extensive noise in the interventional image (a).

it can be observed that B-spline and SyN registration were slowest, taking about six and ten minutes on average, respectively. Runtimes of more than two to three minutes are hardly acceptable in a clinical setting and do not meet the objectives defined in this thesis. The proposed **MRF-BC** approach is sufficiently fast in this respect, taking on average about 115 s seconds.

To further improve the runtime of the proposed **MRF-BC** method, the finest resolution level of the pyramidal approach could be removed. This faster version is marked with a "\*", in Table 5.2, Table 5.3 and Table 5.4. As can be seen from the results, a significant speed-up was gained by sacrificing only little quality. Resulting runtimes ranged around 35 s with results still being better than rigid, B-splines and SyN registration in all categories.

Table 5.4: Comparison of the runtime of the proposed **MRF-BC** deformable registration method to the reference methods B-spline and SyN as well as to rigid registration for the preliminary **Data-V2V<sub>0</sub>**. Bold runtimes mark the fastest deformable approach in each category. All experiments were carried out on consumer hardware. MRF-BC\* is a faster version of the MRF-BC approach, which skips the finest resolution level. Abbreviations: R<sub>1</sub>/R<sub>2</sub> - no/all applicators present.

Method	t <sub>c</sub> [s]		
	R <sub>1</sub>	R <sub>2</sub>	R <sub>1</sub> ∪ R <sub>2</sub>
Rigid	12.2 ± 3.5	15.0 ± 4.0	13.6 ± 3.9
B-spline	364.3 ± 87.6	354.8 ± 70.8	359.8 ± 78.2
SyN	647.1 ± 164.4	599.4 ± 222.8	624.4 ± 190.9
MRF-BC	117.9 ± 34.4	113.2 ± 53.8	115.7 ± 43.6
<b>MRF-BC*</b>	<b>33.5 ± 8.3</b>	<b>38.1 ± 16.2</b>	<b>35.8 ± 12.8</b>

### 5.2.2.2 Conclusion

An original approach to deformable liver registration based on magnetic resonance images was presented. Previous studies addressing this problem are scarce (as figured out in Section 2.5) and the proposed **MRF-BC** approach is the first working solution for an interventional setting, where patient re-positioning, bias field artifacts of different extent, and extensive noise levels as well as computation time pose additional challenges. These issues were successfully addressed by a multi-resolution framework, which combines bias field correction and **MRF** deformable registration in a novel way.

The proposed deformable approach makes less strict assumptions about the bias field than standard pre-processing methods like N3 and N4, which enables a recovery of even very localized artifacts. Contrary to general pre-correction techniques such as PABIC, the presented multi-resolution scheme can recover the bias field artifacts at marginal computational cost. The proposed approach is robust, accurate, and fast, providing a good starting point for computer-assistance during intervention.

However, the approach has limitations in exceptional cases, where the noise is too strong and extensive in the interventional image. Moreover, a more comprehensive evaluation should be performed on a larger data set to investigate the clinical applicability. Especially because the shape of the liver and the deformations vary considerably from patient to patient.

### 5.3 COMPLETE STUDY: JOINT DEFORMABLE LIVER REGISTRATION AND BIAS FIELD CORRECTION FOR MR-GUIDED HDR BRACHYTHERAPY

In order to investigate the clinical applicability of the joint deformable liver registration and bias field correction (MRF-BC) method presented, Data-V2V<sub>1</sub> was used as the basis for evaluation. In addition to the Preliminary Studies A and B, a more detailed evaluation of the method parameters as well as an analysis of different similarity measures for the rigid as well as affine registration was performed. In the Preliminary Study B, a normalized MAD was used for the rigid registration. But in the following complete study, the interventional images have changed and thus, a re-evaluation seems appropriate. Precisely because the results of the proposed deformable MRF-BC registration strongly depend on the rigidly pre-registered results. If the rigid registration fails, the proposed deformable approach cannot compensate for the lack of rigid deformation and would fail, too.

#### 5.3.1 Preprocessing

In this study, pre-planning and interventional images were downsampled to  $1 \times 1 \times 2.5$  mm voxel spacing, which is close to the original resolution as described in Chapter 4. Therefore some adjustments had to be made to handle non-isotropic voxel. Both images were additionally cropped to an axis-aligned ROI. For the pre-planning images, these were extracted automatically from the segmentation mask. For the interventional images, a manual rectangular ROI had to be defined by the medical technical assistance after image acquisition. These pre-processed images were used as input for the rigid and affine registration.

#### 5.3.2 Material and Methods

All experiments were carried out on consumer hardware comprising an Intel® Core™ i7-7700K @ 4.2 GHz and 16 GB RAM. Data-V2V<sub>1</sub> included 3D pre-planning eTHRIVE and several 3D interventional T1-TFE images of 53 patients.

First, rigid and affine registration was performed using the similarity measures defined in Section 5.1, including NGFs, which have not been investigated before. Second, the proposed deformable MRF-BC approach was applied to the best results of the rigid and affine pre-registration with different, appropriate parameter combinations. Since all similarity measures, parameters, methods, and data sets used in this study were already described in detail in the previous studies, the results for each part will directly presented and discussed.

Most of the results are shown in boxplots or aggregated tables. Boxplots are useful to study the distributional characteristics of a group of scores as well as the level of the scores. On each box, the central mark indicates the median, while the bottom and top edges of the box indicate the 25th and 75th percentiles, respectively. The whiskers extend to the most extreme data points not considered outliers, and the outliers are plotted individually as 'o' symbols.

### 5.3.3 Rigid and Affine Registration

To investigate and compare different similarity measures for the rigid and affine registrations, the FAIR toolbox was used. It enables the investigation of several transformation, regularization, interpolation, and similarity measure types and it can be used in MATLAB. In addition, parts of the source code are provided as parallelized C code. As already stated above, the selection of an appropriate rigid or affine pre-registration is required and assumed for the subsequent deformable registration. Hence, MI, NCC, normalized MAD, and NGF were compared with each other in terms of accuracy and computing time. Both types of registration were incorporated into a multi-resolution scheme similar to the already presented (see Section 5.1).

#### 5.3.3.1 Similarity Measures

First, rigid and affine liver DSC values of the four similarity measures were compared for registration task  $R_1$ . The results are shown in Figure 5.11. In general, rigid registration performed better than affine registration. An exception is MI where affine registration performed slightly better. NCC performed on average worse than the other similarity measures, especially using an affine transformation which failed in most cases. Best results could be obtained with NGFs in combination with a rigid registration. This combination finally achieved a median DSC of approx. 0.91. For all similarity measures, there seem to be two to five outliers where the registration did not perform well. Some of them will be discussed later in more detail.

The resulting TREs with respect to the tumor centroid distances  $\bar{d}_{\text{Tum}}$  for registration task  $R_1$  are shown in Figure 5.12. These results seem to correlate with the DSCs, which means that NGFs in combination with a rigid registration performed best and achieved a TRE of approximately 5 mm. Rigid registrations with MI and MAD achieved almost identical results, which also matches to the findings of the preliminary studies. Again, NCC could not achieve sufficient results and performed worse than the other similarity measures.

Hence short computation times are important within a clinical settings, a runtime comparison was performed. The runtimes for rigid and affine registrations are shown in Figure 5.13. Rigid registration finished in most cases in less than 10 s, except for NGF. In this case,

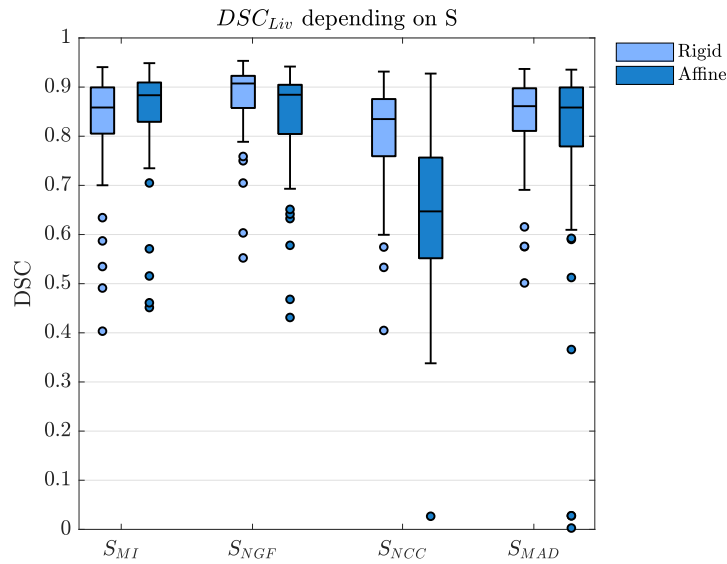


Figure 5.11: Comparison of rigid and affine liver **DSC** values for different similarity measures  $S$ .

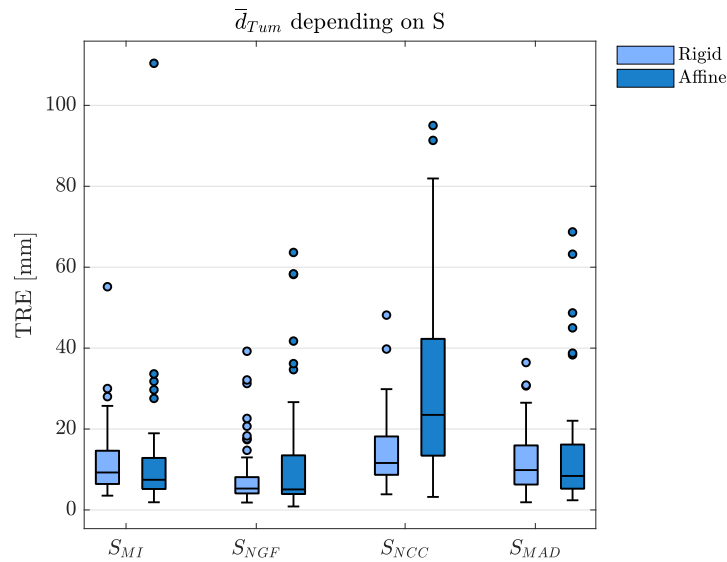


Figure 5.12: Comparison of rigid and affine **TRE** between tumor centroids ( $\bar{d}_{Tum}$ ) for different similarity measures  $S$ .

runtimes ranged between 15s and 30s for most data sets and in about 60s for exceptional data sets. Affine registration calculation usually took more than twice as long as rigid registration because of the larger parameter space. However, no quality improvements could be observed. Affine registration often tended to fit onto the body boundaries due to the lack of regularization, as can be seen in Figure 5.14.

It can be summarized that the best results in terms of accuracy and computation time could be achieved by using a rigid registration with **NGFs**. The aggregated results for both registration tasks  $R_1$  and  $R_2$  are

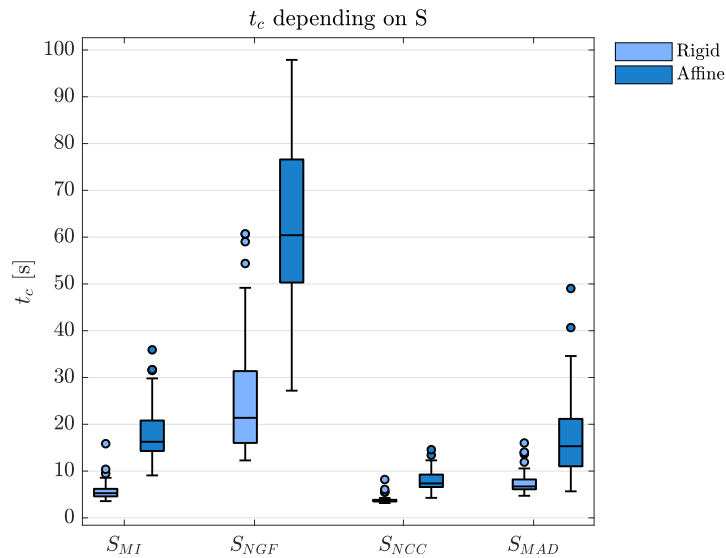


Figure 5.13: Comparison of the runtimes  $t_c$  of rigid and affine registrations for different similarity measures  $S$ .

compared to the upper bounds of the optimal rigid registration and presented in Table 5.6. Finally, rigid registration achieved an average liver **DSC** of 0.88 and tumor **DSC** of 0.39 for task  $R_1$ . Compared to the upper **DSC** bounds of 0.92 and 0.46, it can be seen that the registration probably failed in rare cases. Regarding the quality of the tumor registration, landmark-based and tumor centroid **TREs** of 7.9 mm and 8.6 mm could be achieved for task  $R_1$ .

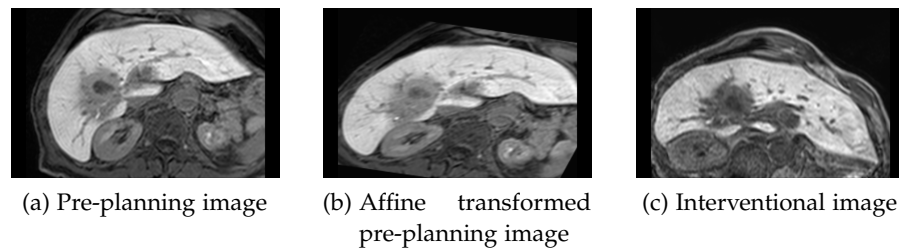


Figure 5.14: Exemplary case where the standard affine registration failed because it tends to fit to the body boundaries due to the lack of regularization.

A comparison of the landmark-based **TRE** to the variability between different observers, who selected landmarks manually, is shown in Table 5.5. The results indicate that for three different observer, who selected about 60 landmarks in 20 data sets, an inter-observer variability of 1.96 mm was reached. The landmarks were set by one clinical expert with several years of experience and two field experts on the same vessel bifurcations. For the landmark selection, the images were isotropically resampled to  $1 \text{ mm}^3$  voxel spacing in order to enable a more precise selection of the landmarks.

Table 5.5: TRE between anatomical landmarks for the best rigid registration using  $S_{\text{NGF}}$ . In addition, inter-observer variabilities between three different observers are shown.

TRE [mm]	Inter-observer variability [mm]			
Rigid	1 & 2	2 & 3	1 & 3	1 & 2 & 3
<b>7.87 ± 8.0</b>	1.55 ± 1.4	2.29 ± 1.2	2.04 ± 1.2	1.96 ± 1.3

In the last section, a detailed investigation of similarity measures has shown that a rigid registration with NGFs performed best for **Data-V2V<sub>1</sub>**. A reason for this could be that NGFs are based on image gradients and that the liver is contrast enhanced in both, pre-planning and interventional images. This leads to strong gradient magnitudes at the liver boundaries compared to the surrounding tissue and thus would enable a more precise alignment. Although it achieved the best results compared to the other similarity measures, the objectives of my thesis have not yet been met. In terms of accuracy, the results of the rigid registration are still below a DSC of 0.94 and above a TRE of 5 mm. In contrast, runtimes of about 30 s would already meet the set objectives.

But rigid registration failed in three registration cases. These cases are already marked in Figure 5.11 and Figure 5.14 as outliers. Figure 5.15 shows the corresponding pre-planning and interventional images of one case. It can be seen that the FOV was extremely cropped so that the liver is no longer completely contained. Such cases cannot be covered at present and are therefore excluded from the evaluation of the deformable MRF-BC registration in the next section. To enable a clinical application nevertheless, these special data sets would have to be pre-registered manually by the MRI technician after image acquisition or must be correctly acquired in advance.

#### 5.3.4 Deformable Registration

For the best rigid registration, the proposed joint deformable registration and bias field correction approach (MRF-BC) was extensively evaluated. First, different parameter combinations were investigated and discussed (in more detail compared to the Preliminary Study B). Second, the overall best results are presented for different tasks  $R_1$  and  $R_2$ . Finally, the clinical applicability of the proposed V2V registration is discussed.

##### 5.3.4.1 Parametrization

Parameter tests were only performed for task  $R_1$ , where the interventional image did not contain any applicators. The proposed MRF-BC

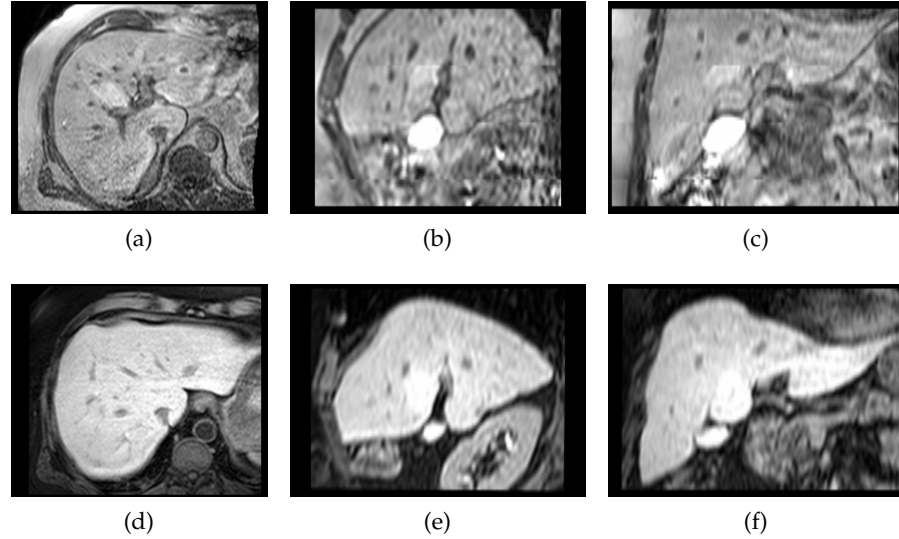


Figure 5.15: Exemplary case where the rigid registration failed. It can be seen that the FOV of the interventional image (a-c) did not contain the whole liver and thus, the transformation of the pre-planning image (d-f) failed. Anatomical view from left to right: axial, sagittal, coronal

registration procedure has in principle only two parameters, which influence the quality and the computing time:  $\Delta_s^{\max}$  specifies the maximum displacement and  $\lambda$  defines the weighting of the data term in Equation 5.8.

Figures 5.16 and 5.17 show deformable V2V registration results of the liver and tumor for different parameter combinations of  $\Delta_s^{\max}$  and  $\lambda$ . Regarding  $\lambda$  it can be seen that values of 0.8, 0.9, and 1.0 achieved the highest liver DSC, lowest tumor centroid ( $\bar{d}_{\text{Tum}}$ ) TRE, and landmark ( $\bar{d}_{\text{LM}}$ ) TRE. However, the quality differences of the internal reference structures ( $\bar{d}_{\text{Tum}}$  or  $\bar{d}_{\text{LM}}$ ) are rather small compared to the liver DSCs with respect to varying  $\lambda$  values.

Additionally, the influence of  $\Delta_s^{\max}$  on the registration quality was investigated for  $\lambda=0.9$  and  $\lambda=1.0$ . The results show that the median DSC and TRE values differ only slightly. But for  $\Delta_s^{\max}=3$  and  $\Delta_s^{\max}=4$ , the values of the outliers have slightly improved. But the computation time  $t_c$  increased drastically for larger displacements  $\Delta_s^{\max}=3$  and  $\Delta_s^{\max}=4$  (as can be seen in Figure 5.18) from about 70 s up to 400 s and more. Since there was no significant quality gain using higher values,  $\Delta_s^{\max}$  was set to 2 for further evaluations.

#### 5.3.4.2 Final Results and Discussion

A comparison of the tumor TREs for both registration tasks ( $R_1/R_2$ ) is illustrated in Figure 5.19. It shows that the median values of the tumor centroid distances  $\bar{d}_{\text{Tum}}$  were about 2.6 mm and 4.1 mm for the tasks



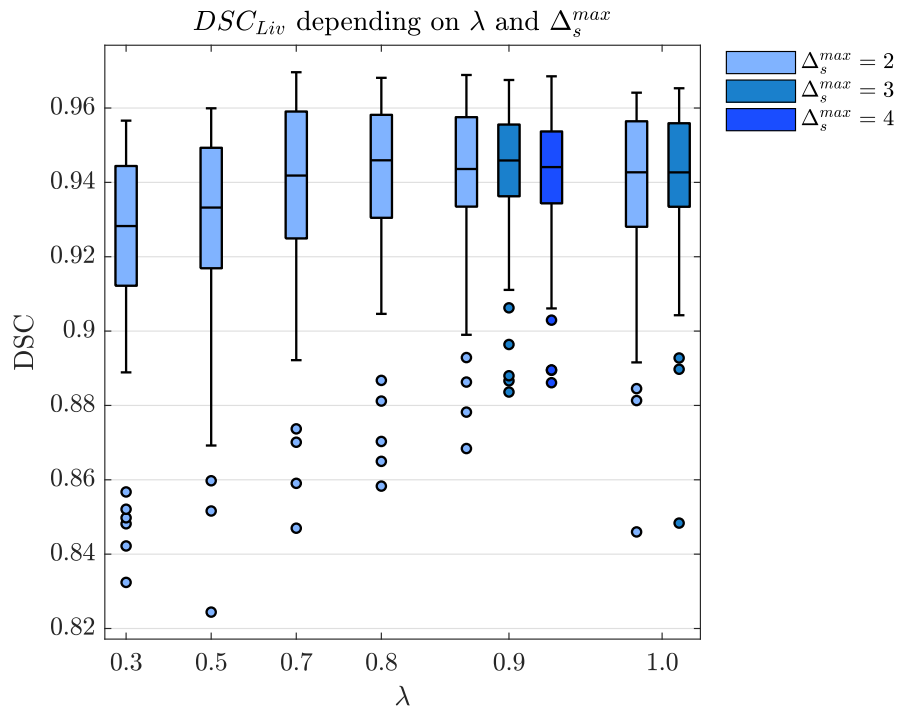


Figure 5.16: Comparison of liver  $DSCs$  of the proposed **MRF-BC** registration for combinations of  $\lambda$  and  $\Delta_s^{max}$ .

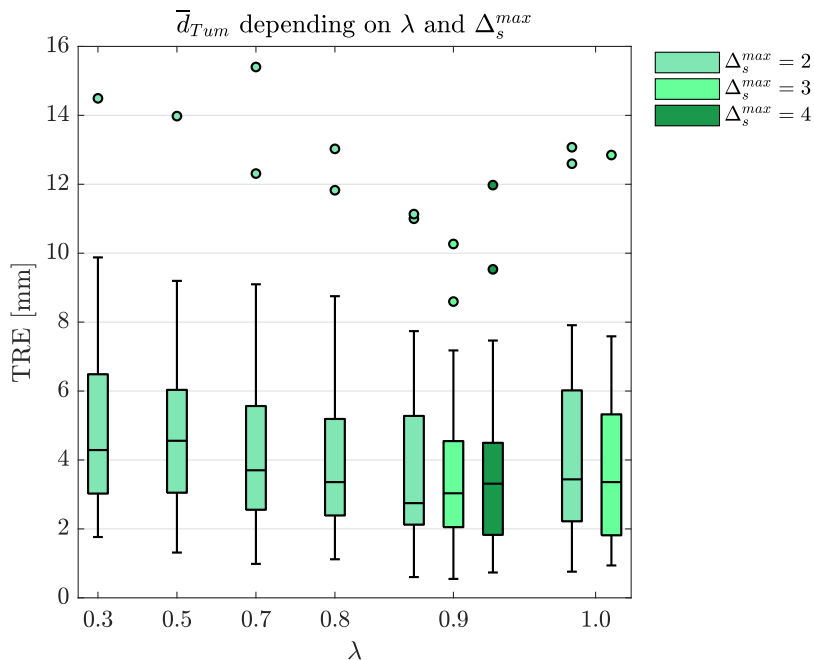


Figure 5.17: Comparison of tumor centroid distances ( $\bar{d}_{Tum}$ ) of the proposed **MRF-BC** registration for combinations of  $\lambda$  and  $\Delta_s^{max}$ .

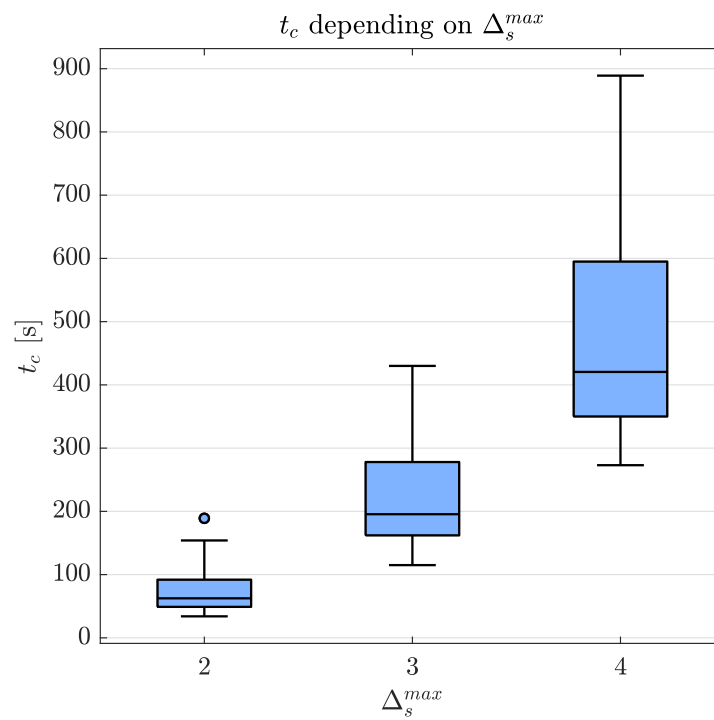


Figure 5.18: Comparison of the runtimes ( $t_c$ ) of the proposed MRF-BC registration for different values of  $\Delta_s^{max}$ .

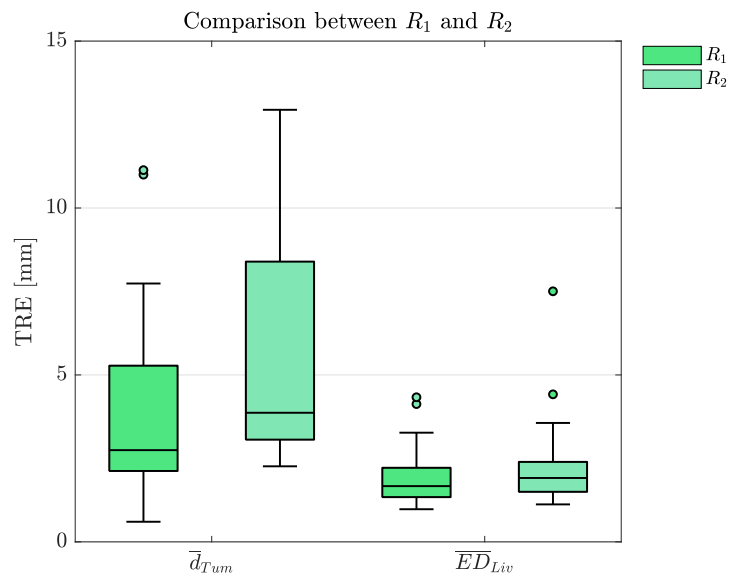


Figure 5.19: Comparison of TREs of the proposed MRF-BC registration between both registration tasks  $R_1$  and  $R_2$ .

Table 5.6: Quality specification of the proposed **MRF-BC** deformable registration method with the best parametrization ( $\lambda = 0.9; \Delta_s^{\max} = 2$ ) for **Data-V2V<sub>1</sub>** between both registration tasks: no/all applicator present ( $R_1/R_2$ ). *Italic values should be interpreted with caution due to small tumors. Values in [ ] are upper bounds on the result quality given optimal rigid (Rig. Mask) and volume-preserving deformable (Def. Mask) registration of the segmentation masks. Abbrev.: DSC - Dice similarity coefficient;  $\overline{ED}/\overline{HD}^{95}$  - Average Euclidean/Hausdorff distance;  $\bar{d}$  - Euclidean distance between landmarks (LMs) or tumor centroids (TCs).*

Task	Method	DSC [%]		$\overline{ED}$ [mm]	$\overline{HD}^{95}$ [mm]		$\bar{d}$ [mm]	
		Liver	<i>Tumor(s)</i>	Liver	Liver	<i>Tumor(s)</i>	LMs	TCs
$R_1$	Rigid	$87.6 \pm 8.0$	$39.1 \pm 24.6$	$4.02 \pm 2.85$	$10.39 \pm 7.32$	$9.12 \pm 7.80$	$7.87 \pm 8.05$	$8.61 \pm 8.03$
$R_2$		$83.8 \pm 12.1$	$27.4 \pm 23.3$	$5.36 \pm 4.52$	$14.36 \pm 12.31$	$14.75 \pm 15.53$	-	$14.26 \pm 15.96$
$R_1 \cup R_2$		$86.5 \pm 9.6$	$35.6 \pm 24.7$	$4.42 \pm 3.47$	$11.59 \pm 9.22$	$10.74 \pm 10.80$	-	$10.24 \pm 11.09$
[ $R_1 \cup R_2$ ]	Rig.Mask	[ $91.9 \pm 2.9$ ]	[ $45.5 \pm 22.5$ ]	[ $2.53 \pm 0.91$ ]	[ $6.99 \pm 3.16$ ]	[ $6.35 \pm 3.20$ ]	-	[ $5.61 \pm 3.45$ ]
$R_1$	MRF-BC	$94.0 \pm 2.3$	$54.2 \pm 18.8$	$1.87 \pm 0.71$	$5.91 \pm 3.08$	$5.20 \pm 2.32$	$3.75 \pm 2.18$	$3.70 \pm 2.48$
$R_2$		$92.4 \pm 4.0$	$40.8 \pm 23.7$	$2.36 \pm 1.46$	$7.38 \pm 4.90$	$8.19 \pm 5.50$	-	$6.75 \pm 5.87$
$R_1 \cup R_2$		$93.6 \pm 3.0$	$50.3 \pm 21.1$	$2.01 \pm 1.01$	$6.34 \pm 3.73$	$6.10 \pm 3.79$	-	$4.62 \pm 4.03$
[ $R_1 \cup R_2$ ]	Def.Mask	[ $96.5 \pm 2.5$ ]	[ $85.1 \pm 15.6$ ]	-	-	-	-	-

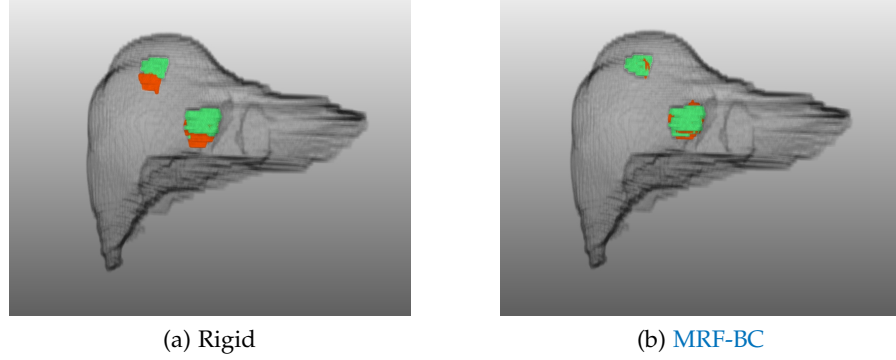


Figure 5.20: Illustration of an example where the tumor alignment after rigid registration (a) could be considerably improved by a [MRF-BC](#) deformable registration (b). The 3D visualization shows the reference liver as well as the reference tumor (red) and the transformed tumor surfaces (green).

$R_1$  and  $R_2$ , respectively.  $\overline{ED}_{Liv}$ ) values of the liver differed only slightly between 1.7 mm and 4.1 mm for the tasks  $R_1$  and  $R_2$ .

Table 5.6 presents final aggregated quality values (mean and standard deviations) of the proposed [MRF-BC](#) deformable [V2V](#) registration with the best parametrization ( $\lambda = 0.9$ ;  $\Delta_s^{\max} = 2$ ) as well as the results of the rigid registration approach for [Data-V2V<sub>1</sub>](#) for both registration tasks: no/all applicator present ( $R_1/R_2$ ). In addition, the complete quality specifications per patient are given in the Appendix in Tables A.1 and A.2. It can be seen that the proposed method could greatly improve the rigid results and that the liver [DSC](#) values are close to the upper bounds of the volume-preserving deformable registration of the segmentation masks. Figure 5.20 and Figure 5.21 illustrate examples where the tumor alignment after rigid registration could be considerably improved by a [MRF-BC](#) deformable registration. For task  $R_1$ , average [TREs](#) of 3.7 mm and 3.75 mm could be achieved between tumor centroids ( $\overline{d}_{Tum}$ ) and anatomical landmarks ( $\overline{d}_{LM}$ ). The latter are additionally compared to the inter-observer variability in Table 5.7. It can be seen that the achieved [TRE](#) of 3.75 mm is already quite well compared to the value of  $1.96 \pm 1.3$  mm calculated for the inter-observer variability.

In terms of computation time, it could be shown that the proposed joint deformable liver registration and bias field correction ([MRF-BC](#)) approach is sufficiently fast using the best parametrization (see Figure 5.18). In combination with a rigid pre-registration, the complete [V2V](#) approach can be executed in less than 100s on average, which thus meets the objectives for this task.

The results achieved for the task  $R_2$  are slightly worse than for  $R_1$ , what was to be expected because of the artifacts from the implanted applicators which impaired the similarity computation in this areas. For those images, a [TRE](#) of 6.75 mm combined with a high standard devi-

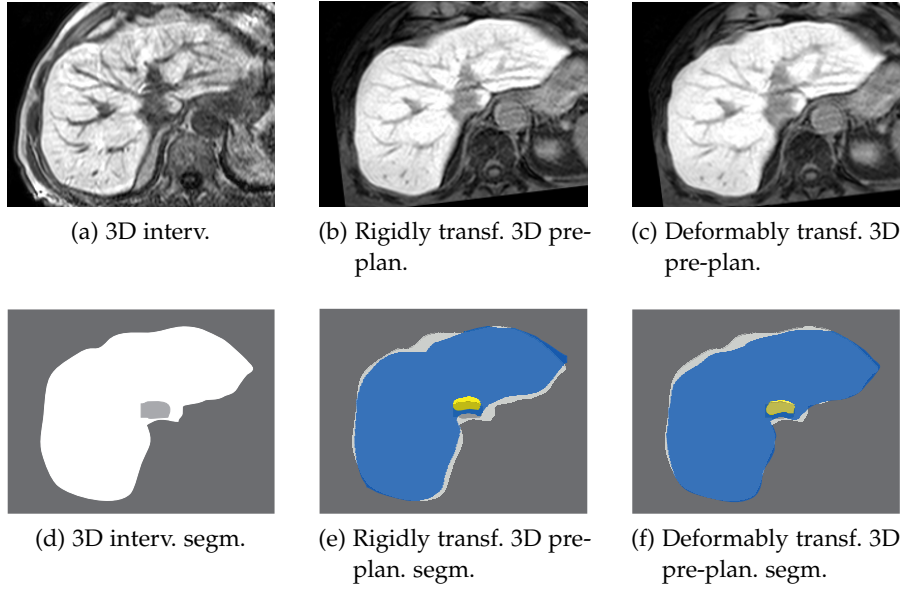


Figure 5.21: Illustration of an exemplary good result of the presented deformable [MRF-BC](#) registration approach. (a) shows the 3D interventional image, (b) the rigidly transformed 3D pre-planning image, (c) the deformedly transformed 3D pre-planning image, (d) the 3D interventional segmentation mask, (e) the rigidly transformed 3D pre-planning segmentation mask, and (f) the deformedly transformed 3D pre-planning segmentation mask. Blue: liver segmentation mask, Yellow: tumor segmentation mask.

ation of 5.87 mm was achieved between the evaluated tumor centroids. Comparing these values with the median scores from Figure 5.19 shows that there exist rare cases with a high TRE. An exemplary case is illustrated in Figure 5.22. In this case, the presented deformable registration approach was not able to compensate for the liver deformation (see Figure 5.22(c,f)) because of the high misalignment after rigid registration (see Figure 5.22(b,e)). This case could also explain the slight improvements of the outlier cases for higher values of  $\Delta_s^{\max}$  that could be observed in Figure 5.16. To compensate for such cases, a more precise rigid pre-registration is needed. This could include a manual correction step performed by the [MRI](#) technician immediately

Table 5.7: TRE between anatomical landmarks for the best parametrization of the [MRF-BC](#) deformable registration. In addition, inter-observer variabilities between three different observers are shown.

TRE [mm]		Inter-observer variability [mm]			
Rigid	MRF-BC	1 & 2	2 & 3	1 & 3	1 & 2 & 3
$7.87 \pm 8.0$	$3.75 \pm 2.1$	$1.55 \pm 1.4$	$2.29 \pm 1.2$	$2.04 \pm 1.2$	$1.96 \pm 1.3$

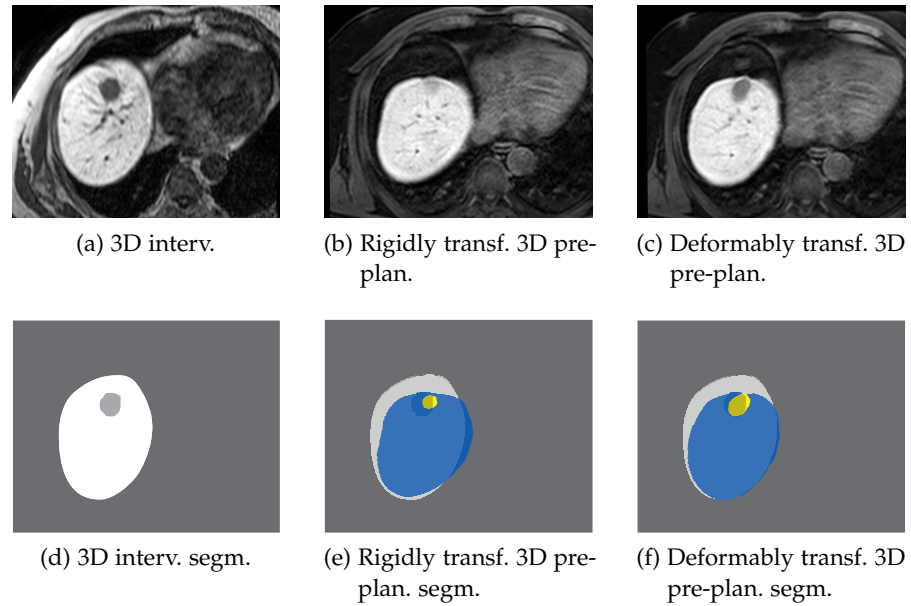


Figure 5.22: Illustration of an exemplary case where the presented deformable **MRF-BC** registration approach was not able to compensate for the liver deformation (c,f) because of the high misalignment after rigid registration (b,e). (a) shows the 3D interventional image, (b) the rigidly transformed 3D pre-planning image, (c) the deformedly transformed 3D pre-planning image, (d) the 3D interventional segmentation mask, (e) the rigidly transformed 3D pre-planning segmentation mask, and (f) the deformedly transformed 3D pre-planning segmentation mask. Blue: liver segmentation mask, Yellow: tumor segmentation mask.

after the rigid registration.

In summary, an novel approach to deformable liver registration based on interventional magnetic resonance images was presented in Section 5.2 and extensively evaluated on a wide range of real patient data sets. It could be shown, that the approach can cope with most of the challenges which were named in Section 1.2.1. The proposed strategy meets all of the objectives set in Section 3 and is robust against minor parameter changes. This means in particular, it achieves final **DSC** of 0.94 for the liver as well as **TREs** of 3.75 mm and 3.7 mm for the tumor centroids and anatomical landmarks, respectively. In addition, it can also be applied to post-interventional data sets (task  $R_2$ ) but with a compromise on accuracy. Despite the high accuracy achieved for task  $R_1$ , the runtimes of the presented approach were sufficiently short for a clinical application.

## 6.1 PRELIMINARY STUDY

Parts of the results of the following preliminary study have already been published at CURAC 2017 as a full paper (König et al., 2017). Therein, an investigation of rigid and deformable intensity-based registration methods from ITK was performed to find out the suitability of such methods for a V2S registration.

In this study, Data-V2S<sub>0</sub> was used which comprises 22 3D interventional THRIVE images and 552 2D interventional T1-FFE slices. Since the T1-FFE images have slightly different intensity characteristics, a square root filter was used to normalize intensities and to deal with intensity peaks. After pre-processing, the 2D interventional images were initialized according to their scanner coordinates which provides a good starting point for further registration.

Liver deformation and tumor displacement in the 2D interventional images are mainly caused by different states of breathing during image acquisition. Such deformations caused by the breathing have already been illustrated in Figure 1.8. Consequently, the evaluation focuses on available rigid, affine, or deformable registration approaches that are able to compensate for these deformations. Overall, about 90 different combinations of transformations, similarity measures, and optimizers were evaluated, which results in a total number of 49.680 V2S registration tasks.

### 6.1.1 Rigid Registration

Table 6.1 briefly summarizes the results of the best combinations. For rigid and affine registration, several combinations perform equally well, i.e. a 3D Euler, a 3D versor, and a quaternion-based transform in combination with MI or ANTs and LBFGS or gradient descent. All registrations yielded comparable DSC and  $\overline{ED}$  values and could not improve the initial values (see Table 6.1). In a few cases, rigid registration was able to improve the initial overlap (see Figure 6.1) but there was no substantial improvement in the majority of cases, because of a huge number of failed registrations.

### 6.1.2 Deformable Registration

With regards to deformable registration, most of the methods (e.g. FEM, DispField) were not applicable to V2S registration without ex-

Table 6.1: Quality and runtime comparison of V2S registration methods that are available in ITK for Data-V2S<sub>0</sub>. Abbrev.: DSC - Dice coefficient;  $\overline{ED}/\overline{HD}$  - Euclidean/Hausdorff distance.

V2S	Average	Liver	
	$t_c$ [s]	DSC [%]	$\overline{ED}$ [mm]
Initial	-	$83 \pm 13$	$7.9 \pm 4.5$
Rigid	1	$83 \pm 13$	$6.8 \pm 4.6$
Affine	1	$82 \pm 17$	$7.2 \pm 4.9$
B-spline	1	$84 \pm 12$	$6.7 \pm 4.3$
DispField	-	failure	
FEM	-	failure	

tensive modifications of the ITK codebase. FFDs with B-splines proved to be the most suitable. In this context, the ANTs and MI similarity measures performed best. However the resulting liver DSC and  $\overline{ED}$  values indicated that the improvement of the initialization was rather significant.

### 6.1.3 Discussion

In terms of V2S registration, it can be concluded that the evaluated registration approaches from ITK did not significantly improve the registration accuracy compared to an initialization of the 2D interventional images according to their scanner coordinates. Furthermore, the results were not precise enough for a clinical setting. The high standard deviations indicated that there are many cases, where rigid or deformable registration methods worsened the results of the initialization and could not compensate the liver deformations caused by breathing.

One reason could be the lack of information in the 2D interventional images and the many degrees of freedom during the registration process. The lack of information means in particular that the correct deformation of the liver was not known for certain breathing states. For the 3D interventional images, only the deformation at acquisition time is known. So there might be some cases, where it is impossible to perform an accurate registration without additional information.

On the other hand, the used square root filter might not have been sufficient in all cases to compensate for the extensive intensity inhomogeneities in the 2D interventional images. As a direct consequence and in combination with the high degrees of freedom, many local optima could arise in the area surrounding the initialization.



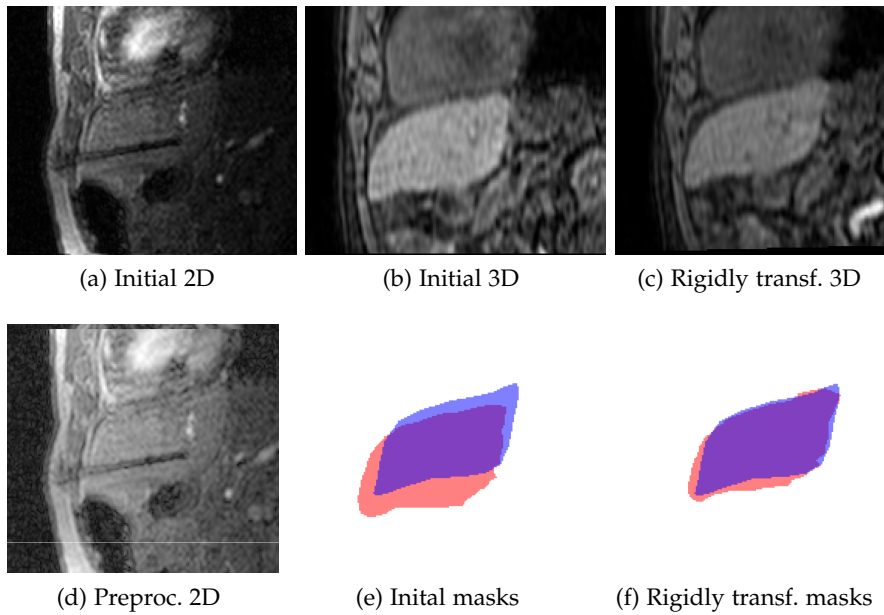


Figure 6.1: Exemplary [V2S](#) registration results between the preprocessed 2D interventional image (d) and the 3D interventional image. Sub-figures (b) and (e) show the results after an initialization according to the scanner coordinates. Sub-figures (c) and (f) show the results after rigid registration.

In summary, the following findings can be made and should be considered in the approach to be developed afterwards:

- A scanner coordinate-based initialization already provides a good initial matching.
- Available rigid and deformable registration approaches are not able to improve the result quality without additional information about the breathing.
- Intensity inhomogeneities in the 2D interventional images should be adequately compensated.

Hence, a registration framework would be needed that can provide an appropriate workaround for the missing breathing information. Such a framework will be introduced, evaluated, and discussed in the next section.

## 6.2 COMPLETE STUDY

In this study, a new registration framework will be presented which can cope with the limitations outlined above. Such a [V2S](#) registration should be able to correctly transfer the already transformed pre-planning information (from the [V2V](#) registration) on the 2D interventional images to finally improve the tumor puncture in terms

of accuracy and time. It is assumed that the 3D pre-planning images were already correctly registered to the 3D interventional images and that the patient was not repositioned during the intervention. This assumption is important for the approach because the initial scanner coordinates of the 2D interventional images will be used as guideline for further computations.

### 6.2.1 *Material and Methods*

The approach was developed and evaluated on the basis of [Data-V2S<sub>1</sub>](#), which comprises 54 3D interventional images and 9738 corresponding 2D interventional [T1-FFE](#) image slices at different time points. All experiments were carried out on consumer hardware comprising an Intel® Core™ i7-7700K @ 4.2 GHz and 16 GB RAM.

The idea of the approach to be developed is that the radiologist does not necessarily need a perfect deformable registration for each 2D image slice acquired at different breathing states, but only for those where the pre-planning information could be transformed accurately enough. Hence, a registration framework will be presented that is able to transform pre-planning information to the 2D interventional images and additionally shows the degree of the matching quality. The degree of the matching quality can be estimated by the similarity between the 3D interventional image and those 2D images which have the same or a very similar breathing time. It is assumed that such cases show a high similarity and that other cases, where the breathing state strongly differs between both images, show a rather low similarity. In the next sections, the presented steps are described in more detail.

#### 6.2.1.1 *Preprocessing*

In the preliminary study, it was outlined that the intensity inhomogeneities in the 2D interventional images should be adequately compensated before or within the registration. For this reason, the already proposed bias field correction from the [MRF-BC V2V](#) registration was adapted and applied to the 2D interventional images. But it has to be assumed that the 3D interventional images were already properly bias field-corrected and that the initial overlap of the liver in both images is large enough. [Figure 6.2](#) illustrates a result of the bias field correction for the 2D interventional [T1-FFE](#) images. The correction could be performed in a few milliseconds per image within a multi-resolution pyramid.

#### 6.2.1.2 *Multiplanar Reconstruction*

In a next step, it was investigated how to reduce the degrees of freedom of the [V2S](#) registration by using multiplanar reconstruction ([MPR](#)) volumes of the 3D interventional images instead of the images

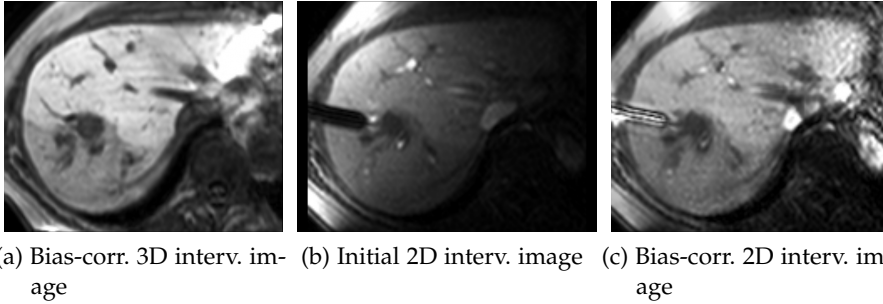


Figure 6.2: Illustration of the bias field correction that was applied to the 2D interventional images (c). The bias corrected 3D interventional image (a) was used as a basis for the correction of the 2D interventional images (b).

themselves. Given a current 2D interventional image slice, the following steps were performed sequentially:

1. The position and orientation of the current 2D interventional slice was obtained from their scanner coordinates.
2. These scanner coordinates were used to find the corresponding multiplanar reconstructed slice within the 3D interventional planning image holding the same scanner coordinates.
3. For each different orientation of the 2D images, a multiplanar reconstructed slice was computed from the 3D image by linear interpolation of the adjacent grid points.
4. For each multiplanar reconstructed slice, a sub-volume within the 3D interventional planning image was resampled orthogonal to the image plane in both directions. The resampling was performed with increments of 1 mm and a range of 1.5 cm in each direction in order to compensate for smaller liver deformation.
5. Finally, *MPR* volumes with a size of  $352 \times 335 \times 30$  mm were created and used for the subsequent matching strategy with the 2D interventional images.

The essential steps of the proposed *V2S* registration are illustrated in Figure 6.3.

### 6.2.1.3 Similarity Matching

Next, the matching quality between each 2D interventional image and corresponding 3D *MPR* image needs to be estimated. Therefore, it is first necessary that the interventional radiologist acquires a brief sequence of images over one breathing cycle. Then, the similarity matching was performed as follows:

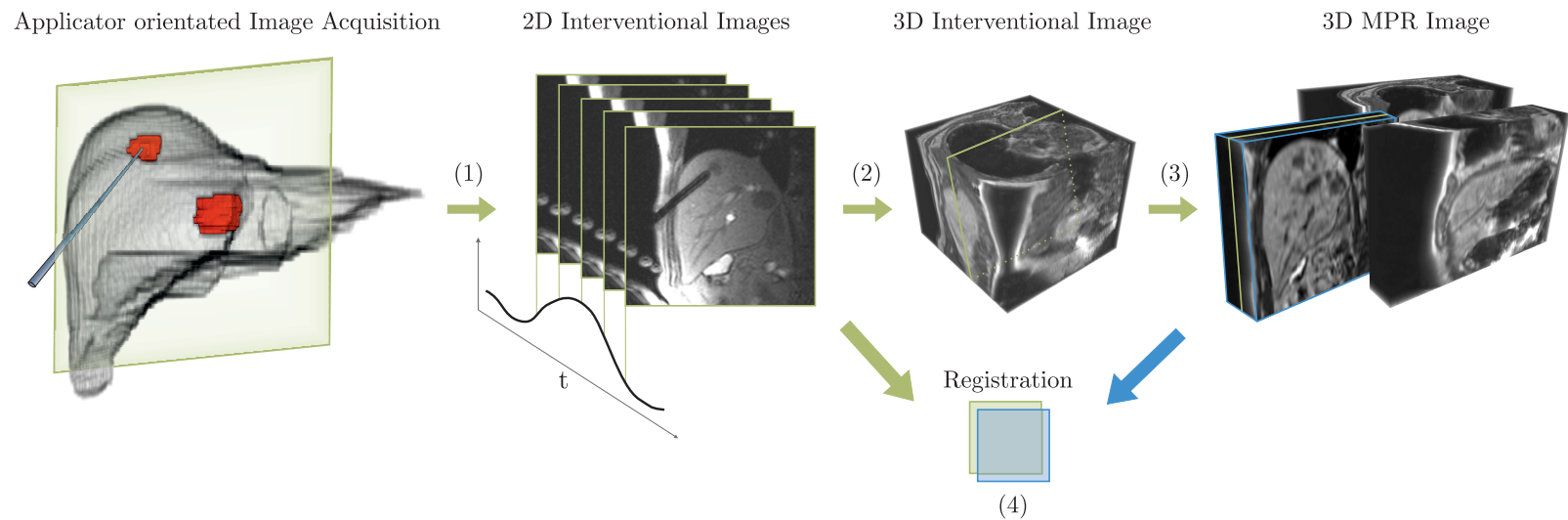


Figure 6.3: Illustration of the essential steps of the proposed **V2S** registration approach. (1) 2D interventional image slices are acquired according to the planned applicator trajectory. (2) A multiplanar reconstructed image slice is computed from the 3D image according to the scanner coordinates of the current 2D image slice. (3) A **MPR** volume is constructed and used for the similarity matching with the stack of 2D interventional images (4).

1. For each 2D interventional image of the acquired stack, a rigid registration with the 3D MPR image and a similarity computation between both images was performed.
2. Similarities and associated images were sorted in a descending order and the best and worst matches were selected. It is assumed that the best match corresponds best and that the worst match corresponds worst to the breathing state of the 3D MPR.
3. Next, the matching quality was estimated for each new 2D interventional image with the same orientation and position by using the already calculated maximum and minimum similarity values.
4. Depending on the quality of the matching, the pre-planning information could be color-coded and overlaid on the 2D interventional image giving the interventional radiologist feedback on how well the transformed planning information fits the current 2D image. For example, by using a color scale from green (best match) to red (worst match), as illustrated in Figure 6.4.

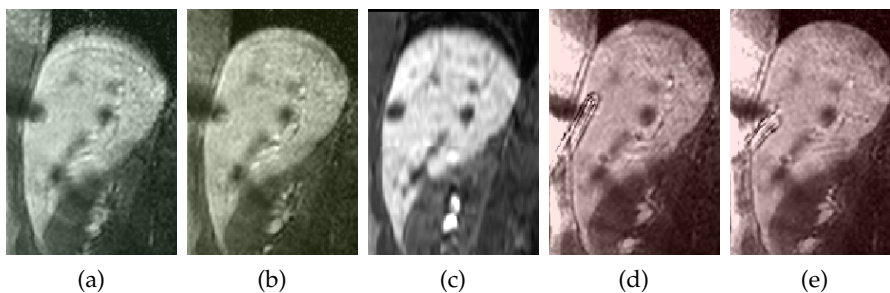


Figure 6.4: Illustration of an exemplary color-coding depending on the similarity between 2D interventional images (a-b, d-e) with same orientations and the 3D MPR image (c) as a feedback system for the interventional radiologist during the tumor puncture. Green overlay means high similarity and red overlay low similarity.

MI was selected as a similarity measure for the matching procedure within the presented V2S registration approach because other measures did not seem appropriate for the given Data-V2S<sub>1</sub>. NGFs did not perform well because of the low gradient information within the 2D interventional images in contrast to the 3D MPR. Other measures like MAD, SSD, or its normalized versions were inappropriate since image intensity properties of the T1-TFE and T1-FFE images do not match perfectly within the liver, i. e. vessel structures are brighter in the T1-FFE images.

### 6.2.2 Results and Discussion

All of the presented steps could be performed in less than 1 s on the used consumer hardware, allowing clinical applicability in this regard. The suitability in terms of accuracy is now being evaluated and discussed. This evaluation was performed by a comparison of segmentation masks of the 3D MPR image with the rigidly registered segmentation masks of the best matches from each 2D interventional image stack. Overall, a number of 1024 best matching 2D interventional images was examined. Since the proposed V2S registration approach is parameter-free and data set Data-V2S<sub>1</sub> does not contain different image sequences, the mean values and standard deviations of the results can be aggregated and are presented in Table 6.2.

Table 6.2: Quality specifications of the proposed V2S approach. Italic values should be interpreted with caution due to small tumors. Values in [ ] are upper bounds on the result quality given optimal volume-preserving deformable (Def. Mask) registration of the gold standard segmentation masks. Abbrev.: DSC - Dice coefficient;  $\overline{ED}/\overline{HD}$  - Euclidean/Hausdorff distance;  $\bar{d}$  - Euclidean distance between landmarks (LMs) or tumor centroids (TCs).

	DSC [%]		$\overline{ED}$ [mm]	
Method	Liver	<i>Tumor</i>	Liver	<i>Tumor</i>
V2S	92.6 ± 4.2	55.2 ± 25.6	3.10 ± 1.56	3.13 ± 3.47
Def. Mask	[ 97.1 ± 2.5 ]	[ 92.7 ± 5.7 ]	-	-
	$\overline{HD}$ [mm]		$\bar{d}$ [mm]	
Method	Liver	Tumor	LMs	TCs
V2S	8.10 ± 4.13	6.05 ± 4.50	4.77 ± 2.14	4.51 ± 2.29

On average, the proposed V2S registration method achieved a liver DSC of 0.93, a tumor centroid distance  $\bar{d}_{\text{Tum}}$  of 4.51 mm and an anatomical landmark distance  $\bar{d}_{\text{LM}}$  of 4.77 mm. DSCs of an optimal volume-preserving deformable registration of the gold standard segmentation masks are also presented in order to figure out upper bounds for the registration and to show that even clinical experts are not able to create a perfect ground truth on the given data.

Figure 6.5 shows the DSCs and  $\overline{ED}$  values of the liver and tumor in more detail. For the liver, the median DSC was about 0.94 and the median  $\overline{ED}$  was 2.78 mm. The presented tumor DSC<sub>Tum</sub> and average surface-to-surface distances  $\overline{ED}_{\text{Tum}}$  should be interpreted with caution due to the small tumor sizes. It can be seen that there are cases where the tumors did not overlap at all. This occurred in cases where tumor sizes are small but it does not necessarily imply that the registration

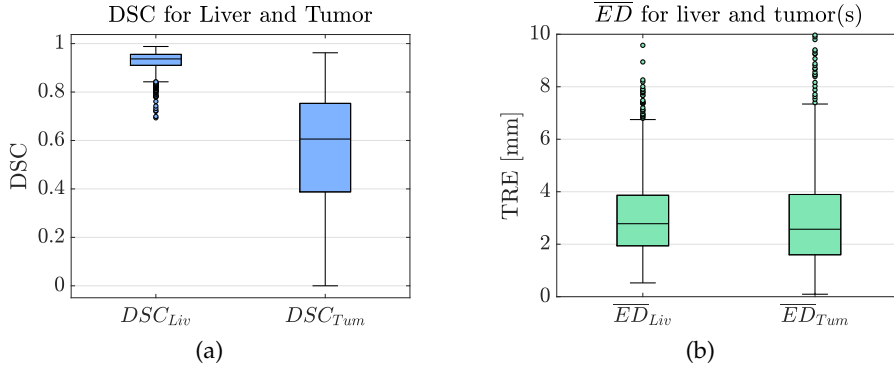


Figure 6.5: Comparison of liver and tumor **DSC** (a) and  $\overline{ED}$  (b) values of the proposed **V2S** registration.

accuracy is low. A more meaningful evaluation measure with respect to the tumors is the distance between the tumor centroids, which is presented in Figure 6.6(a).

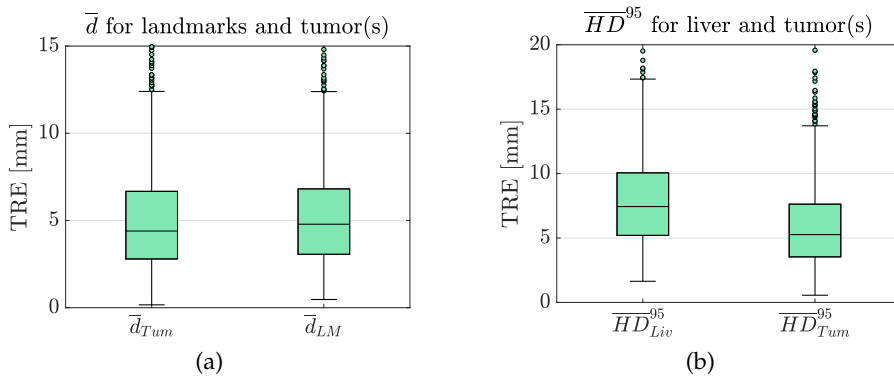


Figure 6.6: Comparison of **TREs** (a) between tumor centroids as well as anatomical landmarks and of liver and tumor  $\overline{HD}^{95}$  (b) of the proposed **V2S** registration.

It can be seen that the overall median and mean **TREs** of the presented approach are in the range between 4.4 mm ( $\bar{d}_{Tum}$ ) and 4.67 mm ( $\bar{d}_{LM}$ ) as well as 4.5 mm ( $\bar{d}_{Tum}$ ) and 4.77 mm ( $\bar{d}_{LM}$ ), respectively, which would be sufficient in terms of the accuracy. Figure 6.7 illustrates an exemplary case where a good tumor alignment could be achieved.

The plots show that there were some outliers with a **TRE** higher than 12 mm. An exemplary case, where the alignment of the best matching 2D interventional image with 3D **MPR** image was imprecise, is shown in Figure 6.8. Either, the similarity matching simply failed because of strong artifacts or many local optima. It could also occur that none of the 2D interventional images from the current stack had the same breathing state as the corresponding 3D interventional image. The proposed method cannot cope with such cases at this time because an estimation or classification of the "best" similarity is not possible.

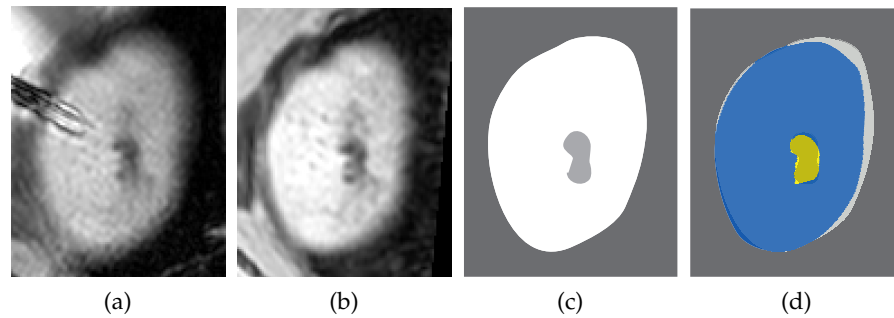


Figure 6.7: Illustration of an exemplary good result of the proposed **V2S** registration approach. In this case, a high tumor and liver alignment was achieved. (a) shows the interventional 2D image slice, (b) the corresponding 3D **MPR** slice, (c) the gold standard segmentation mask of the interventional 2D image, and (d) the overlay of the transformed 3D **MPR** segmentation mask on the segmentation mask of the interventional 2D image.

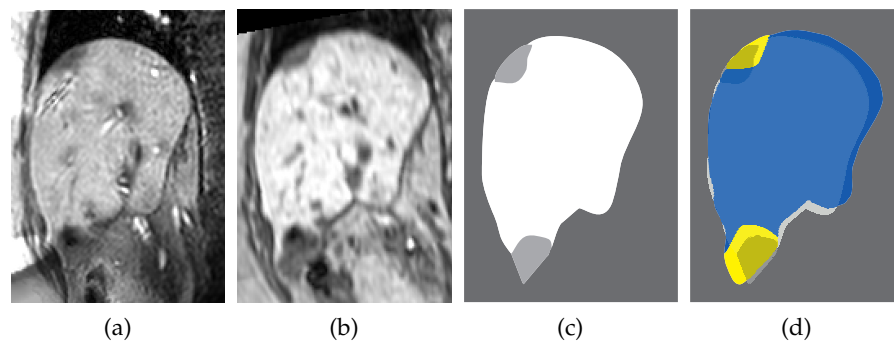


Figure 6.8: Illustration of an exemplary bad result of the proposed **V2S** registration approach. In this case, a low tumor alignment was achieved because of deformations that could not be compensated by the rigid registration. (a) shows the interventional 2D image slice, (b) the corresponding 3D **MPR** slice, (c) the gold standard segmentation mask of the interventional 2D image, and (d) the overlay of the transformed 3D **MPR** segmentation mask on the segmentation mask of the interventional 2D image.

To work around this problem, more information about the current breathing state is necessary, e. g., by using a **MRI** compatible breathing belt or a tracking system like the Moiré Phase Tracking (Gumus et al., 2015). In this context, it was investigated whether the deformations can be compensated with a deformable registration like the **MRF-BC** approach presented early. However, the application of the procedure had no impact on the results and thus was neglected from further evaluations. Another possibility would be a preliminary acquisition of the 3D pre-planning image at different breathing states to create a patient specific 4D liver breathing model. Additionally, images could be acquired in the same decubital position which is used during



the intervention. Such small changes to the clinical workflow could significantly simplify and improve computer-assisted registration.

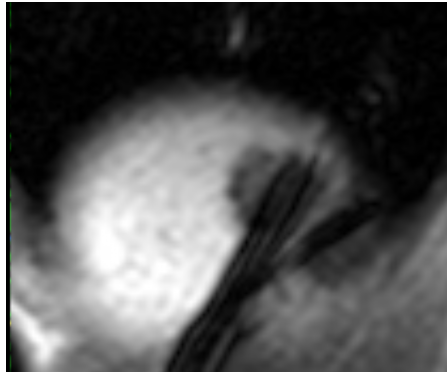


Figure 6.9: Illustration of the limitations of the [V2S](#) registration approach. The similarity matching step failed in cases where two or more applicators were present in a 2D interventional slice near the liver boundary.

Other cases that cannot be covered by the presented procedure include images that were acquired at the exact moment when the needle is pierced through the skin. In these images the tissue is strongly deformed and thus the similarity measure can become imprecise. Other limitations occur in cases where two or more applicators were present in a 2D interventional slice near the liver boundary. Figure 6.9 illustrates an exemplary case.

In summary, a [V2S](#) registration framework was proposed that is able to transfer diagnostic information from the 3D interventional image on the 2D interventional image slices. The system achieved a sufficiently high accuracy with regard to the tumor [TRE](#), which was on average lower than the accuracy set as one of the objectives in this thesis. In addition, the presented system is fast enough to transfer information on each temporal 2D interventional slice that is acquired during the tumor puncture using current available consumer hardware. Since no information is available regarding the current breathing state, which also influences the liver deformations, an appropriate strategy was presented that is able to cope with this. The presented method has limitations in rare cases, when image slices near the liver boundary contain several applicators.



## CONCLUSION

---

The overall goal of this thesis was to improve MRI-based high-dose rate brachytherapy interventions by means of computer-assistance. At first, the clinical workflow was analyzed to figure out limitations that could possibly be solved using suitable computer-assisted methods. It was found out, that the main flaw is the lack of an adequate transfer of pre-planning information onto the interventional images to support the radiologist during the tumor puncture. The contributions of the thesis are the investigation of existing and - in case necessary - the development of novel strategies to provide a solution suitable for challenges faced in interventional settings seen in the clinical routine. Hence, meaningful objectives were set in cooperation with a clinical partner.

To achieve the objectives, a two-step approach was presented which comprised a fast and accurate volume-to-volume as well as a subsequent volume-to-slice registration. For both tasks, separate challenges were defined depending on the available data sets of each task. Next, a comprehensive investigation and evaluation of the related works and of state-of-the-art registration methods was performed in several preliminary studies. With regard to the related work, it could be demonstrated that there is still a need for further research because the few comparable works did not meet the defined objectives. In addition, most of the investigated, freely available rigid, affine, and deformable registration methods did not work well without further adjustments either. Based on findings from the preliminary studies discussed in this thesis, new strategies were derived for both tasks which have addressed the problems identified in a meaningful way.

Considering the volume-to-volume registration, a novel joint deformable liver registration and bias field correction (MRF-BC) method was presented which is, to the best of my knowledge, the first working solution for an interventional setting, where patient re-positioning, bias field artifacts of different extent, and extensive noise levels as well as limited time pose additional challenges. These issues were successfully addressed by a multi-resolution framework, which combines bias field correction and MRF deformable registration in a novel way. It could be demonstrated on a wide range of real patient data sets that the proposed approach is robust, accurate, and fast, providing a good starting point for computer-assistance during intervention. The presented MRF-BC was able to meet all of the defined objectives

and it was robust against minor parameter changes. It achieved final Dice similarity coefficient values of 0.94 for the liver as well as target registration errors of 3.75 mm and 3.7 mm for the tumor centroids and anatomical landmarks, respectively. In addition, the presented method can also be applied to post-interventional data sets but with a compromise on accuracy. The average runtime of the presented rigid and deformable approach was about 100 s, which is sufficiently short for a usage within a clinical setting.

With regard to volume-to-slice registration, a framework was proposed that is able to transfer diagnostic information on the interventional image slices to guide the radiologists during the puncture of the tumors. The main challenge was to cope with the different breathing states during the intervention because breathing has an influence on the deformation of the liver and thus, on the accuracy of the registration. Since no additional information are available, an appropriate strategy was presented that is able to achieve a sufficiently high accuracy for those 2D interventional images that matched best to the breathing state of the corresponding 3D data set. In this context, a visual feedback system was proposed, which allows the radiologist to assess the quality of the transformed information during the puncture in real-time. The presented volume-to-slice registration approach achieved median and mean target registration errors of 4.4 mm and 4.67 mm between corresponding tumor centroids as well as 4.5 mm and 4.77 mm, between corresponding landmarks on vessel bifurcations, respectively. Thus, it was shown that the system was able to meet the objectives on average but holding relatively high standard deviations.

To sum up, the presented methods were able to achieve the defined objectives to a sufficient extent. The suitability of the methods was proven on a high number of real data sets comprising gold standard annotations from a clinical expert with several years of experience which were used for the evaluation. However, they also have limitations in rare cases for which the accuracy decreases. These cases either included strong artifacts from many implanted applicators, unusually high deformations of the liver, or a limited field of view cropping parts of the liver volume. Future work should mainly focus on the adaption of the clinical workflow to ease the registration tasks, which means in particular, an acquisition of the liver with different patient positioning and at different breathing states, e. g., inhale, exhale, and intermediate, during the diagnostic stage prior to intervention. This would enable the creation of a patient-specific liver breathing model which could be used within the volume-to-slice registration to allow a highly accurate registration at any point in time and for any 2D interventional image.

# A

## APPENDIX

---

Table A.1: Complete quality specifications of the proposed MRF-BC deformable registration of Data-V2V<sub>1</sub> per patient (Part 1 of 2).

data	DSC [%]		$\overline{ED}$ [mm]	$\overline{HD}^{95}$ [mm]		$\overline{d}$ [mm]
	Liver	Tumor	Liver	Liver	Tumor	TCs
1	96,20	63,40	1,20	3,20	3,17	1,54
2	93,87	63,37	1,87	6,27	3,88	2,72
3	94,20	53,59	1,65	5,00	4,42	2,41
4	95,34	88,03	1,63	4,72	3,85	2,44
5	95,79	40,75	1,51	4,22	6,72	5,86
6	93,54	46,91	2,21	8,38	7,64	6,64
7	96,52	70,86	1,24	3,72	3,30	2,06
8	87,82	45,59	4,13	15,24	14,03	11,00
9	93,28	15,51	2,37	7,50	7,13	5,51
10	92,58	0,00	2,23	7,37	-	-
11	94,33	9,57	1,64	5,10	7,82	6,61
12	96,23	53,79	1,10	2,97	5,91	3,72
13	92,96	64,19	2,12	6,27	5,60	4,79
14	93,42	79,92	2,23	7,54	2,44	1,32
15	94,34	70,66	1,38	3,78	3,43	1,75
16	93,87	42,10	1,88	5,12	5,75	4,16
17	94,80	54,67	1,53	5,00	3,85	2,19
18	94,38	49,72	1,82	5,08	7,21	5,57
19	95,96	71,65	1,34	3,44	4,34	3,26
20	96,89	55,86	0,98	2,69	4,89	2,13
21	96,14	83,27	1,20	3,29	2,50	1,01
22	94,65	43,85	1,73	5,00	4,69	2,65
23	92,37	50,92	2,42	7,14	5,85	5,42
24	93,49	62,61	2,07	5,59	5,74	5,04
25	93,48	39,86	2,24	6,16	8,43	7,45
26	96,89	32,45	1,09	2,97	4,24	2,48
27	94,83	62,70	1,58	5,00	4,22	3,24
28	93,71	36,50	1,94	5,83	-	-
29	89,90	35,80	3,05	9,94	11,04	11,13
30	94,10	32,69	1,69	5,00	6,37	5,28
31	91,23	33,10	2,20	7,16	-	-
32	95,70	88,46	1,22	4,03	2,69	0,96
33	94,68	61,10	1,82	6,71	3,87	2,78
34	94,93	64,49	1,62	5,00	3,92	2,30

Table A.2: Complete quality specifications of the proposed MRF-BC deformable registration of Data-V2V<sub>1</sub> per patient (Part 2 of 2).

data	DSC [%]		$\overline{ED}$ [mm]	$\overline{HD}^{95}$ [mm]		$\overline{d}$ [mm]
	Liver	Tumor	Liver	Liver	Tumor	TCs
35	92,84	48,86	2,24	6,71	5,77	2,83
36	88,63	26,07	3,27	12,30	7,97	7,74
37	96,18	72,81	1,23	3,16	3,88	1,95
38	94,11	62,73	1,99	5,94	5,64	2,12
39	93,13	77,39	2,52	8,60	2,97	1,18
40	89,29	72,49	2,73	9,85	2,80	2,27
41	95,26	80,72	1,28	3,77	3,72	0,60
42	86,84	32,77	4,33	18,20	2,99	1,32
43	94,95	0,00	1,60	5,13	-	-
44	95,72	53,48	1,34	4,10	5,18	3,78
45	96,30	0,00	1,34	3,78	-	-
46	96,57	34,69	1,13	2,80	4,09	4,06
47	95,23	68,17	1,52	4,00	4,79	2,42
48	96,04	42,59	1,41	4,03	-	-
49	96,25	49,09	1,12	2,97	6,22	3,87
50	93,46	47,51	1,91	6,27	6,82	3,86
51	95,12	28,64	1,82	5,10	8,27	7,59
52	87,43	0,00	3,56	11,31	-	-
53	91,37	3,49	2,36	7,50	12,42	11,13
54	87,22	11,89	3,30	11,15	8,64	8,39
55	93,33	72,85	2,18	7,07	3,28	2,26
56	94,36	41,96	1,40	4,10	12,99	9,97
57	95,41	49,70	1,32	3,72	4,81	2,89
58	95,76	47,53	1,28	3,77	5,39	3,70
59	95,06	44,16	1,61	5,00	4,28	2,40
60	92,19	49,63	2,43	7,63	6,90	5,81
61	94,38	70,45	1,86	5,00	4,57	2,44
62	80,83	0,00	7,51	24,65	26,46	26,20
63	92,27	41,92	2,35	8,17	8,89	8,21
64	85,98	24,68	4,42	13,24	13,17	12,94
65	93,67	53,19	1,92	5,94	4,72	3,12
66	95,50	61,28	1,44	4,88	4,05	3,06
67	95,01	0,00	1,56	4,67	-	-
68	94,51	78,27	1,99	5,55	5,71	3,75





## REFERENCES

---

- Adam, R., Delvart, V., Pascal, G., Valeanu, A., Castaing, D., et al. (2004). "Rescue surgery for unresectable colorectal liver metastases downstaged by chemotherapy: a model to predict long-term survival." In: *Annals of Surgery* 240.4, p. 644.
- Adams, R. B., Aloia, T. A., Loyer, E., Pawlik, T. M., Taouli, B., and Vauthey, J.-N. (2013). "Selection for hepatic resection of colorectal liver metastases: expert consensus statement." In: *HPB* 15.2, pp. 91–103.
- Archip, N., Tatli, S., Morrison, P., Jolesz, F., Warfield, S. K., and Silverman, S. (2007). "Non-rigid registration of pre-procedural MR images with intra-procedural unenhanced CT images for improved targeting of tumors during liver radiofrequency ablations." In: *International Conference on Medical Image Computing and Computer-Assisted Intervention (MICCAI)*. Springer, pp. 969–977.
- Avants, B. B., Schoenemann, P., and Gee, J. C. (2006). "Landmark and intensity-driven lagrangian frame diffeomorphic image registration: Application to structurally and functionally based interspecies comparison." In: *Medical Image Analysis* 10, pp. 397–412.
- Avants, B. B., Epstein, C. L., Grossman, M., and Gee, J. C. (2008). "Symmetric diffeomorphic image registration with cross-correlation: evaluating automated labeling of elderly and neurodegenerative brain." In: *Medical Image Analysis* 12.1, pp. 26–41.
- Avants, B. B., Tustison, N. J., Song, G., Cook, P. A., Klein, A., and Gee, J. C. (2011). "A reproducible evaluation of ANTs similarity metric performance in brain image registration." In: *Neuroimage* 54.3, pp. 2033–2044.
- Ayav, A., Germain, A., Marchal, F., Tierris, I., Laurent, V., et al. (2010). "Radiofrequency ablation of unresectable liver tumors: factors associated with incomplete ablation or local recurrence." In: *The American Journal of Surgery* 200.4, pp. 435–439.
- Azar, F. S., Metaxas, D. N., and Schnall, M. D. (2001). "A deformable finite element model of the breast for predicting mechanical deformations under external perturbations." In: *Academic Radiology* 8.10, pp. 965–975.
- Bajcsy, R. and Kovačič, S. (1989). "Multiresolution elastic matching." In: *Computer Vision, Graphics, and Image Processing* 46.1, pp. 1–21.
- Birkfellner, W., Figl, M., Kettenbach, J., Hummel, J., Homolka, P., Scherthaner, R., Nau, T., and Bergmann, H. (2007). "Rigid 2D/3D slice-to-volume registration and its application on fluoroscopic CT images." In: *Medical Physics* 34.1, pp. 246–255.

- Bookstein, F. L. (1989). "Principal warps: Thin-plate splines and the decomposition of deformations." In: *IEEE Transactions on Pattern Analysis and Machine Intelligence* 11.6, pp. 567–585.
- Böttger, T., Ruiter, N. V., Stotzka, R., Bendl, R., and Herfarth, K. K. (2003). "Registration of CT and MRI volume data of the liver." In: *International Congress Series*. Vol. 1256. Elsevier, pp. 118–123.
- Boykov, Y., Veksler, O., and Zabih, R. (2001). "Fast approximate energy minimization via graph cuts." In: *IEEE Transactions on Pattern Analysis and Machine Intelligence* 23.11, pp. 1222–1239.
- Bro-Nielsen, M. and Gramkow, C. (1996). "Fast fluid registration of medical images." In: *Visualization in Biomedical Computing*. Springer, pp. 265–276.
- Brock, K. K., Dawson, L. A., Sharpe, M. B., Moseley, D. J., and Jaffray, D. A. (2006). "Feasibility of a novel deformable image registration technique to facilitate classification, targeting, and monitoring of tumor and normal tissue." In: *International Journal of Radiation Oncology\* Biology\* Physics* 64.4, pp. 1245–1254.
- Broit, C. (1981). "Optimal registration of deformed images."
- Brown, L. G. (1992). "A survey of image registration techniques." In: *ACM Computing Surveys (CSUR)* 24.4, pp. 325–376.
- Carrillo, A., Duerk, J. L., Lewin, J. S., and Wilson, D. L. (2000). "Semi-automatic 3-d image registration as applied to interventional MRI liver cancer treatment." In: *IEEE Transactions on Medical Imaging* 19, pp. 175–185.
- Center, M. M. and Jemal, A. (2011). "International trends in liver cancer incidence rates." In: *Cancer Epidemiology and Prevention Biomarkers* 20.11, pp. 2362–2368.
- Cha, D. I., Lee, M. W., Song, K. D., Oh, Y.-T., Jeong, J.-Y., et al. (2017). "A prospective comparison between auto-registration and manual registration of real-time ultrasound with MR images for percutaneous ablation or biopsy of hepatic lesions." In: *Abdominal Radiology* 42.6, pp. 1799–1808.
- Chalana, V. and Kim, Y. (1997). "A methodology for evaluation of boundary detection algorithms on medical images." In: *IEEE Transactions on Medical Imaging* 16.5, pp. 642–652.
- Cheng, X., Zhang, L., and Zheng, Y. (2015). "Deep similarity learning for multimodal medical images." In: *Computer Methods in Biomechanics and Biomedical Engineering: Imaging & Visualization* 6.3, pp. 248–252.
- Choi, J.-Y., Choi, J.-S., Kim, M.-J., Lim, J. S., Park, M. S., Kim, J. H., and Chung, Y. E. (2010). "Detection of hepatic hypovascular metastases: 3D gradient echo MRI using a hepatobiliary contrast agent." In: *Journal of Magnetic Resonance Imaging* 31.3, pp. 571–578.
- Christensen, G. E., Miller, M. I., and Vannier, M. (1994). "A 3d deformable magnetic resonance textbook based on elasticity." In:

- AAAI Spring Symposium Series: Applications of Computer Vision in Medical Image Processing*, pp. 153–156.
- Collettini, F., Schnapauff, D., Poellinger, A., Denecke, T., Schott, E., et al. (2012). "Hepatocellular carcinoma: computed-tomography-guided high-dose-rate brachytherapy (CT-HDRBT) ablation of large (5–7 cm) and very large (> 7 cm) tumours." In: *European Radiology* 22.5, pp. 1101–1109.
- Collignon, A., Maes, F., Delaere, D., Vandermeulen, D., Suetens, P., and Marchal, G. (1995). "Automated multi-modality image registration based on information theory." In: *Information Processing in Medical Imaging*. Vol. 3. 6, pp. 263–274.
- Davis, M. H., Khotanzad, A., Flamig, D. P., and Harms, S. E. (1997). "A physics-based coordinate transformation for 3-D image matching." In: *IEEE Transactions on Medical Imaging* 16.3, pp. 317–328.
- De Jong, M. C., Pulitano, C., Ribero, D., Strub, J., Mentha, G., et al. (2009). "Rates and patterns of recurrence following curative intent surgery for colorectal liver metastasis: an international multi-institutional analysis of 1669 patients." In: *Annals of Surgery* 250.3, pp. 440–448.
- Dupuis, P., Grenander, U., and Miller, M. I. (1998). "Variational problems on flows of diffeomorphisms for image matching." In: *Quarterly of Applied Mathematics* 56.3, pp. 587–600.
- Elhawary, H., Oguro, S., Tuncali, K., Morrison, P. R., Tatli, S., Shyn, P. B., Silverman, S. G., and Hata, N. (2010). "Multimodality non-rigid image registration for planning, targeting and monitoring during CT-guided percutaneous liver tumor cryoablation." In: *Academic Radiology* 17.11, pp. 1334–1344.
- Fei, B., Duerk, J. L., Boll, D. T., Lewin, J. S., and Wilson, D. L. (2003). "Slice-to-volume registration and its potential application to interventional MRI-guided radio-frequency thermal ablation of prostate cancer." In: *IEEE Transactions on Medical Imaging* 22.4, pp. 515–525.
- Ferlay, J., Colombet, M., Soerjomataram, I., Dyba, T., Randi, G., et al. (2018). "Cancer incidence and mortality patterns in Europe: Estimates for 40 countries and 25 major cancers in 2018." In: *European Journal of Cancer* 103, pp. 356–387.
- Ferlay, J., Steliarova-Foucher, E., Lortet-Tieulent, J., Rosso, S., Coebergh, J.-W. W., Comber, H., Forman, D., and Bray, F. (2013). "Cancer incidence and mortality patterns in Europe: estimates for 40 countries in 2012." In: *European Journal of Cancer* 49.6, pp. 1374–1403.
- Fernandez-de-Manuel, L., Wollny, G., Kybic, J., Jimenez-Carretero, D., Tellado, J. M., et al. (2014). "Organ-focused mutual information for nonrigid multimodal registration of liver CT and Gd-EOB-DTPA-enhanced MRI." In: *Medical Image Analysis* 18.1, pp. 22–35.

- Ferrante, E. and Paragios, N. (2017). "Slice-to-volume medical image registration: A survey." In: *Medical Image Analysis* 39, pp. 101–123.
- Fischbach, F., Thormann, M., Seidensticker, M., Kropf, S., Pech, M., and Ricke, J. (2011). "Assessment of fast dynamic imaging and the use of Gd-EOB-DTPA for MR-guided liver interventions." In: *Journal of Magnetic Resonance Imaging* 34.4, pp. 874–879.
- Fischer, B. and Modersitzki, J. (2003). "Curvature based image registration." In: *Journal of Mathematical Imaging and Vision* 18.1, pp. 81–85.
- Foruzan, A. H. and Motlagh, H. R. (2015). "Multimodality liver registration of Open-MR and CT scans." In: *International Journal of Computer Assisted Radiology and Surgery* 10.8, pp. 1253–1267.
- Frydrychowicz, A., Lubner, M. G., Brown, J. J., Merkle, E. M., Nagle, S. K., Rofsky, N. M., and Reeder, S. B. (2012). "Hepatobiliary MR imaging with gadolinium-based contrast agents." In: *Journal of Magnetic Resonance Imaging* 35.3, pp. 492–511.
- Garden, O. J., Rees, M., Poston, G., Mirza, D., Saunders, M., Ledermann, J., Primrose, J., and Parks, R. (2006). "Guidelines for resection of colorectal cancer liver metastases." In: *Gut* 55.suppl 3, pp. iii1–iii8.
- Glocker, B. (2010). "Random Fields for Image Registration."
- Glocker, B., Komodakis, N., Tziritas, G., Navab, N., and Paragios, N. (2008). "Dense image registration through MRFs and efficient linear programming." In: *Medical Image Analysis* 12.6, pp. 731–741.
- Gomez-Iturriaga, A., Casquero, F., Urresola, A., Ezquerro, A., Lopez, J. I., et al. (2016). "Dose escalation to dominant intraprostatic lesions with MRI-transrectal ultrasound fusion High-Dose-Rate prostate brachytherapy. Prospective phase II trial." In: *Radiotherapy and Oncology* 119.1, pp. 91–96.
- Gumus, K., Keating, B., White, N., Andrews-Shigaki, B., Armstrong, B., et al. (2015). "Comparison of optical and MR-based tracking." In: *Magnetic Resonance in Medicine* 74.3, pp. 894–902.
- Haber, E. and Modersitzki, J. (2006). "Intensity gradient based registration and fusion of multi-modal images." In: *International Conference on Medical Image Computing and Computer-Assisted Intervention (MICCAI)*. Springer, pp. 726–733.
- Hallet, J., Sa Cunha, A., Adam, R., Goéré, D., Bachellier, P., et al. (2016). "Factors influencing recurrence following initial hepatectomy for colorectal liver metastases." In: *British Journal of Surgery* 103.10, pp. 1366–1376.
- Holden, M. (2008). "A review of geometric transformations for non-rigid body registration." In: *IEEE Transactions on Medical Imaging* 27.1, p. 111.
- Jamriska, O., Sykora, D., and Hornung, A. (2012). "Cache-efficient graph cuts on structured grids." In: *IEEE Conference on Computer Vision and Pattern Recognition*. IEEE, pp. 3673–3680.

- Kadoury, S., Zagorchev, L., Wood, B. J., Venkatesan, A., Weese, J., Jago, J., and Kruecker, J. (2012). "A model-based registration approach of preoperative MRI with 3D ultrasound of the liver for Interventional guidance procedures." In: *IEEE International Symposium on Biomedical Imaging (ISBI)*. IEEE, pp. 952–955.
- Karabis, A., Giannouli, S., and Baltas, D. (2005). "40 HIPO: A hybrid inverse treatment planning optimization algorithm in HDR brachytherapy." In: *Radiotherapy and Oncology* 76, p. 29.
- Kaus, M. R., Brock, K. K., Pekar, V., Dawson, L. A., Nichol, A. M., and Jaffray, D. A. (2007). "Assessment of a model-based deformable image registration approach for radiation therapy planning." In: *International Journal of Radiation Oncology\* Biology\* Physics* 68.2, pp. 572–580.
- Kim, K. W., Lee, J. M., Klotz, E., Kim, S. J., Kim, S. H., Kim, J. Y., Han, J. K., and Choi, B. I. (2011). "Safety margin assessment after radiofrequency ablation of the liver using registration of preprocedure and postprocedure CT images." In: *American Journal of Roentgenology* 196.5, pp. 565–572.
- König, T., Rak, M., Fensky, S., Held, F., Tönnies, K. D., and Wybranski, C. (2017). "Feasibility of rigid and deformable liver registration for MRI-guided HDR brachytherapy." In: *16. Jahrestagung der Deutschen Gesellschaft für Computer- und Roboterassistierte Chirurgie (CURAC)*, pp. 17–23.
- Lange, T., Eulenstein, S., Hünenbein, M., and Schlag, P.-M. (2003). "Vessel-based non-rigid registration of MR/CT and 3D ultrasound for navigation in liver surgery." In: *Computer Aided Surgery* 8.5, pp. 228–240.
- Lange, T., Wenckebach, T. H., Lamecker, H., Seebass, M., Hünenbein, M., Eulenstein, S., Gebauer, B., and Schlag, P. M. (2005). "Registration of different phases of contrast-enhanced CT/MRI data for computer-assisted liver surgery planning: Evaluation of state-of-the-art methods." In: *The International Journal of Medical Robotics and Computer Assisted Surgery* 1.3, pp. 6–20.
- Lasowski, R., Benhimane, S., Vogel, J., Jakobs, T. F., Zech, C. J., Trumm, C., Clason, C., and Navab, N. (2008). "Adaptive visualization for needle guidance in RF liver ablation: taking organ deformation into account." In: *Medical Imaging 2008: Visualization, Image-Guided Procedures, and Modeling*. Vol. 6918. International Society for Optics and Photonics.
- Lee, B. C., Lee, H. G., Park, I. J., Kim, S. Y., Kim, K.-H., et al. (2016). "The role of radiofrequency ablation for treatment of metachronous isolated hepatic metastasis from colorectal cancer." In: *Medicine* 95.39.
- Lee, W.-C. C., Tublin, M. E., and Chapman, B. E. (2005). "Registration of MR and CT images of the liver: comparison of voxel similarity

- and surface based registration algorithms." In: *Computer Methods and Programs in Biomedicine* 78.2, pp. 101–114.
- Lewis, E. B. and Fox, N. C. (2004). "Correction of differential intensity inhomogeneity in longitudinal MR images." In: *NeuroImage* 23.1, pp. 75–83.
- Litjens, G., Kooi, T., Bejnordi, B. E., Setio, A. A. A., Ciompi, F., et al. (2017). "A survey on deep learning in medical image analysis." In: *Medical Image Analysis* 42, pp. 60–88.
- Liu, P., Eberhardt, B., Wybranski, C., Ricke, J., and Lüdemann, L. (2013). "Nonrigid 3D medical image registration and fusion based on deformable models." In: *Computational and Mathematical Methods in Medicine* 2013, pp. 1–10.
- Luu, H. M., Klink, C., Niessen, W., Moelker, A., and Van Walsum, T. (2016). "Non-rigid registration of liver CT images for CT-guided ablation of liver tumors." In: *PLoS ONE* 11.9.
- Mahapatra, D. and Sun, Y. (2012). "Integrating segmentation information for improved MRF-based elastic image registration." In: *IEEE Transactions on Image Processing* 21.1, pp. 170–183.
- Manfredi, S., Lepage, C., Hatem, C., Coatmeur, O., Faivre, J., and Bouvier, A.-M. (2006). "Epidemiology and management of liver metastases from colorectal cancer." In: *Annals of Surgery* 244.2, p. 254.
- Mattes, D., Haynor, D. R., Vesselle, H., Lewellen, T. K., and Eubank, W. (2001). "Nonrigid multimodality image registration." In: *Medical Imaging 2001: Image Processing*. Vol. 4322. International Society for Optics and Photonics, pp. 1609–1621.
- Mattes, D., Haynor, D. R., Vesselle, H., Lewellen, T. K., and Eubank, W. (2003). "PET-CT image registration in the chest using free-form deformations." In: *IEEE Transactions on Medical Imaging* 22.1, pp. 120–128.
- Mauri, G., Cova, L., De Beni, S., Ierace, T., Tondolo, T., Cerri, A., Goldberg, S. N., and Solbiati, L. (2015). "Real-time US-CT/MRI image fusion for guidance of thermal ablation of liver tumors undetectable with US: results in 295 cases." In: *CardioVascular and Interventional Radiology* 38.1, pp. 143–151.
- Miao, S., Wang, Z. J., and Liao, R. (2016). "A CNN regression approach for real-time 2D/3D registration." In: *IEEE Transactions on Medical Imaging* 35.5, pp. 1352–1363.
- Micu, R., Jakobs, T. F., Urschler, M., and Navab, N. (2006). "A new registration/visualization paradigm for CT-fluoroscopy guided RF liver ablation." In: *International Conference on Medical Image Computing and Computer-Assisted Intervention (MICCAI)*. Springer, pp. 882–890.
- Modersitzki, J. (2004). *Numerical methods for image registration*. Oxford University Press on Demand.

- Modersitzki, J. (2009). *FAIR: Flexible Algorithms for Image Registration*. Philadelphia: SIAM.
- Mohnike, K., Wieners, G., Schwartz, F., Seidensticker, M., Pech, M., et al. (2010). "Computed tomography-guided high-dose-rate brachytherapy in hepatocellular carcinoma: safety, efficacy, and effect on survival." In: *International Journal of Radiation Oncology\* Biology\* Physics* 78.1, pp. 172–179.
- Mohnike, K., Wolf, S., Damm, R., Seidensticker, M., Seidensticker, R., et al. (2016). "Radioablation of liver malignancies with interstitial high-dose-rate brachytherapy." In: *Strahlentherapie und Onkologie* 192.5, pp. 288–296.
- Pace, D. F., Aylward, S. R., and Niethammer, M. (2013). "A locally adaptive regularization based on anisotropic diffusion for deformable image registration of sliding organs." In: *IEEE Transactions on Medical Imaging* 32.11, pp. 2114–2126.
- Papież, B. W., Heinrich, M. P., Fehrenbach, J., Risser, L., and Schnabel, J. A. (2014). "An implicit sliding-motion preserving regularization via bilateral filtering for deformable image registration." In: *Medical Image Analysis* 18.8, pp. 1299–1311.
- Pech, M., Mohnike, K., Wieners, G., Bialek, E., Dudeck, O., et al. (2008). "Radiotherapy of liver metastases. Comparison of target volumes and dose-volume histograms employing CT-or MRI-based treatment planning." In: *Strahlentherapie und Onkologie: Organ der Deutschen Röntgengesellschaft...[et al]* 184.5, pp. 256–261.
- Peterlík, I., Courtecuisse, H., Rohling, R., Abolmaesumi, P., Ngan, C., Cotin, S., and Salcudean, S. (2018). "Fast elastic registration of soft tissues under large deformations." In: *Medical Image Analysis* 45, pp. 24–40.
- Peters, N., Wieners, G., Pech, M., Hengst, S., Rühl, R., et al. (2008). "CT-guided interstitial brachytherapy of primary and secondary lung malignancies." In: *Strahlentherapie und Onkologie* 184.6, pp. 296–301.
- Polgár, C., Major, T., Fodor, J., Németh, G., Orosz, Z., et al. (2004). "High-dose-rate brachytherapy alone versus whole breast radiotherapy with or without tumor bed boost after breast-conserving surgery: seven-year results of a comparative study." In: *International Journal of Radiation Oncology\* Biology\* Physics* 60.4, pp. 1173–1181.
- Prada, P. J., Cardenal, J., Blanco, A. G., Anchuelo, J., Ferri, M., et al. (2016). "High-dose-rate interstitial brachytherapy as monotherapy in one fraction for the treatment of favorable stage prostate cancer: Toxicity and long-term biochemical results." In: *Radiotherapy and Oncology* 119, pp. 411–416.
- Rak, M., König, T., Tönnies, K. D., Walke, M., and Wybranski, C. (2017). "Joint deformable liver registration and bias field correction

- for MR-guided HDR brachytherapy." In: *International Journal of Computer Assisted Radiology and Surgery* 12.12, pp. 2169–2180.
- Ricke, J., Thormann, M., Ludewig, M., Jungnickel, K., Grosser, O., et al. (2010). "MR-guided liver tumor ablation employing open high-field 1.0T MRI for image-guided brachytherapy." In: *European Radiology* 20.8, pp. 1985–1993.
- Ricke, J., Wust, P., Stohlmann, A., Beck, A., Cho, C. H., et al. (2004). "CT-guided interstitial brachytherapy of liver malignancies alone or in combination with thermal ablation: phase I–II results of a novel technique." In: *International Journal of Radiation Oncology\* Biology\* Physics* 58.5, pp. 1496–1505.
- Rohlfing, T., Maurer Jr., C. R., O'Dell, W. G., and Zhong, J. (2004). "Modeling liver motion and deformation during the respiratory cycle using intensity-based nonrigid registration of gated MR images." In: *Medical Physics* 31.3, pp. 427–432.
- Romero, A. M., Verheij, J., Dwarkasing, R. S., Seppenwoolde, Y., Redekop, W. K., et al. (2012). "Comparison of macroscopic pathology measurements with magnetic resonance imaging and assessment of microscopic pathology extension for colorectal liver metastases." In: *International Journal of Radiation Oncology\* Biology\* Physics* 82.1, pp. 159–166.
- Rueckert, D., Sonoda, L. I., Hayes, C., Hill, D. L., Leach, M. O., and Hawkes, D. J. (1999). "Nonrigid registration using free-form deformations: application to breast MR images." In: *IEEE Transactions on Medical Imaging* 18.8, pp. 712–721.
- Rühl, R., Lüdemann, L., Czarnecka, A., Streitparth, F., Seidensticker, M., et al. (2010). "Radiobiological restrictions and tolerance doses of repeated single-fraction HDR-irradiation of intersecting small liver volumes for recurrent hepatic metastases." In: *Radiation Oncology* 5.1, p. 44.
- Salem, R. and Thurston, K. G. (2006). "Radioembolization with <sup>90</sup>Yttrium microspheres: a state-of-the-art brachytherapy treatment for primary and secondary liver malignancies: part 1: technical and methodologic considerations." In: *Journal of Vascular and Interventional Radiology* 17.8, pp. 1251–1278.
- Simonovsky, M., Gutiérrez-Becker, B., Mateus, D., Navab, N., and Komodakis, N. (2016). "A deep metric for multimodal registration." In: *International Conference on Medical Image Computing and Computer-Assisted Intervention (MICCAI)*. Springer, pp. 10–18.
- Sled, J. G., Zijdenbos, A. P., and Evans, A. C. (1998). "A nonparametric method for automatic correction of intensity nonuniformity in MRI data." In: *IEEE Transactions on Medical Imaging* 17, pp. 87–97.
- Sotiras, A., Davatzikos, C., and Paragios, N. (2013). "Deformable medical image registration: A survey." In: *IEEE Transactions on Medical Imaging* 32.7, pp. 1153–1190.



- Studholme, C., Hill, D. L. G., and Hawkes, D. J. (1996). "Incorporating connected region labelling into automated image registration using mutual information." In: *Workshop on Mathematical Methods in Biomedical Image Analysis*. IEEE, pp. 23–31.
- Studholme, C., Hill, D. L. G., and Hawkes, D. J. (1999). "An overlap invariant entropy measure of 3D medical image alignment." In: *Pattern Recognition* 32.1, pp. 71–86.
- Styner, M., Brechbühler, C., Szekely, G., and Gerig, G. (2000). "Parametric estimate of intensity inhomogeneities applied to MRI." In: *IEEE Transactions on Medical Imaging* 19.3, pp. 153–165.
- Suramo, I., Päivänsalo, M., and Myllylä, V. (1984). "Cranio-caudal movements of the liver, pancreas and kidneys in respiration." In: *Acta Radiologica. Diagnosis* 25.2, pp. 129–131.
- Tang, S. and Wang, Y. (2010). "MR-guided liver cancer surgery by nonrigid registration." In: *International Conference on Medical Image Analysis and Clinical Applications (MIACA)*. IEEE, pp. 113–117.
- Tang, T. W. and Chung, A. C. (2007). "Non-rigid image registration using graph-cuts." In: *International Conference on Medical Image Computing and Computer-Assisted Intervention (MICCAI)*. Springer, pp. 916–924.
- Thian, Y. L., Riddell, A. M., and Koh, D.-M. (2013). "Liver-specific agents for contrast-enhanced MRI: role in oncological imaging." In: *Cancer Imaging* 13.4, p. 567.
- Thirion, J.-P. (1996). "Non-rigid matching using demons." In: *IEEE Computer Society Conference on Computer Vision and Pattern Recognition (CVPR)*. IEEE, pp. 245–251.
- Thirion, J.-P. (1998). "Image matching as a diffusion process: an analogy with Maxwell's demons." In: *Medical Image Analysis* 2.3, pp. 243–260.
- Tokuda, J., Plishker, W., Torabi, M., Olubiyi, O. I., Zaki, G., et al. (2015). "Graphics processing unit-accelerated nonrigid registration of MR images to CT images during CT-guided percutaneous liver tumor ablations." In: *Academic Radiology* 22.6, pp. 722–733.
- Tramnitzke, F., Rühak, J., König, L., Modersitzki, J., and Köstler, H. (2014). "GPU based affine linear image registration using normalized gradient fields." In: *International Workshop on High Performance Computing for Biomedical Image Analysis (HPC-MICCAI)*.
- Trouvé, A. (1998). "Diffeomorphisms groups and pattern matching in image analysis." In: *International Journal of Computer Vision* 28.3, pp. 213–221.
- Tustison, N. J., Avants, B. B., Cook, P. A., Zheng, Y., Egan, A., Yushkevich, P. A., and Gee, J. C. (2010). "N4ITK: improved N3 bias correction." In: *IEEE Transactions on Medical Imaging* 29, pp. 1310–1320.
- Van Cutsem, E., Cervantes, A., Adam, R., Sobrero, A., Van Krieken, J., et al. (2016). "ESMO consensus guidelines for the management of

- patients with metastatic colorectal cancer." In: *Annals of Oncology* 27.8, pp. 1386–1422.
- Van den Eynden, G. G., Majeed, A. W., Illemann, M., Vermeulen, P. B., Bird, N. C., et al. (2013). "The multifaceted role of the microenvironment in liver metastasis: biology and clinical implications." In: *Cancer Research* 73.7, pp. 2031–2043.
- Viola, P. and Wells, W. M. (1997). "Alignment by maximization of mutual information." In: *International Journal of Computer Vision* 24.2, pp. 137–154.
- Voroney, J. P., Brock, K. K., Eccles, C., Haider, M., and Dawson, L. A. (2006). "Prospective comparison of computed tomography and magnetic resonance imaging for liver cancer delineation using deformable image registration." In: *International Journal of Radiation Oncology\* Biology\* Physics* 66.3, pp. 780–791.
- Warfield, S. K., Nabavi, A., Butz, T., Tuncali, K., Silverman, S. G., Black, P. M., Jolesz, F. A., and Kikinis, R. (2000). "Intraoperative segmentation and nonrigid registration for image guided therapy." In: *International Conference on Medical Image Computing and Computer-Assisted Intervention (MICCAI)*. Springer, pp. 176–185.
- Wilson, D. L., Carrillo, A., Zheng, L., Genc, A., Duerk, J. L., and Lewin, J. S. (1998). "Evaluation of 3D image registration as applied to MR-guided thermal treatment of liver cancer." In: *Journal of Magnetic Resonance Imaging* 8.1, pp. 77–84.
- Wouters, J., D'Agostino, E., Maes, F., Vandermeulen, D., and Suetens, P. (2006). "Non-rigid brain image registration using a statistical deformation model." In: *Medical Imaging 2006: Image Processing*. Vol. 6144. International Society for Optics and Photonics.
- Wu, G., Kim, M., Wang, Q., Gao, Y., Liao, S., and Shen, D. (2013). "Unsupervised deep feature learning for deformable registration of MR brain images." In: *International Conference on Medical Image Computing and Computer-Assisted Intervention (MICCAI)*. Springer, pp. 649–656.
- Wybranski, C., Eberhardt, B., Fischbach, K., Fischbach, F., Walke, M., et al. (2015). "Accuracy of applicator tip reconstruction in MRI-guided interstitial <sup>192</sup>Ir-high-dose-rate brachytherapy of liver tumors." In: *Radiotherapy and Oncology* 115.1, pp. 72–77.
- Yang, X., Kwitt, R., and Niethammer, M. (2016). "Fast predictive image registration." In: *Deep Learning and Data Labeling for Medical Applications*. Springer, pp. 48–57.
- Yoo, T. S., Ackerman, M. J., Lorensen, W. E., Schroeder, W., Chalana, V., Aylward, S., Metaxas, D., and Whitaker, R. (2002). "Engineering and algorithm design for an image processing API: a technical report on ITK - The Insight Toolkit." In: *Studies in Health Technology and Informatics*, pp. 586–592.

- Zagorchev, L. and Goshtasby, A. (2006). "A comparative study of transformation functions for nonrigid image registration." In: *IEEE Transactions on Image Processing* 15.3, pp. 529–538.